

Prediction of Excitation Angles for a Switched Reluctance Generator using Artificial Neural Network

Pairote Thongprasri

Faculty of Engineering at Sriracha, Kasetsart University Sriracha Campus,
 199, Sukumvit Road, Tungskula, Chonburi 20230, Thailand

Abstract: This paper presents a method to determine excitation angles for a Switched Reluctance Generator (SRG) by using Artificial Neural Network (ANN). The ANN model consists of the feed-forward neural network and the back-propagation learning with a linear activation function (the linear function) and a nonlinear function (the hyperbolic tangent). The ANN model with two layers; the hidden layer and the output layer, is derived from the current and flux linkage of the SRG. The SRG model is built from the magnetization curve which the flux linkage versus current at different rotor positions is analyzed from the finite element method (FEM). An 8/6 SRG was set up to validate the proposed ANN method.

Keywords: artificial neural network; feed-forward; back-propagation; hidden layer; output layer

1. INTRODUCTION

Advantages of SRGs are fault tolerance, high robustness, and high efficiency. The SRG has remarkable characteristics which employs as a variable speed generator [1]. However, the SRG requires a position sensor for the commutation of the stator phases in synchronism with the rotor position and its nonlinear electrical behavior provides a high torque ripple [2]. Finite Element Method (FEM) is the accurate solution to the model problem in SRG. However, FEM is a time consuming process and has a lot of data. An optimized design of the SRG for maximum output power is proposed [3]. The system based on a simple controller is proposed that the optimal control angles are determined online [4]. A back-propagation neural network is a multilayer feed forward network trained by back propagation algorithm. The objective is to train the network to achieve a balance between the ability to respond correctly to the input patterns. The training of a network by back-propagation involves three stages; the feed-forward of the input training pattern, the calculation and back-propagation of the associated error, and the adjustment of the weights. After training, application of the net involves only the computations of the feed-forward phase. A multilayer net (with one or more hidden layers) can learn any continuous mapping to an arbitrary accuracy.

The proposed method in this paper utilizes FEM and Artificial Neural Network (ANN). A model of a SRG based on MATLAB/Simulink depending on the flux linkage and the inductance obtained from FEM. A training data set is generated by control parameters of the SRG. Neural mapping used to predict the excitation angles after good training.

2. OPERATION OF SWITCHED RELUCTANCE GENERATOR

The SRG structure is double protruding pole. The SRG has steel laminations on the rotor and stator as shown in Fig.1 that there are no windings or permanent magnets on the rotor. The operation of SRG depends entirely on synchronized excitation of the set of stator windings to create continuous rotation of the rotor poles. When the switches S1 and S2 are turned on, the windings on the stator are excited by the outer circuit, and the electrical energy and mechanical energy provided by

exterior circuit are converted into magnetic field energy. When the switches S1 and S2 are turned off, nevertheless the diodes D1 and D2 are turned on. The magnetic field energy and mechanical energy are converted into electricity energy to the load.

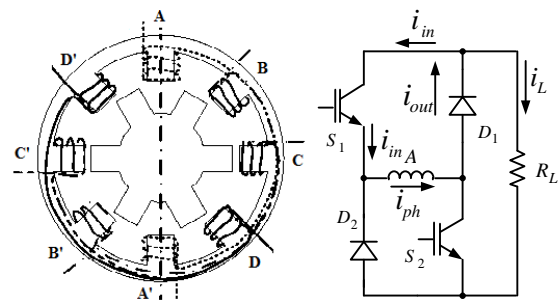


Figure. 1. 8/6 SRG structure (left) and its converter (right)

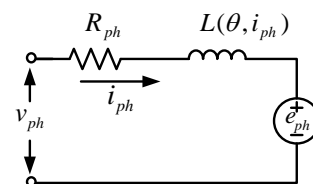


Figure. 2. Equivalent circuit of one phase SRG

The equivalent circuit of one phase SRG is shown in Fig. 2 that the phase voltage can be expressed by

$$v_{ph} = R_{ph} i_{ph} + \frac{L(\theta, i_{ph}) di_{ph}}{dt} + \frac{dL(\theta, i_{ph})}{d\theta} \cdot i_{ph} \cdot \omega \quad (1)$$

where:

- R_{ph} is the phase resistance
- i_{ph} is the phase current
- L is the inductance
- ω is the rotor speed.

In this paper, the value of parameter of the candidate 8/6 SRG is shown in Table 1. The characteristics of flux linkage versus the current and rotor position of the SRG can be determined using the Finite Element Method (FEM) as shown in Fig. 3. The relationship between the flux linkage at the aligned and unaligned positions can be obtained from the FEM and is shown in Fig. 4. The relationship between the flux linkage and the phase current at different rotor positions is shown in Fig. 5.

Table 1. The value of parameter of the candidate SRG

Parameter	Value
Outer diameter of stator	150 mm
Inner diameter of stator	70 mm
Stack length	70 mm
Shaft diameter	24 mm
Length of air gap	0.5 mm
Stator pole arc	22°
Rotor pole arc	24°

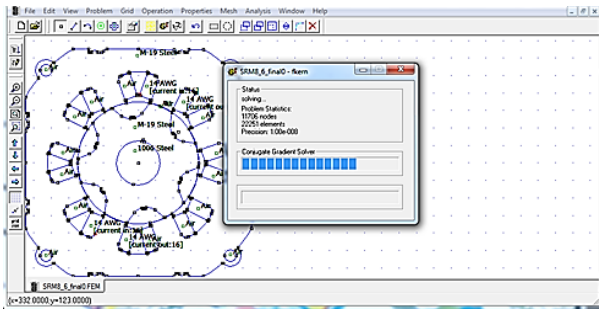


Figure 3. Finite element method

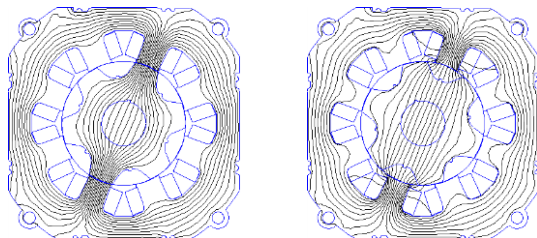


Figure 4. Aligned (left) and unaligned (right) rotor positions

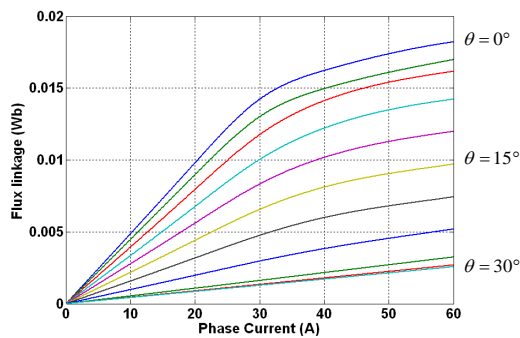


Figure 5. Characteristics of flux linkage versus current and rotor position

The mathematical model of the phase current of the SRG is shown in Fig. 6 which is obtained using Eq. (1).

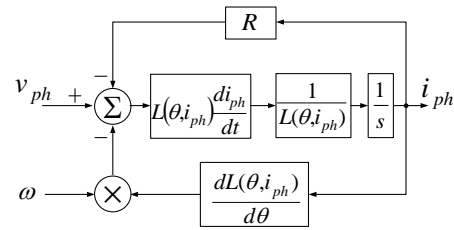
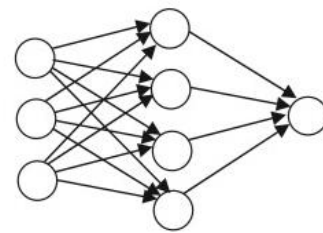


Figure 6. Block diagram for mathematical model of the phase current

3. ARTIFICIAL NEURAL NETWORKS

Artificial neural network (ANN) is computing systems whose structures are inspired by a simplified model of the human brain [5]. In Fig.7 describes a typical 3-layer feed-forward ANN. It consists of input layer, output layer and hidden layer. Activation signal of nodes in one layer are transmitted to the next layer through weights which either attenuate the signal [6]. The value of the weights in a supervised ANN is determined through the iterative training process. ANN output is compared with true output from training data set, and then the weights are adjusted incrementally to make the error minimum. Several learning methods have been developed such as back-propagation, Levenberg-Marquardt [7].



Input Hidden layer Output layer

Figure 7. Typical 3-layer feed-forward ANN

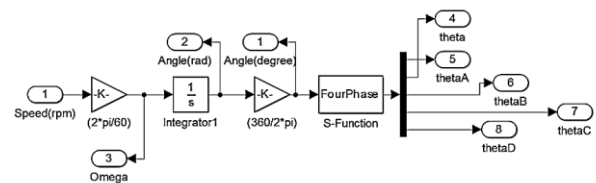


Figure 8. Block diagram for mathematical model of the rotor position

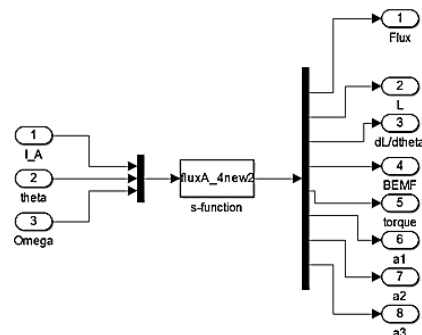


Figure 9. Block diagram for mathematical model of the flux linkage

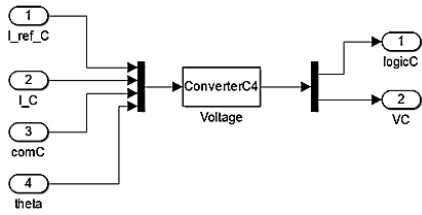


Figure 10. Block diagram for mathematical model of the converter

The SRG model using FEM data consists of the rotor position model, the flux linkage model, and the converter model as shown in Figs 8-10, respectively. These models are used to simulate to collect data of the control parameters in different conditions. These data are used to train the ANN model. The mathematical model of inductance is shown in Fig. 11. The inductance based on the mathematical model and the block diagram to calculate of the SRG model are shown in Fig. 12 and Fig. 13, respectively.

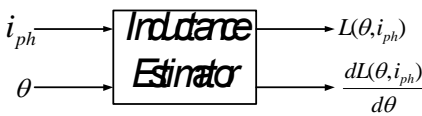


Figure 11. Block diagram for inductance estimator

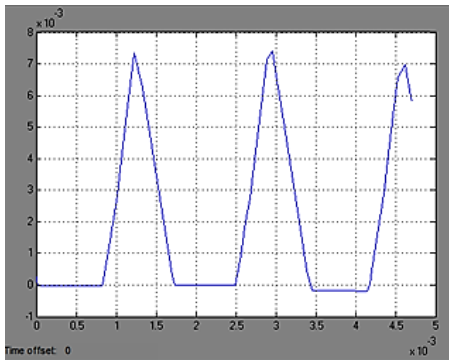


Figure 12. Inductance based on the proposed model

Torque of the SRG can be given as

$$T_e = \frac{1}{2} \cdot i_{ph}^2 \frac{dL(\theta, i_{ph})}{d\theta} \quad (2)$$

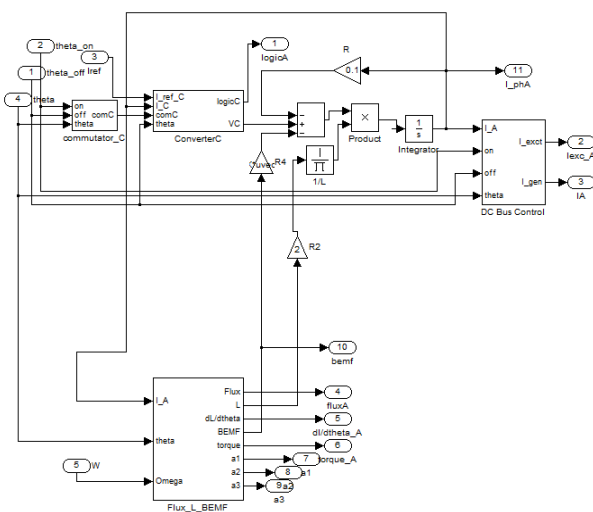


Figure 13. Block diagram for calculation of the SRG

4. SIMULATION AND EXPERIMENTAL RESULTS

The 8/6 SRG system is shown in Fig. 14. The induction motor is used as the prime mover. A variable transformer with a rectifier is used as the constant DC bus voltage. The average torque of the generator is measured by a rotational torque transducer. The rotor speed and the aligned rotor position are detected by a resolver mounted on the SRG. One ohm resistor is used as the load. The schematic layout of the experimental setup is shown in Fig. 15.

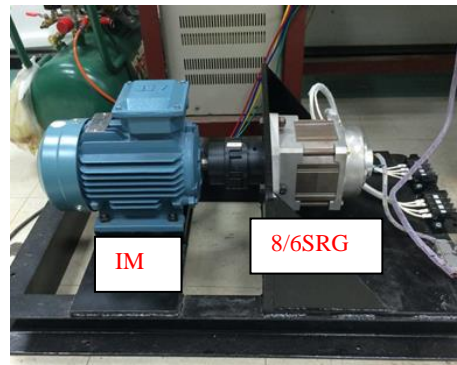
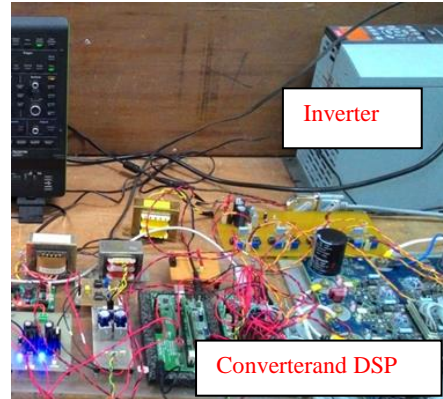


Figure 14. 8/6 experimental Setup

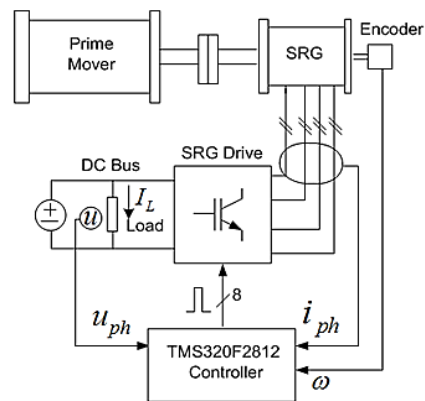


Figure 15. Schematic layout of the experimental system

Fig 16 shows the rotor position of 4 phases of the SRG. Fig 17 shows the simulation results obtained from the mathematical model when the SRG is controlled at positions of turn-on = 0° and turn-off = 13°.

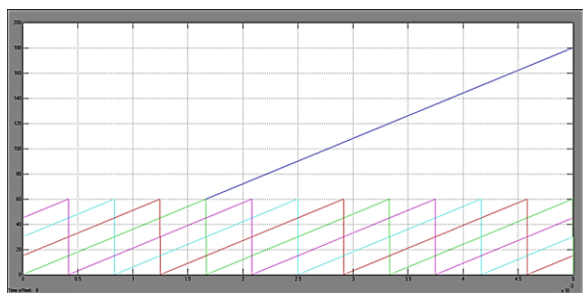


Figure. 16. Rotor position of 4-phase SRG

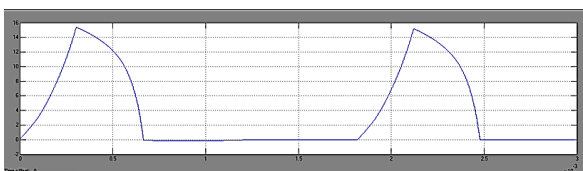


Figure. 17. Phase current shape at of turn-on = 0° and turn-off = 13°

Data of the flux linkage, the rotor speed, the excitation angles, the DC bus voltage, and the phase current are used to train the ANN model. Ultimately; the ANN model only requires the data of the flux linkage and the phase current.

To validate the ANN model, the experiment results in 5 cases are shown in Table 2 when the proposed model of the SRG compare with the ANN model. And Figs. 18-22 show the results based on the proposed ANN model, the mathematical model, and the experiments. The waveforms of the phase voltage, phase current, the total torque (inverse), and the rotor position are described in the proposed model and the experiments.

Table 2. The value of parameter of the candidate SRG

Case	Turn-on (°)		Turn-off (°)	
	Model	ANN	Model	ANN
1	0	0.1472	15	15.45
2	2	2.078	11	11.7
3	3	3.209	15	15.33
4	5	4.757	14	14.26
5	8	7.758	16	15.64

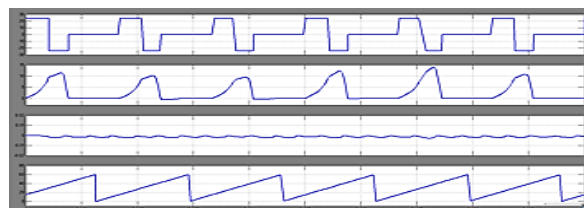
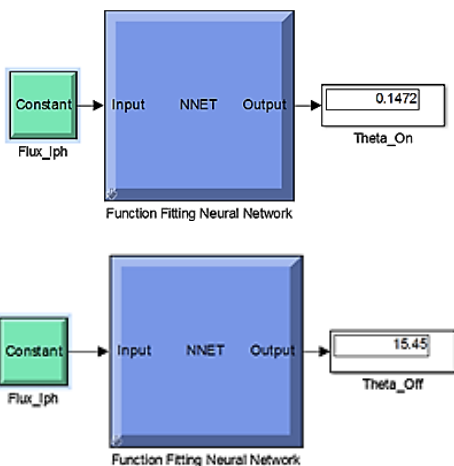


Figure. 18. Case 1 with turn-on at 0° and turn-off at 15°; the proposed ANN (top), the mathematical model (middle), and the experiment

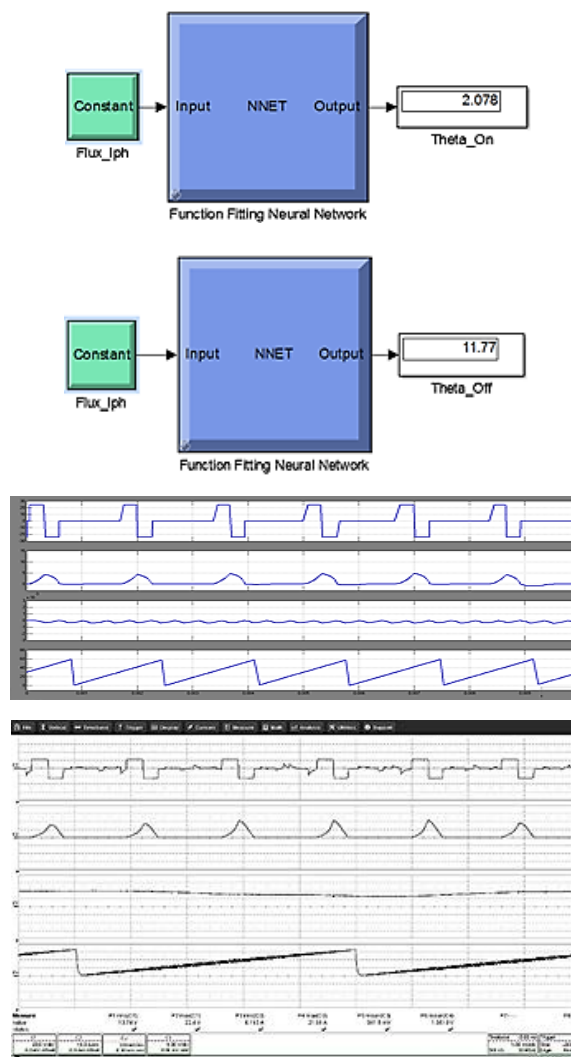


Figure. 19. Case 2 with turn-on at 2° and turn-off at 11°; the proposed ANN (top), the mathematical model (middle), and the experiment

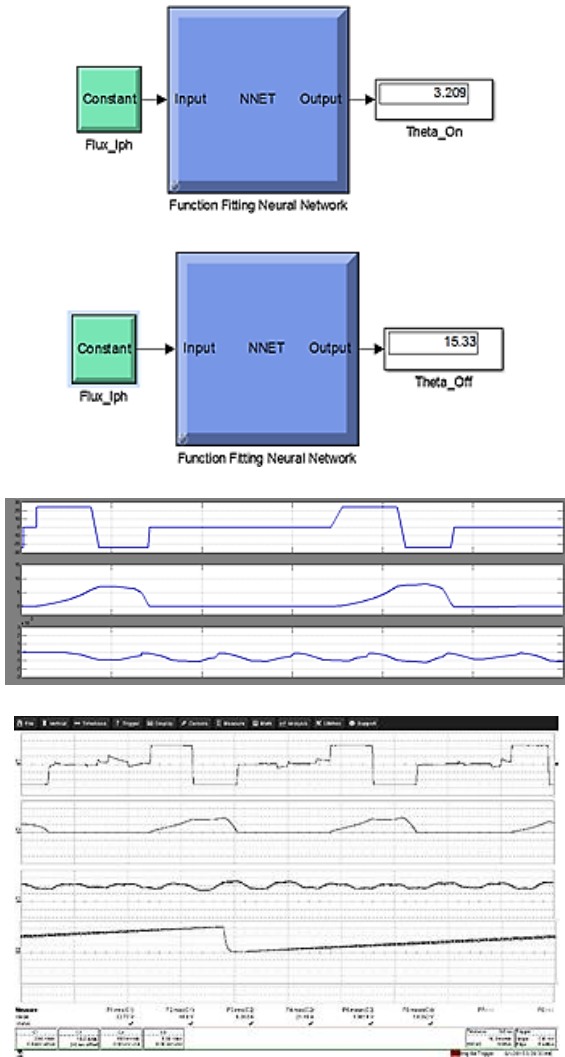


Figure 20. Case 3 with turn-on at 3° and turn-off at 15°; the proposed ANN (top), the mathematical model (middle), and the experiment

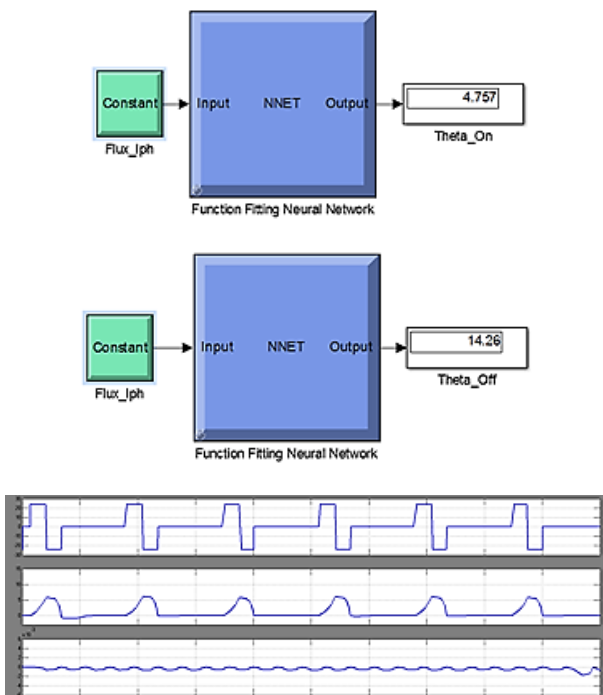


Figure 21. Case 4 with turn-on at 5° and turn-off at 14°; the proposed ANN (top), the mathematical model (middle), and the experiment

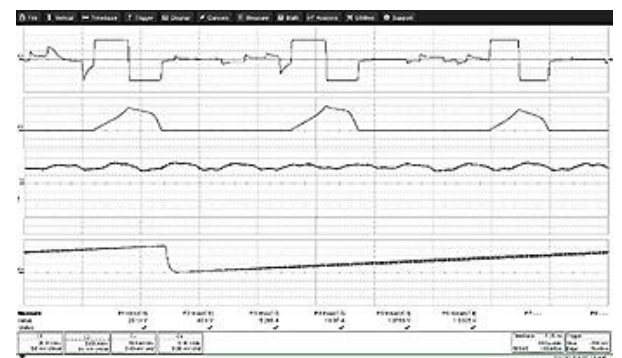
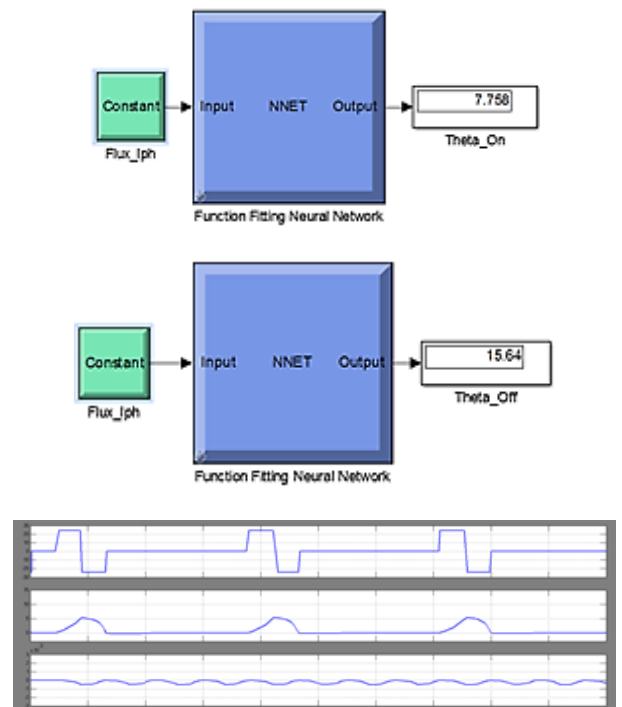


Figure 22. Case 5 with turn-on at 8° and turn-off at 16°; the proposed ANN (top), the mathematical model (middle), and the experiment

5. CONCLUSIONS

The ANN method for predicting the excitation angles of a SRG is proposed. The FEM is used to analyze the magnetization curve. The data obtained from the FEM is provided to build the SRG model. The model gives the

position of excitation angles. The data of the flux linkage and phase current and control parameters are used to train the proposed ANN model. Regarding to results, the ANN can accurately predict to determine the excitation angles of the SRG. The average error is 4.9% compared to the mathematical model.

6. REFERENCES

- [1] K.M. Rahman, S. Gopalakrishnan, Optimized, Instantaneous Torque Control of Switched Reluctance Motor by Neural Network, in Proc. IEEE IAS, vol. 37, 2001, pp. 904-913.
- [2] E. Mese, D.A. Torrey, An approach for Sensorless Position Estimation for Switched Reluctance Motors Using Artificial Neural Networks, IEEE Trans. Power Electronics, vol.17. no. 1, 2002, pp. 66-75.
- [3] P. Asadi, M. Ehsani, and B. Fahimi, Design and control characterization of switched reluctance generator for maximum output power, in Proc. IEEE APEC, 2006, pp. 1639-1644.
- [4] R.G. Lopez and B. Diong, "Simplified control of switched reluctance machines for AC generation," in Proc. IEEE IAS, vol. 1, 2004, pp. 409.
- [5] K. Yilmaz, E. Mese, A. Cengiz, Minimum Inductance Estimation In Switched Reluctance Motors By Using Artificial Neural Networks, in Proc. IEEE MELECON, 2002, pp. 152-156.
- [6] H. Haykin, Neural Networks; A comprehensive Foundation, IEEE press, Macmillan College Publish Comp., 1994
- [7] J.M. Zurada, Introduction to Artificial Neural Systems, PWS Publishing Company, 1992.

Geochemical Studies for Gold in Alut Anomaly District

Mohammadreza Agharezaei

Department of Mining and Metallurgy Engineering,
Amirkabir University of Technology (Tehran
Polytechnic)
Tehran, Iran

Ardeshir Hezarkhani

Department of Mining and Metallurgy Engineering,
Amirkabir University of Technology (Tehran
Polytechnic)
Tehran, Iran

Abstract: The target in this research is detecting Gold anomalies in Alut district. This area is located in western Iran. The area mostly consists of metamorphic rocks extended along geological structures. Geochemical anomaly detection for gold begins with sampling in the study area. The samples are obtained from drainages of the area thus the samples are surface soil specimens. These samples are analyzed by ICP-MS. Then statistical and non-statistical methods are applied to define anomalies in the area. Finally anomaly maps are generated.

Keywords: Geochemistry, Gold, Boxplot, C-A fractal, Alut.

1. INTRODUCTION

Gold prospection and exploration date back to centuries ago since the human was familiar with this valuable metal. This process has been systematized in the recent decades. Nowadays mining prospection and exploration includes different fields of study. One of the most important fields is geochemistry. Geochemical behavior of elements in a study area is a critical answer key to exploration uncertainties. Geochemistry as an important field in mining exploration is developed by several experts. Most of the endeavor in this field is trying to locate mineral deposits, which is technically defined as anomaly delineation and separation from background. Delineation of geochemical anomalies from background is one of the major targets in exploration geochemistry. In order to achieve this goal, different descriptive and quantities methods have been employed [1].

Statistical approaches are one of the most popular and useful methods in geochemical exploration. Among different statistical approaches, the Exploratory Data Analysis (EDA) methods are highly helpful in understanding single-element distribution and defining outlier data. The EDA methods are firstly expressed by Tukey [2] and then developed by other experts for geochemical studies [3-8]. The boxplot is one of the EDA methods. The Boxplot function is most informative if the true number of outliers is below 10% [10]. The other statistical approach for anomaly detection is X+tS introduced by Solovov [9].

The other geochemical approach for anomaly separation from back ground is fractal modeling firstly introduced by Mandelbort [10] and then developed by other researchers. One of the most off use fractal modeling types is Concentration-Area (C-A) fractal modeling developed by Cheng et al. [11] and Li et al. [12].

In this study, anomaly delineation and geochemical behavior of gold has been studied in Alut district, Iran. The geochemical surface sampling covers the whole study area. The data obtained from these samples are then processed by different geochemical methods as introduced above. Finally the results of these methods are compared and discussed.

2. GEOLOGY SETTINGS

The geology of Iran is in accordance to continental fragments initially rifted from Gondwana land. The geological studies of Iran has begun since decades ago containing [13-25]. Iran has one of the most complex economic geology settings in the world including several metallic and non-metallic deposits. Among different mineral resources in Iran, gold mineralization is considerable and valuable to be studied and explored.

Alut area in Kurdistan, Iran is noticeable as a promising gold mineralization district. The area is located between 45°30'00" E to 46°00'00" E longitudes and 35°30'00" N to 36°00'00" N latitudes. The geology of the area is mostly in consistence to metamorphism. Figure 1 depicts the geological map of the study area.

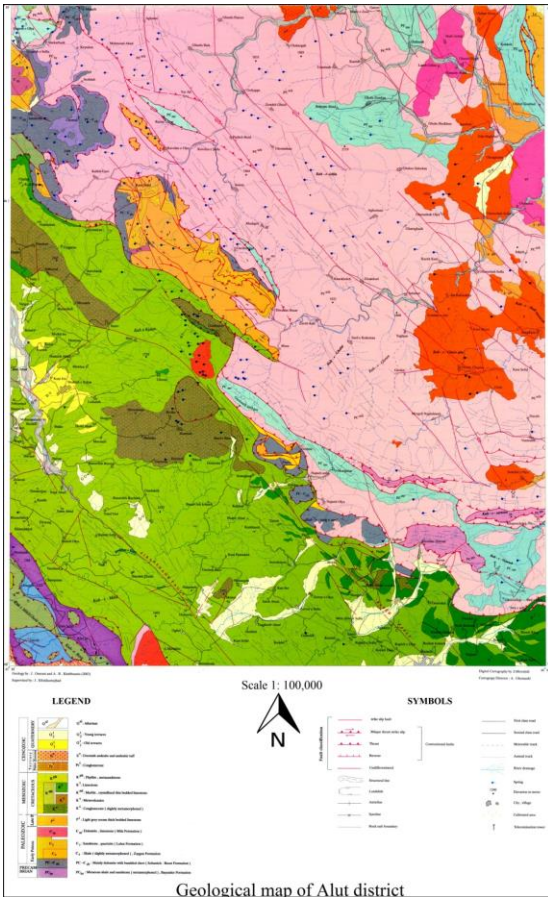


Figure 1. Geological map of the study area (modified after the geological survey of Iran)

The area is generally consisted of metamorphic rocks such as Gneiss, Mica schist and amphibolites. The similarities of rocks with low degree of metamorphism to Kahar formation rocks, inspires that the metamorphic rocks are derived from Kahar formation and then under tectonic activities, metamorphism degree has increased in some parts. In the north-west of the area, carbonate unites including Shale and Mica-bearing sandstone and in the north-east of the area small outcrop of acidic volcanic rock unites mainly consisted of Rhyolite and meta-Rhyolite observed. The oldest rock unites in the area is Permian carbonates. There is no rock unite in accordance to Triassic and Jurassic age. The youngest rock unite is related to cretaceous age which have suffered low degree of metamorphism. The most noticeable magmatic activities in the area are the granite intrusive series in the north-east of the area with Jurassic age [26].

3. METHODOLOGY

3.1 The Exploratory Data Analysis (EDA) method (The Boxplot)

The Boxplot as one of the most popular and beneficial type of the EDA methods divides the data-set into four quartiles (Fig.2). The box consists of 2nd and 3rd quartiles which approximately contain fifty percents of the samples. The other segments are: lower and upper fences with the distance of 1.5 times of the box length from each side of the box, lower and upper hinges which are the 2nd and 4th quartiles (or the equal median of the first and second half of the dataset around the main median) and lower and upper whiskers extended to the two most extreme data values which are still inside the fences. The threshold value is the upper fence which denotes that samples with higher values than the upper fence can be defined as anomalies in dataset [1].

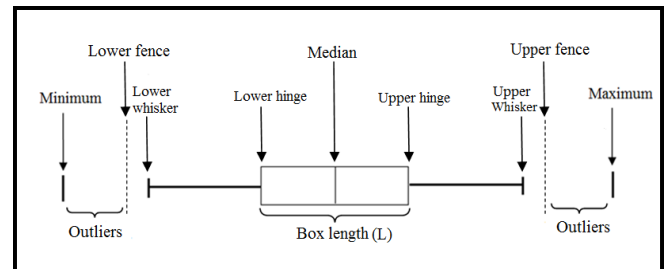


Figure 2. Schematic definition of the boxplot [1].

3.2 The statistical method X+tS method

This statistical method is based on the different levels of confidence which is represented by "t" in the general form of this method "X+tS". X is the average of the variable and S is the standard deviation. Different confidence levels will cause different anomaly thresholds.

3.3 Concentration-Area (C-A) fractal modeling

In spite of statistical methods, fractal modeling methods are structural approaches meaning that the location of the samples has direct effect on the results. The C-A fractal modeling was firstly expressed by Cheng et al [11] as following:

Let $A(p)$ denote the area with concentration values greater than the contour value p . This implies that $A(p)$ is a decreasing function of p . If v represents the threshold, the following empirical model generally provides a good fit to the data for different elements in the study area:

$$A(p \leq v) \propto p^{-\alpha_1}; \quad A(p > v) \propto p^{-\alpha_2}$$

Where α denotes proportionality.

4. DISCUSSION

In this research 836 soil samples were obtained from the area (Fig.3) and then analyzed by ICP-MS method. The data process began with data normalization. Then normalized data are used for the statistical and non-statistical studies for gold.

Lower hinge	1.40
Median	1.80
Upper hinge	2.66
Upper whisker	3.70
Threshold	4.56
Max	8.30

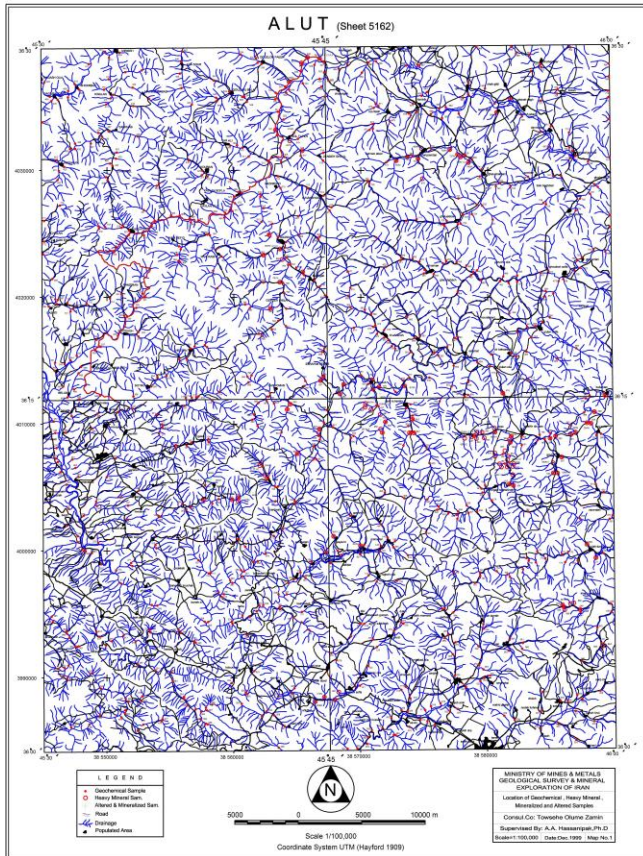


Figure 3. Sampling map.

4.1 The Boxplot

According to the boxplot, the data-set is classified as table 1.

Table 1. Summary statistics of the boxplot for gold.

	Au(ppb)
N	836
Min	0.43
Lower whisker	0.49

The threshold for Gold based on this method is 4.56 ppb. This threshold is applied to the map (Fig.4) in which samples are plotted according to their X-Y coordination and Z value (grade of gold). The software used for map generation is Surfer 11.0.642.

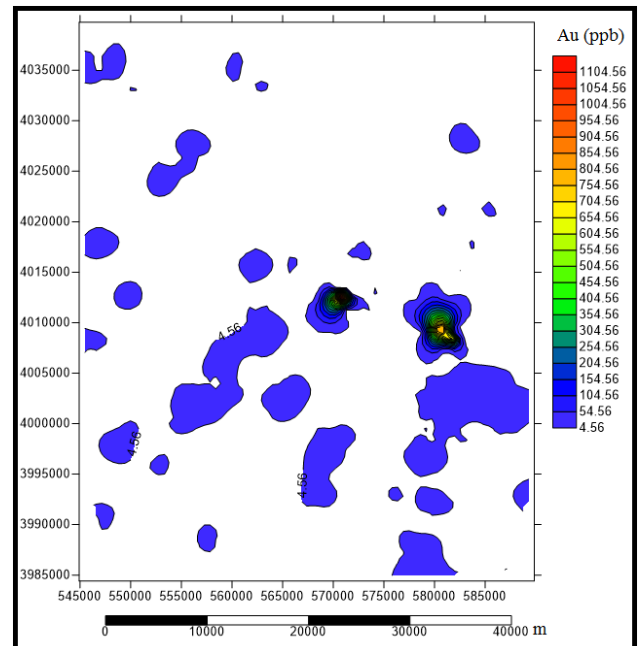


Figure 4. Geochemical anomalies for gold detected by the boxplot method

4.2 The X+tS method

Based on this method, different confidence levels could be applied for anomaly detection. In this study, commonly used confidence level ($t=2$) is applied. Based on different values of “t”, different anomaly maps are generated (Fig.5). The software used for map generation is Surfer 11.0.642.

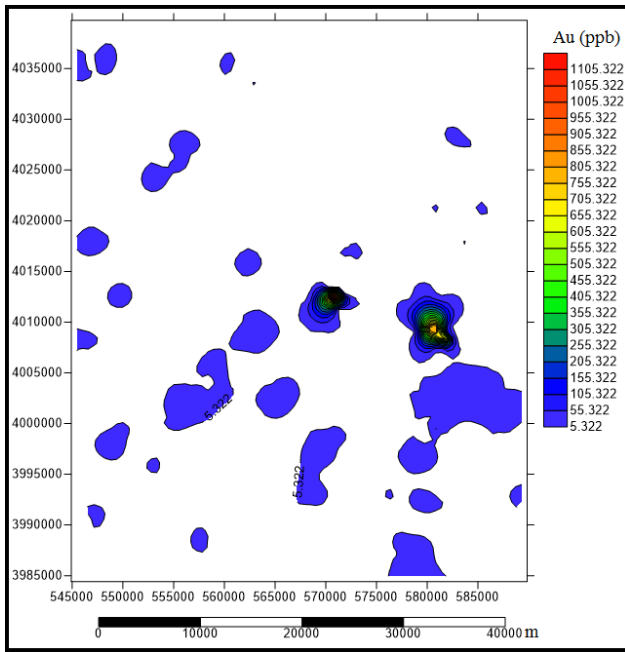


Figure 5. Geochemical anomalies for gold detected by X+2S method.

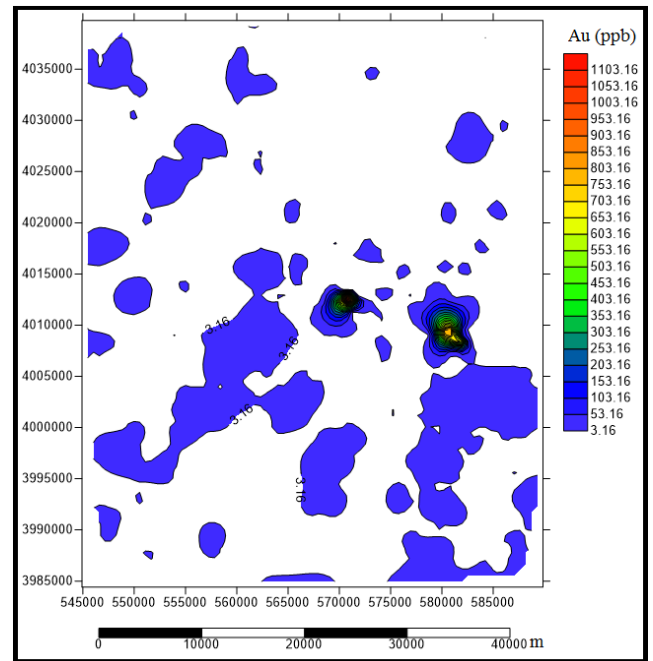


Figure 7. Geochemical anomalies for gold detected by C-A fractal method

4.3 The C-A fractal modeling

According to this method, the area enclosed by contours with different values must be calculated firstly. Based on the calculated area for each contour, the C-A log-log plot is drawn (Fig.6).

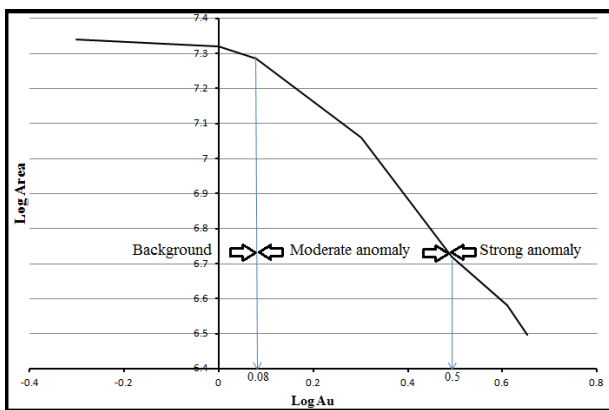


Figure 6. C-A log-log plot.

According to the C-A fractal modeling, the threshold for gold is defined as 3.16 ppb. The anomaly map for C-A fractal modeling is shown in figure 7. The software used for map generation is Surfer 11.0.642.

5. CONCLUSION

In this study, the aim was detection of gold geochemical anomalies. To begin the studies, 836 samples were obtained from the area (surface soil) and then analyzed. The geochemical data-set was created after data normalization. In order to detect Gold anomalies, different statistical and non-statistical methods were applied and the result was anomaly maps. Based on these anomaly maps, most of gold potential is located in the middle of the area where all the applied methods detected anomaly there.

6. REFERENCES

- [1] Agharezaei, M. and Hezarkhani, A. (2016) Delineation of Geochemical Anomalies Based on Cu by the Boxplot as an Exploratory Data Analysis (EDA) Method and Concentration-Volume (C-V) Fractal Modeling in Mesgaran Mining Area, Eastern Iran. *Open Journal of Geology*, 6, 1269-1278.
- [2] Tukey, J.W. (1977) *Exploratory Data Analysis*. Addison-Wesley, Reading.
- [3] Campbell, N.A. (1982) *Statistical Treatment of Geochemical Data*. In: Smith, R.E., Ed., *Geochemical Exploration in Deeply Weathered Terrain*, CSIRO Institute of Energy and Earth Resources, Floreat Park, Western Australia, 141-144.
- [4] Garrett, R.G. (1988) IDEAS: An Interactive Computer Graphics Tool to Assist the Exploration Geochemist. *Geological Survey of Canada*, Paper 88-1F, 1-13.

- [5] Chork, C.Y. and Mazzucchelli, R.H. (1989) Spatial Filtering of Exploration Geochemical Data Using EDA and Robust Statistics. *Journal of Geochemical Exploration*, 34, 221-243. [http://dx.doi.org/10.1016/0375-6742\(89\)90114-3](http://dx.doi.org/10.1016/0375-6742(89)90114-3)
- [6] Reimann, C. and Garrett, R.G. (2005) Geochemical Background-Concept and Reality. *Science of the Total Environment*, 350, 12-27. <http://dx.doi.org/10.1016/j.scitotenv.2005.01.047>
- [7] Carranza, E.J.M. (2009) Geochemical Anomaly and Mineral Prospectivity Mapping in GIS. *Handbook of Exploration and Environmental Geochemistry*, 11. Elsevier, 351 p.
- [8] Carranza, E.J.M. (2010) Catchment Basin Modelling of Stream Sediment Anomalies Revisited: Incorporation of EDA and Fractal Analysis. *Geochemistry : Exploration, Environment , Analysis*, 10, 365-381. <http://dx.doi.org/10.1144/1467-7873/09-224>
- [9] Solovov., A.P. 1985. Geochemical prospecting for mineral deposits, Mir publication Moscow, 288p.
- [10] Mandelbort, B.B. (1982) *The Fractal Geometry of Nature*. Freeman, San Francisco, 460 p.
- [11] Cheng, Q., Agterberg, F.P. and Ballantyne, S.B. (1994) The Separation of Geochemical Anomalies from Background by Fractal Methods. *Journal of Geochemical Exploration*, 51, 109-130. [http://dx.doi.org/10.1016/0375-6742\(94\)90013-2](http://dx.doi.org/10.1016/0375-6742(94)90013-2)
- [12] Li, C., Ma, T. and Shi, J. (2003) Application of a Fractal method Relating Concentrations and Distances for Separation of Geochemical Anomalies from Background. *Journal of Geochemical Exploration*, 77, 167-175. [http://dx.doi.org/10.1016/S0375-6742\(02\)00276-5](http://dx.doi.org/10.1016/S0375-6742(02)00276-5)
- [13] Stocklin, J., 1974. A-Northern Iran: Alborz mountains. Mesozoic – Cenozoic orogenic Belt, data for orogenic studies. In: Spennner, A.M. (Ed.), *Geol. Soc.*, London, Sp. Pub4. Scottish Academic Press, pp. 213–234.
- [14] Sengör, A.M.C., 1984. The Cimmeride orogenic system and the tectonics of Eurasia. *Geol. Soc. Am. Spec. Pap.* 195, 1–82.
- [15] Sengör, A.M.C., Altiner, D., Cin, A., Ustaomer, T., Hsu, K.J., 1988. Origin and assembly of the Tethyside orogenic collage at the expense of Gondwanaland. In: Audley- Charles, M.G., Hallam, A. (Eds.), *Gondwana and Tethys*. *Geol. Soc. Lond. Spec. Publ.* 37, pp. 81–119.
- [16] Davouzadeh, M., Schmidt, K., 1984. A review of the Mesozoic paleogeography and paleotectonic evolution of Iran. *N. Jahrb. Geol. Palaontol. Abh.* 68, 182–207.
- [17] Kazmin, V.G., 1991. Collision and rifting in the Tethys Ocean: geodynamic implications. *Tectonophysics* 196, 371–384.
- [18] Boulin, J., 1991. Structures in Southwest Asia and evolution of the eastern Tethys. *Tectonophysics* 196, 211–268.
- [19] Alavi, M., 1994. Tectonic of the Zagros orogenic belt of Iran: new data and interpretations. *Tectonophysics* 229, 211–239.
- [20] Ramezani, J., Tucker, R.D., 2003. The Saghand region, central Iran: U–Pb geochronology, petrogenesis and implications for Gondwana tectonics. *Am. J. Sci.* 303, 622–665.
- [21] Stampfli, G.M., Borel, G.D., 2004. The TRANSMED transects inspace and time: constraints on the paleotectonic evolution of the Mediterranean domain. In: Cavazza, W., et al. (Ed.), *The TRANSMED Atlas: The Mediterranean Region from Crust to Mantle*. Springer, New York, pp. 53–80.
- [22] Bagheri, S., Stampfli, G.M., 2008. A new litho-structural subdivision for the Palaeotethys terranes in central Iran (Anarak, Jandaq and Posht-e-Badamareas) and its geodynamic implications.
- [23] Hassanzadeh, J., Stockli, D.F., Horton, B.K., Axen, G.J., Stockli, L.D., Grove, M., Schmitt, A.K., Walker, J.D., 2008. U–Pb zircon geochronology of late Neoproterozoic–Early Cambrian granitoids in Iran: implications for paleogeography, magmatism, and exhumation history of Iranian basement. *Tectonophysics* 451, 71–96.
- [24] Omrani, J., Agard, P., Whitechurch, H., Benoit, M., Prouteau, G., Jolivet, L., 2008. Arcmagmatism and subduction history beneath the Zagros Mountains, Iran: a new report of adakites and geodynamic consequences. *Lithos* 106, 380–398.
- [25] Agard, P., Yamato, P., Jolivet, L., Burov, E., 2009. Exhumation of oceanic blueschists and eclogites in subduction zones: timing and mechanisms. *Earth Sci. Rev.* 92, 53–79.
- [26] Tajodin, H.A. (2006) 'control and introduction of mining promising districts in Baneh 1:100000 sheet', geological survey and mineral exploration of Iran.

A Neuro-Fuzzy Based Approach to Object Tracking and Motion Prediction

Engr. Simon Samuel
Department of Electrical and
Electronics Engineering
Modibbo Adama University of
Technology Yola, Adamawa
State, Nigeria

Engr. Ibrahim A. Usman
Department of Electrical and
Electronics Engineering
Modibbo Adama University of
Technology Yola, Adamawa
State, Nigeria

Engr. Baams Baamani Alfred
Department of Electrical and
Electronics Engineering
Modibbo Adama University of
Technology Yola, Adamawa
State, Nigeria

Abstract: In this Paper, object tracking system model was developed using Neuro-Fuzzy hybrid based approach to predict the trajectory of an object moving around a scene. Servo motors were used to perform high-precision positioning in azimuth and elevation directions, fuzzy logic is applied to control the position servo motors via feedback. A Neuro-Fuzzy hybrid approach is used to design the fuzzy rule base of the intelligent system for control. In particular, ANFIS methodology was used to build a Sugeno fuzzy model for controlling the servo motor position carrying charge couple device camera (CCD) on a chaotic trajectory. An advanced test bed is used in order to evaluate the tracking properties and the robustness of the ANFIS controller operations. However, the variations of the Mechanical configuration of the drive, which is common to these two applications, can lead to error in object positioning before segmentation. The result for the azimuth and elevation time responses show that the rise time t_r reduces to 0.1 and 0.3, respectively. The settling time decreases to 0.5 for the motors with ANFIS controller, the delay time reduces to 0.1 for both motors. Steady state was reached. Conclusively, ANFIS controller output was the best in terms of faster rise time, settling time, reduced delay time and object position stabilization.

Keywords: ANFIS, Charge couple device (CCD)-Positioning System, DC servomotor, Segmentation.

1. Introduction.

Object tracking and motion prediction are ways of estimating moving object path and position as it moves/stops in an environment. It plays a key role in an intelligent visioning for environmental monitoring during surveillance especially in military, traffic monitoring and sport video analysis. In tracking, a system approaches a moving object (also called target) matching its location and velocity. Tracking system in literature consist of three parts; a controller that receives information on the position of object through a sensor, a dummy moving mechanism which follows an object based on controller directive, and a system vision which captures the object picture as it moves around a scene e.g a camera[1]. A major problem to object tracking is the uncertainty associated with the environments within which the system have to operate due to illumination, changing appearance patterns of the object and the scene, abrupt object motion, non-rigid object structures, object-to-object and object-to-scene occlusions, and camera motion stabilization. To address the fore mentioned challenges the controller must denote the ability to learn about the operating environment, the moving mechanism directed by the controller must be prompt or without delay to follow the object, finally, the system vision which in most case the camera must be clear to present the target object when segmented through coloured image processing [2].

The study is aimed at tracking object operating on a sequence of video images provided by camera through the application of Neuro-fuzzy logic system.

The objectives of this work are; to use Neuro-fuzzy techniques to develop a rule based fuzzy system as an efficient and robust approach for object tracking on a sequence of video image and predict position of object on a trajectory.

2. Related Works

Object tracking was defined as approaching a moving object (also called target) matching its location and velocity. The tasks have a wide range of applications. We shall review some of the methods outlining clearly the limitations that necessitate the hybrid method used. The early tracking methodologies uses background subtractions; in these methods, the authors utilize and optimized threshold systems to obtain the behavior of the moving object, centroid of the object was computed to analyze the position of the moving object. However, in this work, the cameras' used were fixed and cannot follow moving object [5]. Another set of authors used neural network to track an object, the method utilize one to one organizing map to model a dynamic background and tracks object from video as well as static object/image. It was noticed that, this method involves computational complexity and this makes tracking difficult [6]. In a separate work, a particle filter approach was performed, the work established to track and predict non-linear, non Gaussian moving object in a certain environment. In this work, histogram colour of every object was obtained and sampled. The particle approach was found to be limited by the volume of combined foreground predicted information. Another author used Kernel based algorithm, in this method, tracking was performed by calculating moving object velocity and shape represented by a potential object region, from one frame to the next frame. Although, the method have a good directional selectivity it was observed that it has limitation since it used real filter which cannot track non-linear motions [8]. In another review the author [9], worked on baseline approach, the approach received input and image that depicts object of interest O and a video V of N frames and predict instances of this object. The similarities against all the frames of the video are evaluated stored in bounding box the Coordinates of the upper-left corners (x, y) calculated to tracks object. The major limitation observed in the method is that the process is slow.

The remaining parts of the work are organized as follows, 2 system description, 3 modeling and simulation of servomotor and ANFIS controller, 4 result and discussions, 5 summary conclusion and recommendation for further studies.

3 System Description

Fig.1 is the complete block diagram for object tracking system. The tracking system is made up of one charge couple device (CCD) camera, two servomotors and an ANFIS controller. The CCD video camera is mounted on elevator motor shaft to pan the camera field of view, whereas, the azimuth motor moves both the elevator motor with the camera to tilt the camera field of view. The video output of CCD camera and the motion/position of camera are the feedback signal to the input and output of the tracking system respectively. Consequentially, CCD camera is used as an image sensor and to measure the position of moving target θ_r . The first input to the summer is the set position θ_d , i.e the desired position of the azimuth or elevation motor. The second input is the feedback signal, the current position θ_r of

the object from the camera. The difference between the two inputs θ_r and θ_d , is called position error signal $\theta(e)$, is given to the controller that reads the signal and produce appropriate output signal ω . The controller output reaches the motor driver, which produces a proportional output to rotate the respective motor in either direction according to the sign of the error signal. As the desired position of the object is approached, the error signal is reduced to zero and motor stops. In order to have stable focus with the CCD camera, the targets are automatically locked whenever the camera sensor senses that the object is at the centre of the camera field of view. Target locking is the act of maintaining the target in the camera sensor's center field of view. Under target motion, the target is tracked continuously and to have the object in center of image, the camera is moved in Pan (elevation) and tilt (azimuth) direction according to target position in image. The two servomotors rotate from 0 to $\pm 90^\circ$ along Azimuth and Elevation angles. Object Segmentation is carried out once the object is within the camera field of view.

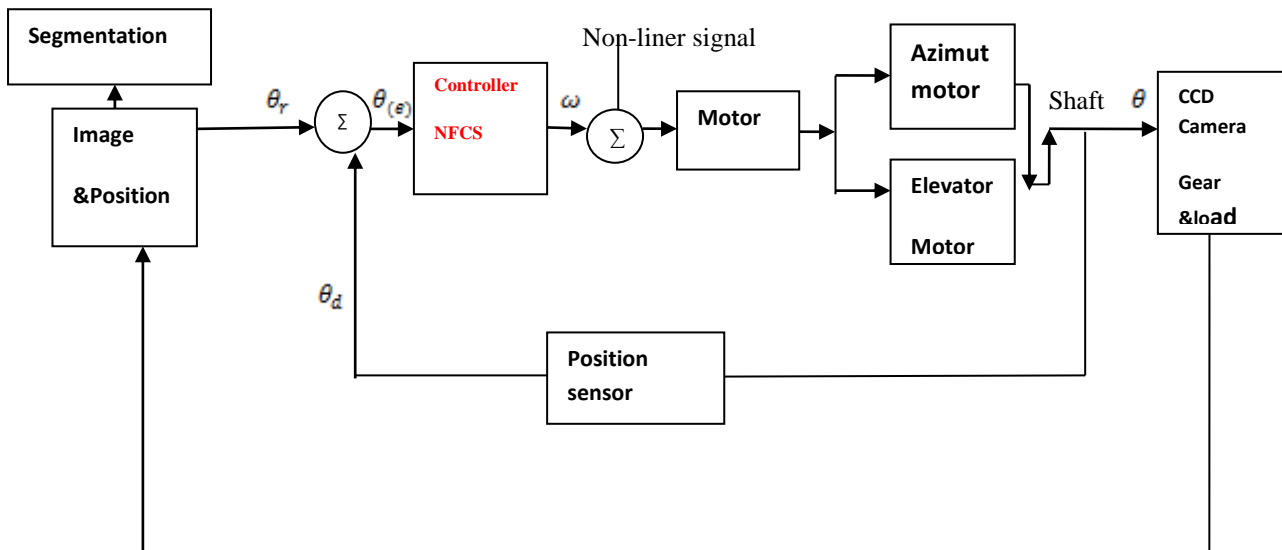


Fig.1 block diagram showing connected systems for object tracking

3.1 Modeling of D.C servomotor

First DC servomotor which positions the system vision (camera) is modeled mathematically for analytical applications. Figure 2 shows the complete parts of the servomotor.

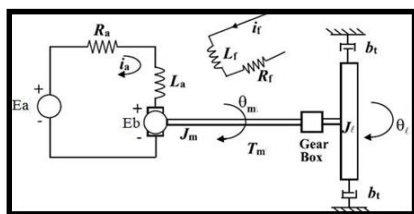


Fig 4 Armature controlled DC servo motor

For the armature controlled DC servomotor in Figure 2 the field current i_f is constant and the torque T_m generated by the DC motor shaft is given by:

$T_m = K_t i_a$ Where K_t is the given motor torque constant in (N-m/A) and i_a is the armature current in (A) [12]. The back

emf induced is directly proportional to the armature angular velocity

$\omega_m(t) = \frac{d\theta_m}{dt}$ where $\theta_m(t)$ is the angular velocity of the motor shaft thus, E_b

Where K_b is a given motor constant (Volt-sec/rad). Fig. 2

The angular speed of armature control motor $\omega_m(t)$ is controlled by armature voltage E_a . The differential equation relating armature current i_a back emf E_b is obtained by Kirchhoff's Voltage law as;

$$L_a \frac{di_a}{dt} + R_a i_a + E_b = E_a$$

since the DC servomotor shaft is connected to a gear box of given gear ratio K_g and the load which is the camera is attached to the output shaft of the gear-box. The gear ratio K_g is given by

$K_g = \frac{n_l}{n_m}$ where n_l and n_m are number of teeth on the load-side and the motor gears, respectively. The gear ratio

K_g relates the motor shaft angular position θ_m to the gearbox output shaft angular position θ_l by $K_g = \frac{\theta_m}{\theta_l}$. In addition J_L load inertia acting at the output shaft of the gearbox when reflected at the motor shaft is give by $\frac{1}{K_g^2} J_L$

Using Newton's moment balance equation at the motor output shaft [13].

$$T_m = J_m \frac{d^2 \theta_m}{dt^2} + \frac{1}{K_g^2} J_L \frac{d^2 \theta_m}{dt^2} + \frac{1}{K_g^2} b_t$$

This can be rewritten as

$$J_{eq} \frac{d^2 \theta_l}{dt^2} + b_t \frac{d \theta_m}{dt} = K_g T_m$$

Where $J_{eq} = K_g^2 J_m + J_L$ is the total load inertia reflected at the motor shaft and b_t is the rotational viscous frictional constant.

Taking the lap lace transform of the last four equations to eliminate the variables T_m, E_b , and i_a .

$$\frac{\theta_l(s)}{E_a(s)} = \frac{K_g K_t}{S(L_a J_{eq} S^2 + (L_a b_t R_a J_{eq}) S + R_a b_t + K_g^2 K_t K_b)}$$

The transfer function from input E_a to output ω_l is give by

$$\frac{\omega_l(s)}{E_a(s)} = \frac{K_g K_t}{(L_a J_{eq}) S^2 + (L_a b_t R_a J_{eq}) S + R_a b_t + \frac{\omega_l(s)}{E_a(s)} K_g^2 K_t K_b}$$

Now, assuming two real, simple roots of the characteristic equation can be obtained as P_e and P_m , using partial fraction expansion

$$\frac{\omega_l(s)}{E_a(s)} = \frac{A_e}{S + P_e} + \frac{A_m}{S + P_m}$$

Using the inverse Laplace transforms the forced response of the system (with zero initial condition) to the input $E_a(t)$ is given by;

$$\omega_l(t) =$$

$$\int_0^t (A_e e^{-p_e(t-q)} + A_m e^{-p_m(t-q)}) E_a(q) dq$$

In most practical application of armature control DC motor, $P_e \gg P_m$; that is the electrical subsystem respond considerably is faster than the mechanical subsystem. Hence, the first exponential term decay rapidly thus the respond $\omega_l(t)$ is dominated by mechanical subsystem $\frac{A_m}{S + P_m}$. in D.C servomotor the influence of electrical subsystem component $\frac{A_e}{S + P_e}$ on the response $\omega_l(t)$ is commonly neglected, viewed

as neglecting the armature inductance effect L_a , this simplification yields a first-order transfer function model which relates the DC motor load angular velocity response ω_l to the armature voltage input E_a given by

$$\frac{\omega_l(s)}{E_a(s)} = \frac{K_g K_t}{R_a J_{eq} S + R_a b_t + K_g^2 K_t K_b}$$

In S.I unit K_t and K_b numerical values are identical Hence, the transfer function model can be written as

$$\frac{\omega_l(s)}{E_a(s)} = \frac{K}{\tau S + 1}$$

Where K and τ are the D.C gain and mechanical time constant of D.C servomotor respectively [14].

3.1.1 Servomotor position control with position feedback

$\frac{\theta_l(s)}{E_a(s)}$ Is given as;

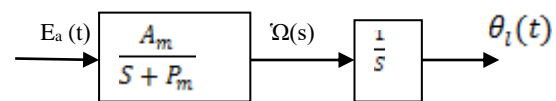


Fig 3 Servomotor transfer function model

The s-domain unit step response is

$$\theta_l(s) = \frac{A_m}{S(S + P_m)} \frac{1}{s}$$

The final value of the response is $\lim_{t \rightarrow \infty} \theta_o(t) = \lim_{s \rightarrow 0} s \theta_l(s) = \infty$. That is, the position response is unbounded. In order to control the output position to follow an input command, consider the addition of a position feedback and feedback is given by;

$$E_a(s) = K_p [\theta_i(s) - \theta_l(s)] \cdot \Omega_c(s)$$

As shown in Figure 4 the purpose of this system is to have the output angle $\theta_l(t)$ follow the input angle $\theta_i(t)$ [15].

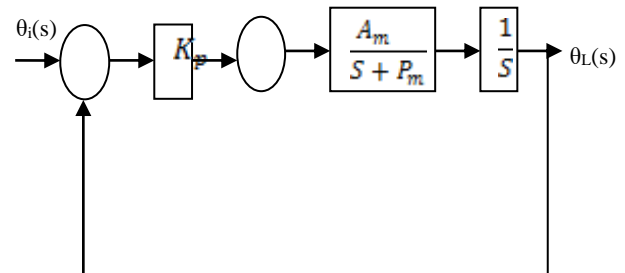


Fig.4 Servomotor position control using position feedback

Applying Mason's gain formula and show that the overall transfer function is

$$\frac{\theta_L(s)}{\theta_i(s)} = \frac{K_p A_m}{s^2 + P_m s + K_p A_m}$$

Using parameters obtained from servo motor vendor's in table 1, A_m and P_m are calculated for both azimuth and elevation servo motor.

Table 1
Parameters of Model with D.C Servomotors

PARAMETER	DEFINATION	ELEVATION	AZIMUTH
Δ	Motor Dampening constant [Nms/rad]	0.04	0.01
J_m	Motor Inertial Constant [Kgm ²]	0.00001	0.001
J_l	Load inertia [Kgm ²]	0.0044	0.00001
$J_{eq} = K_g^2(J_m + J_{tac}) + J_l$	Equivalent inertia [Kgm ²]	0.00012	0.000013
K_B	Back emf Constant [Vs/rad]	0.055	0.5
B_{eq}	Equivalent friction required to the secondary gear [Nm/(rad/s)]	0.001	0.01
K_g	Gear Ratio	0.1	0.1
K_T	Motor Torque Constant [Nm/A]	0.00006	0.5
L_a	Motor Armature Inductance [H]	0.0018	0.45
R_a	Motor Armature Resistance [Ω]	0.2	4.5
V	Voltage (D.c) [V]	24	10
η_{rl}	Motor efficiency due to rotational loss	0.87	0.87
η_g	Gear box efficiency	0.85	0.85
W	Weight [Kg]	0.27	1
K	Gain of Potentiometer error (vs/pi) v/rad	24/pi	10/pi

For The Azimuth Servo motor

$$A_m = \frac{\eta K_m K_g}{R_a J_{eq}} = 288.76$$

$$P_m = \frac{B_{eq}}{J_{eq}} + \frac{\eta K_g^2 K_m^2}{R_a J_{eq}} = 40.40$$

Using $k_p=1$ from mat lab Substitute for A_m and P_m

$$\frac{\theta_L(s)}{\theta_i(s)} = \frac{288.76 K_p}{s^2 + 40.40 s + 288.76 K_p}$$

The servomotor transfer function model with gear and position feedback was obtained by

substituting K_p , transfer function model used in this work to control the output angular position θ_L of the DC servomotor with a camera mounted on the shaft. The output response follows the input angle θ_i of azimuth and elevation servomotor as desired for controller tracking of positions. [15].

$$\frac{\theta_L(s)}{\theta_i(s)} = \frac{288.76}{s^2 + 40.40 s + 288.76}$$

For The Elevation Servomotor

$$A_m = \frac{\eta K_m K_g}{R_a J_{eq}} = 42.3$$

$$P_m = \frac{B_{eq}}{J_{eq}} + \frac{\eta K_B^2 K_m^2}{R_a J_{eq}} = 9.6$$

$$\frac{\theta_L(s)}{\theta_i(s)} = \frac{42.3}{s^2 + 9.6s + 42.3}$$

$$\frac{\theta_L(s)}{\theta_i(s)} = \frac{42.3K_p}{s^2 + 9.6s + 42.3K_p}$$

3.2. Adaptive Neuro-Fuzzy (ANFIS) system controller design

Having obtained the servomotor transfer function models for positioning the system vision (camera) it is necessary to design an intelligent non-linear self-tuning controller i.e the ANFIS that controls the servomotors in azimuth and elevation positions to track objects using two dimensional coordinates in a given scene. To obtain the design, the ANFIS must generate change in angular reference position E and derivative position error DE for both the azimuth and elevation axes defined by equations below.

Error (E) = (Desired angular Position–Actual angular Position)

Change in Error (DE) = (Current Error- Previous)

In this model, a first order Sugeno-type fuzzy inference is used for ANFIS and the typical fuzzy rule takes the form of

If x is A_i and y is B_i then,

$Z = f(E, DE)$

Where A_i and B_i are fuzzy sets in the antecedent and $z = f(E, DE)$ is a crisp function in the consequent. The significant of each layer and operation of input output ANFIS structure considered are:

Layer 1: This layer (the fuzzification layer) enables the entry of raw data or crisp inputs from the target system into ANFIS. It is composed of a number of computing nodes whose activation functions are fuzzy logic membership functions, taken here is triangular. Each adaptive node generates the membership grades called fuzzy spaces for the input vectors $i A$, $i = 1, \dots, n$ and $i B$, $i = 1, \dots, n$ where n is the number of membership. Functions of the inputs (E and DE) chosen as $n = 4$. The degree to which the inputs lie within the fuzzy space is given a value normalized between -4 and 4.

$$O_{A,i}^1 = \mu_{A_i}(E), O_{B,i}^1 = \mu_{B_i}(DE), i=1, \dots, n$$

Layer 2: Is the rule layer where each node is fixed. Once the locations of inputs in the fuzzy spaces are identified, the product of the degrees to which the inputs satisfy the membership functions is found. This product is called the firing strength of a rule whose output is given by

$$O_i^2 = W_i = \min(\mu_{A_i}(E) \cdot \mu_{B_i}(DE))$$

In other words, it selects the minimum value of the inputs. In this layer, the total number of Takagi-Sugeno rules used is 16 since the membership function is 4 (4×4) = 16.

Layer 3: This is the normalization layer in which the ratio of each rule's firing strength is calculated with respect to the sum of the firing strengths of all the rules. Each node in this layer is fixed. The node output is the i^{th} input activation level divided by the sum of all the activation levels of the other inputs, as given below

$$O_i^3 = \bar{W}_i = \frac{W_i}{\sum_{i=1}^n W_i}$$

Layer 4: In layer 4, the defuzzification layer, the output of each node is the weighted consequent value. Adaptive node i in this layer calculates the contribution of the i rule towards the overall output, with the following node function

$$O_i^4 = \bar{W}_i Z_i = \bar{W}_i (P_i E + DE q_i + r_i)$$

Layer 5: Layer 5 is the summation layer and its output, which is the sum of all the outputs of layer 4, gives the overall output for the respective inputs within the fuzzy space. The single fixed node in this layer computes the overall output as the sum of each rule's contribution given as

$$O_i^5 = \sum_{i=1}^n \bar{W}_i Z_i = \frac{W_1 Z_1 + W_2 Z_2}{W_1 + W_2}$$

3.2.1 Anfis training for tracking on trajectory with chaotic data

Before ANFIS can be used to predict position of object on a trajectory, training data are presented to the ANFIS. The data presented is for training (estimating) membership function Parameter which fully represents the feature of FIS intending to model. After training, the rules remain so that when new input data is presented to the model, the rules provide a corresponding reasonable output [16]

In this paper, non-linear trajectory movement along x and y is similar to the non-linear movement of object on scene. The optimization technique used is a hybrid learning algorithm that minimizes the error between the ANFIS model and the real system using training data from the target system to generate signals that propagate backwards and forwards and update the parameters. The parameters to be trained are A_i , and B_i of the premise parameters and p_i , q_i and r_i of the consequent parameters. The MATLAB/ANFIS Editor GUI window is used in this work. The ANFIS Editor GUI window includes four distinct areas to support this workflow in realizing this task.

3.2.2 Training procedures

- Loading, Plotting, and Clearing the Data
- Generating or Loading the Initial FIS Structure
- Training the FIS
- Validating the Trained FIS

For generating FIS structure, the triangular membership function (MF) was used for the input variable and output type is linear. The number of MFs for the input variable E and DE is 4 each hence the number of rules is $4 \times 4 = 16$ function for E and DE before training

3.2.3 Simulink Implementation of ANFIS for data training

To implement training procedure for ANFIS desired input/output target control of the system the procedures are as follows;

3.2.4 Loading and training data.

The chaotic data which represent the chaotic trajectory position intended to model are loaded

and checked in ANFIS Matlab GUI shown in figure 5 using the *anfisedit* command window which pops up the ANFIS GUI. Using load data button on ANFIS Matlab GUI, the data representing the model is loaded from disk. The blue small circles represent the load data and the plus sign represent checked data. Fig 6 shows the ANFIS training using the hybrid approach the training error is the difference between the training data output value and the output of the fuzzy inference system. The training error records the root mean square error (RMSE) for each training epoch of the data set. Fig 7 shows how FIS can track train data. Fig 8 and 9 represent the triangular membership function used in training. The rule base for controlling servomotors and the five-layer model structure with 2 inputs and 1 output is depicted in fig 10 and 11.

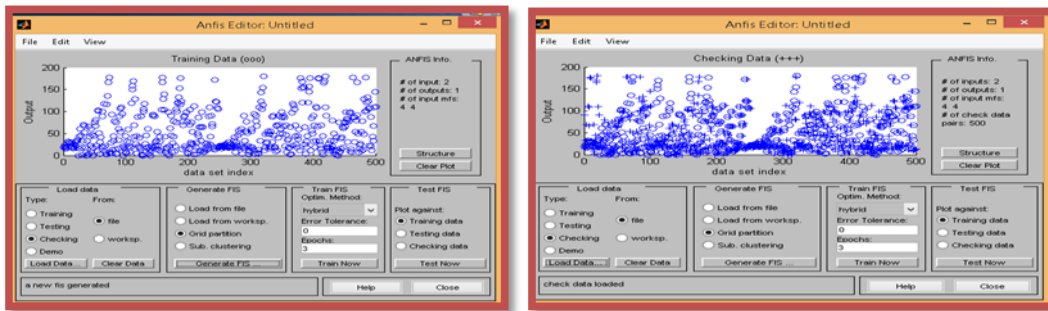


Fig.5 Loading and checking data for training for training in Matlab Anfis Graphical user interface

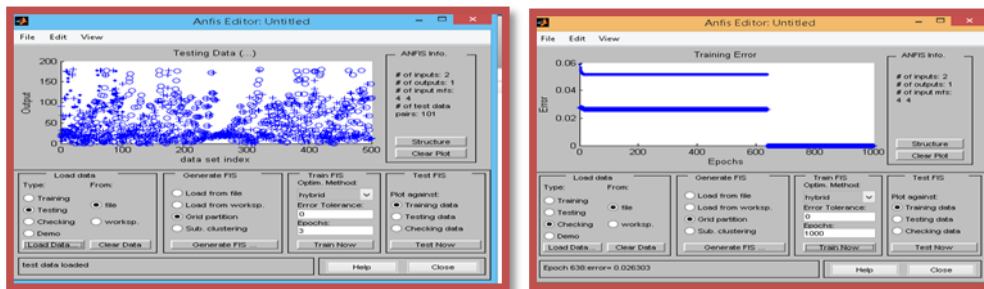


Fig 6 training the output FIS checking the FIS with the minimum error in Graphical user interface

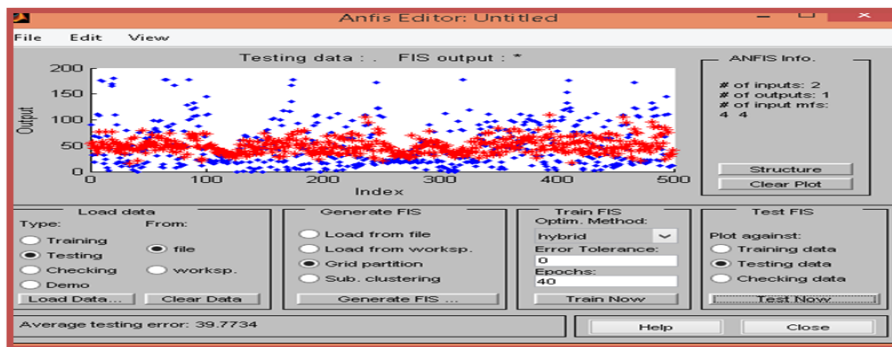


Fig 7 output FIS structure checking trained data

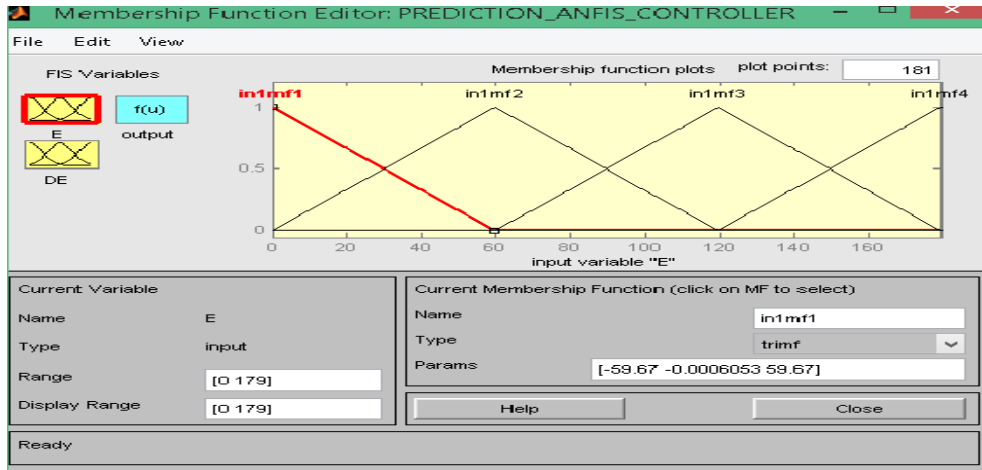


Figure 8 Membership function for training

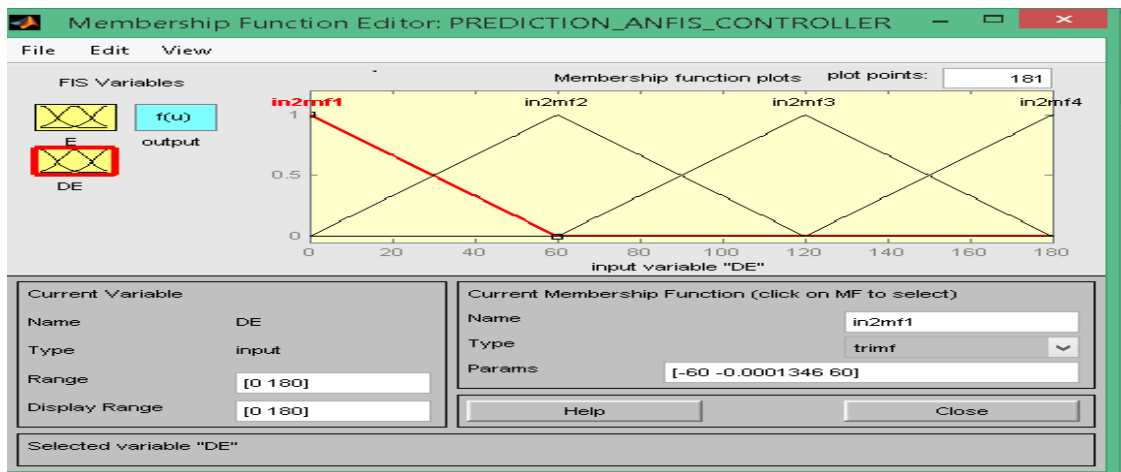


Figure 9 Membership function for training

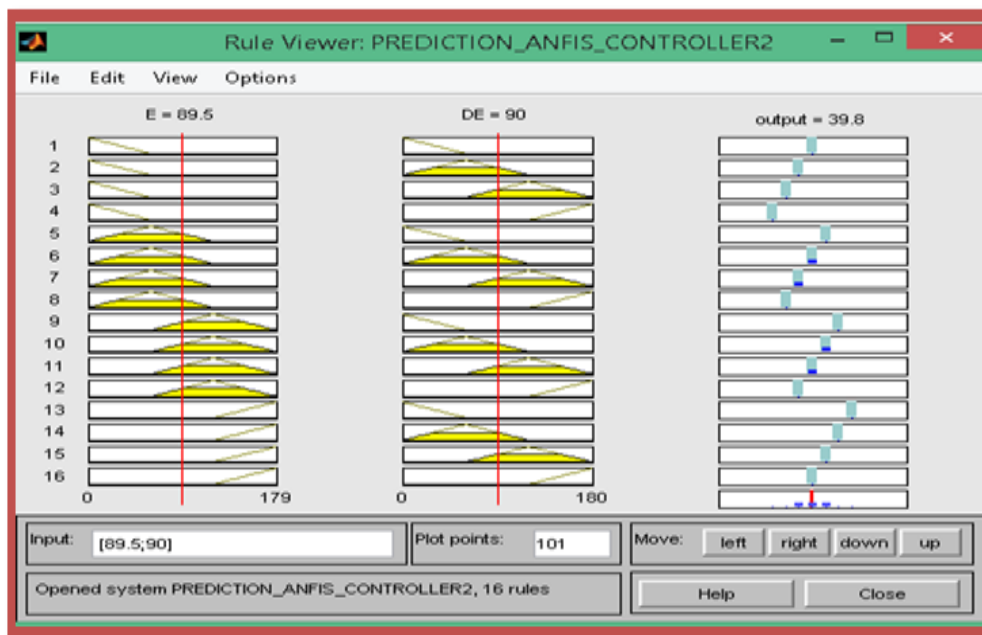


Fig 10 ANFIS control Rule base after training.

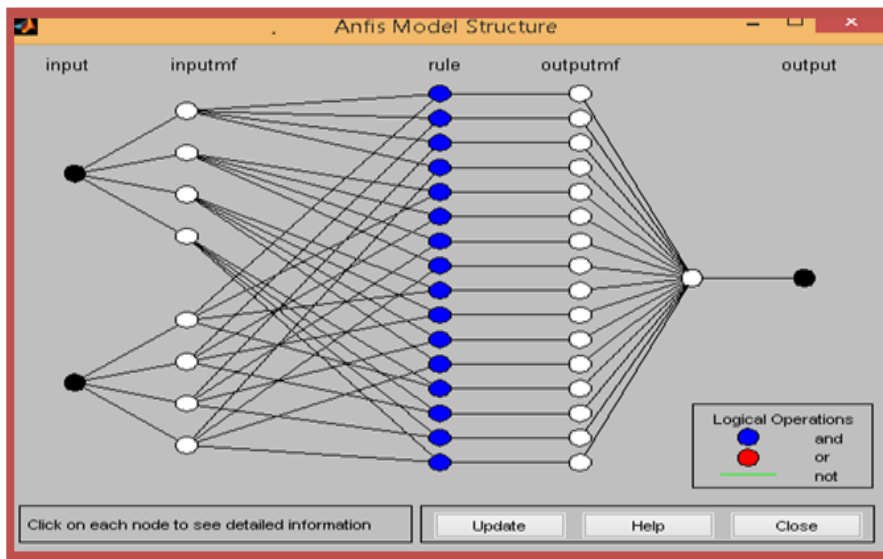


Fig 11 5-Layer ANFIS model structure with 2 inputs & 1 output

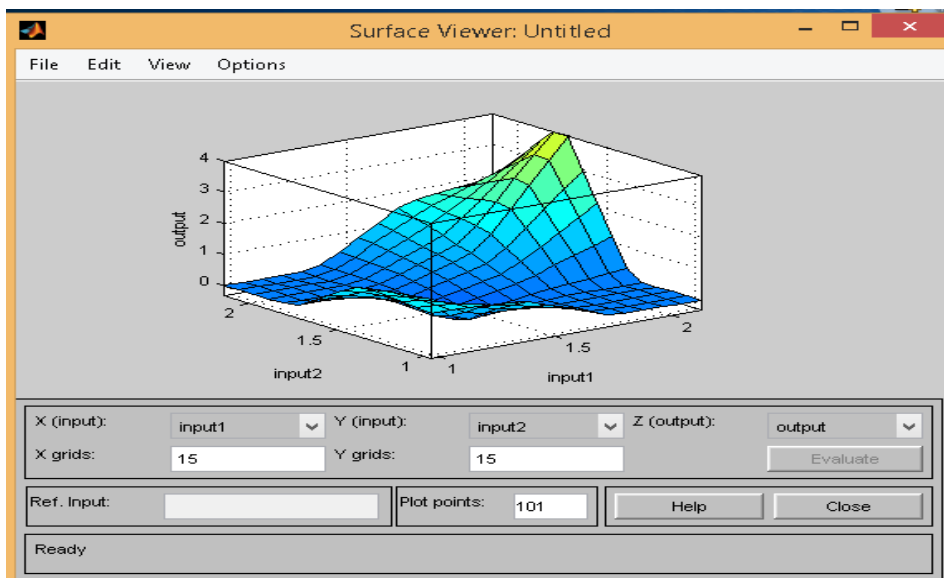


Fig 12 Surface Viewer for two inputs with one output

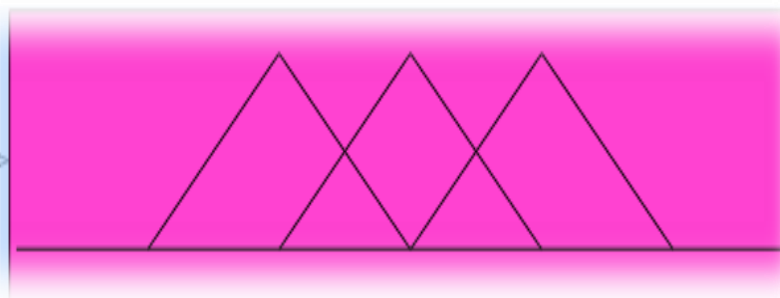


Fig 13 self-turning train FIS embedded (ANFIS) controller

3.3 Servomotors with Anfis Model

Fig 14 and 15 depicts the designed ANFIS model connected to azimuth and elevation servomotors. The connection was simulated to obtain desired performance by the ANFIS

controller. The two models are masked connected to video source with camera mounted shown in Fig 16 to obtain the two dimension track.

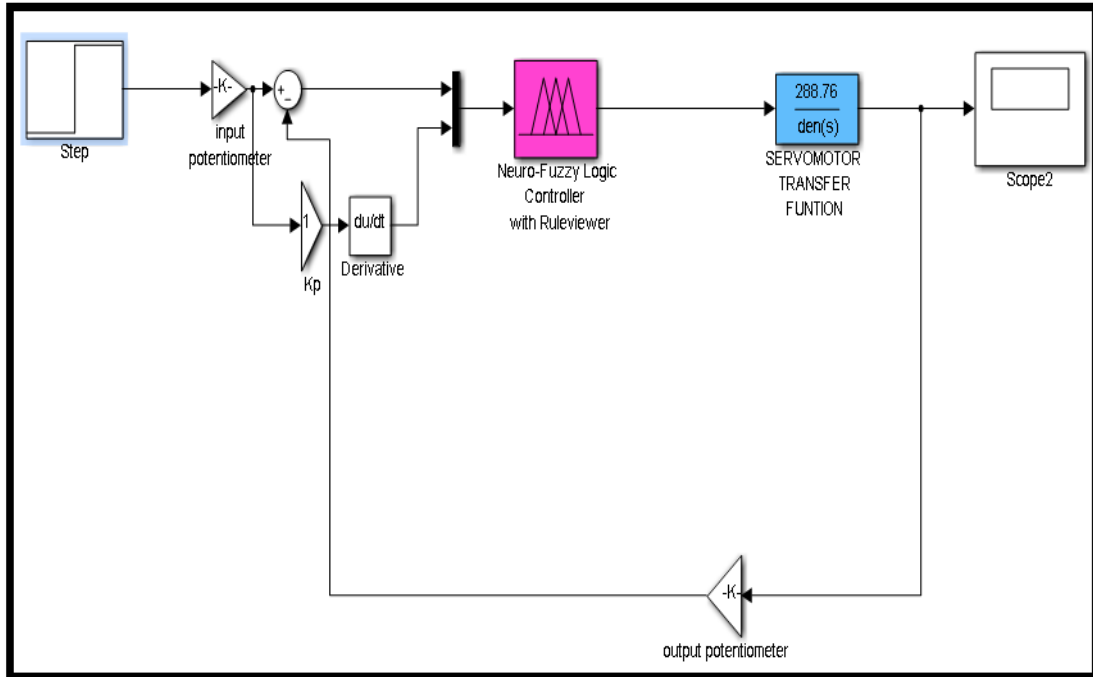


Fig 14 ANFIS model controller with azimuth servomotor with step input

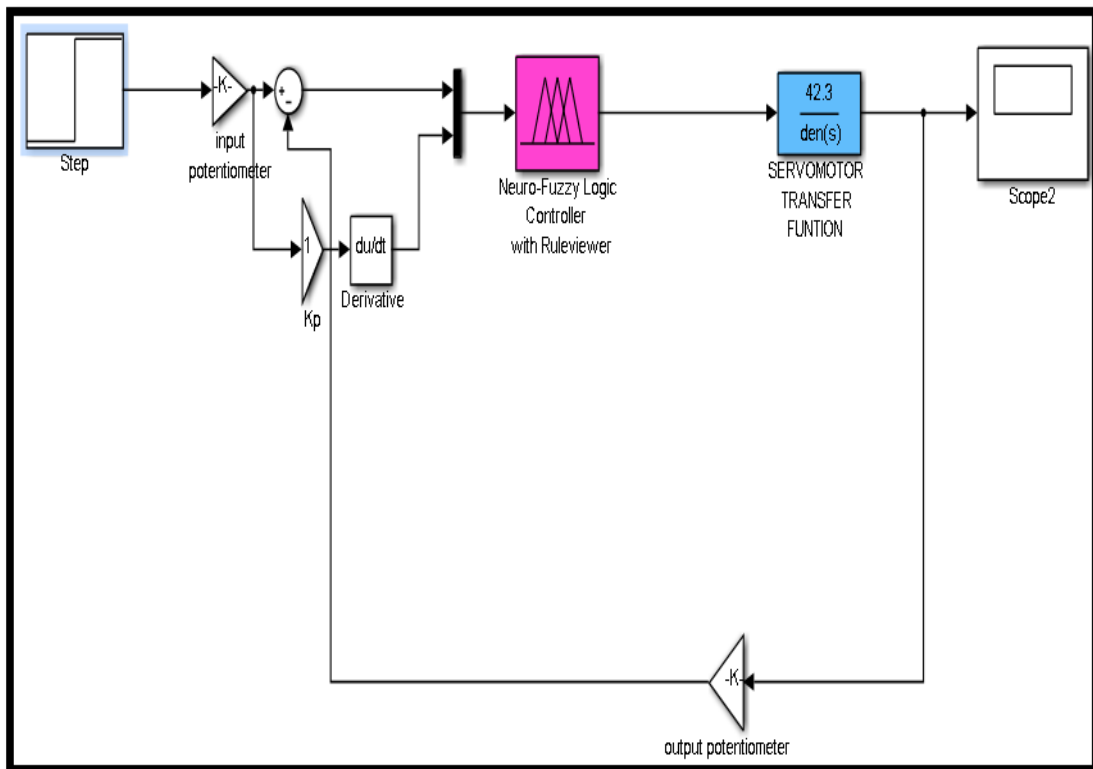


Fig 15 ANFIS model controller with elevation servomotor with step input

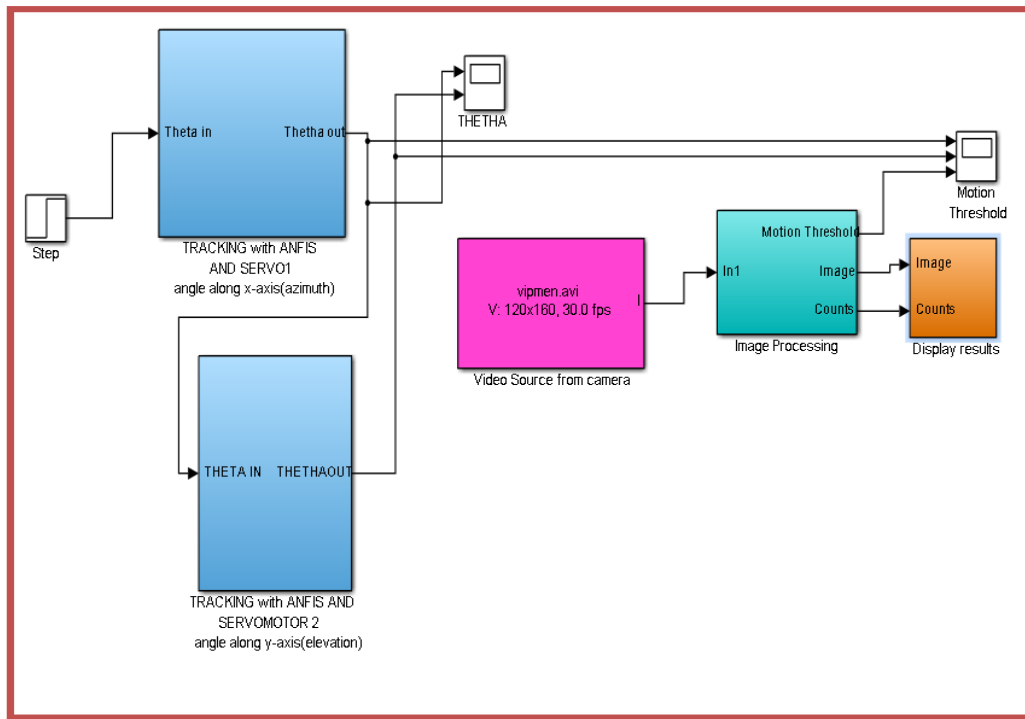


Fig 16 Model Block for object tracking and Motion Prediction

4. Result and Discussions.

The work has been studied by simulation. First, the servo motor transfer functions was simulated using step input for both azimuth and elevation servos without controller, the result is shown in Figure 17. The model servo's without controller were further simulated using angular input signals. With 1degree square Angular positions and sinusoidal signal result figure 18 and 19 were obtained respectively. The result shows that the servos followed the angular positions path or trajectory. The performance of the servomotors to track the

path/trajectory in term of transient, significantly improved with introduction of the model ANFIS controller shown in Fig 20. The complete result for the transient performances of the model is summarize in table 2 this shows the transient result of tracking using servomotors in azimuth and elevation connection with and without the ANFIS controller. The result shows a significant robust performance with the ANFIS controller

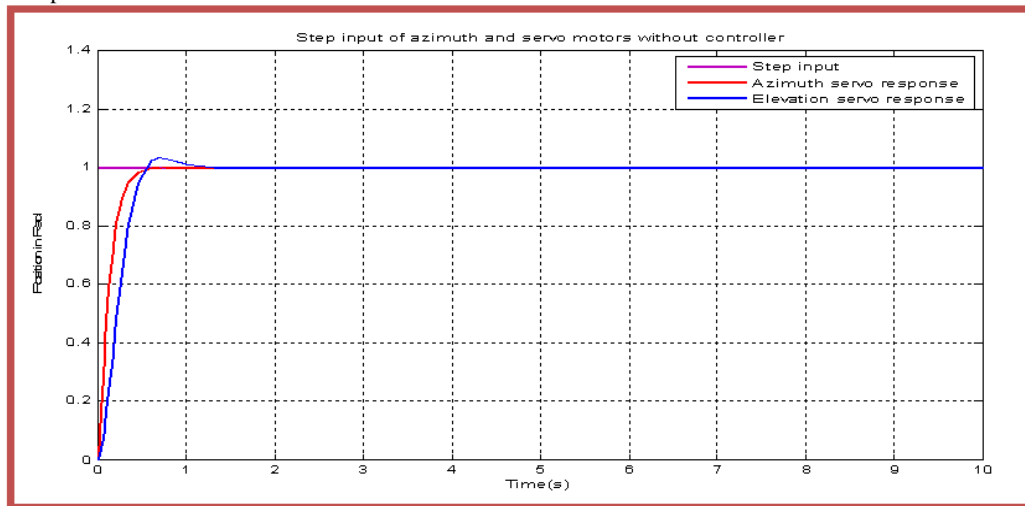


Fig 17 Step response azimuths and elevation servo motor without controller

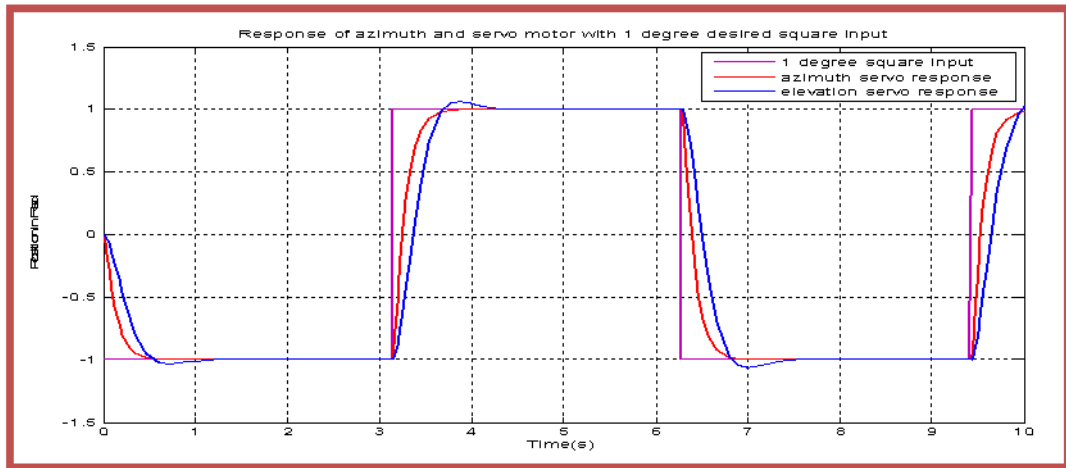


Fig 18 Azimuth and Elevation Servo response with 1 degree square trajectory

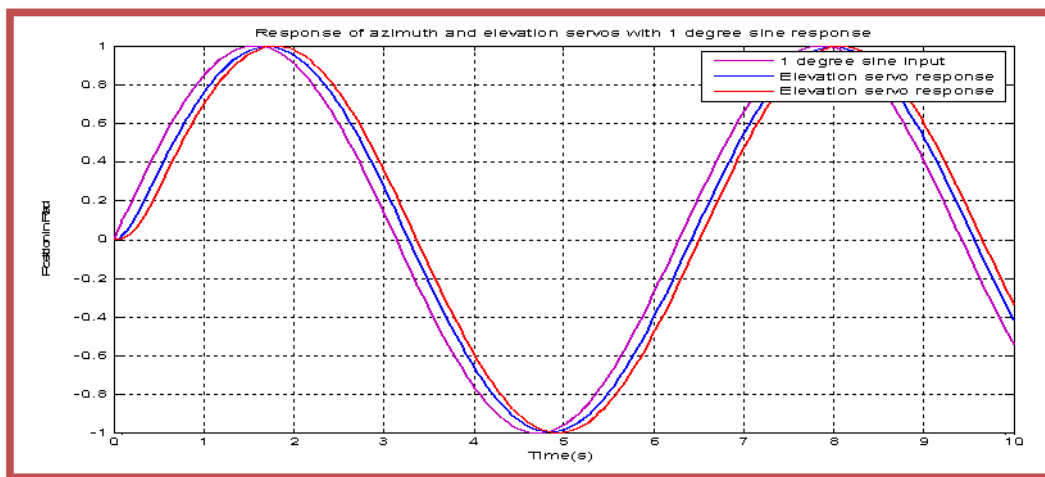


Fig 19 Azimuth and Elevation Servo position response with 1 degree sinusoidal trajectory

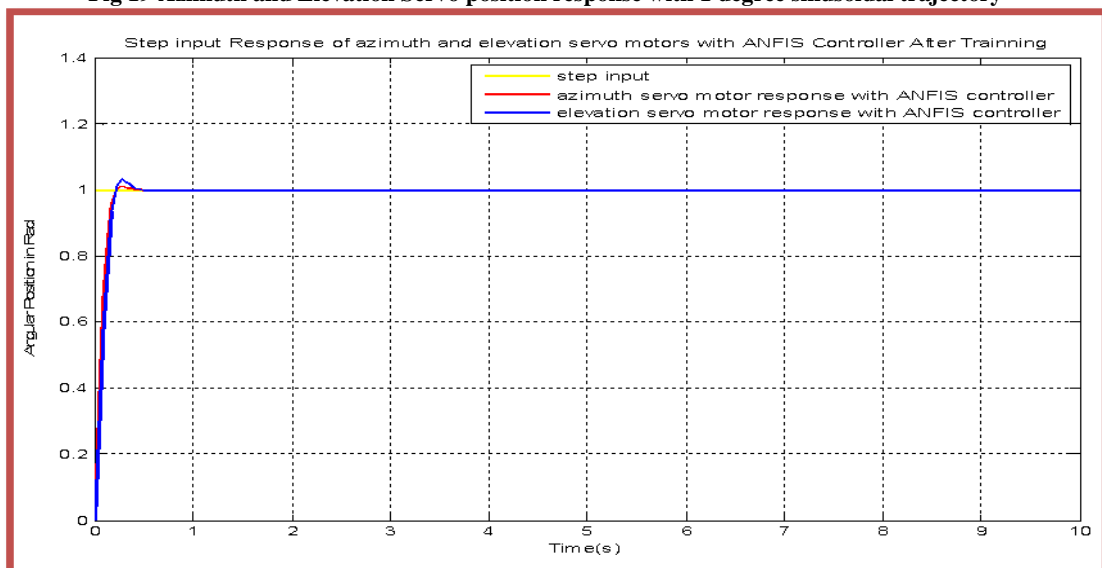


Fig 20 Step responses with azimuth and elevation servo motor position with ANFIS controller

Table 2 Comparison of tracking time response results of azimuth and elevation servo with and without ANFIS controller.

Characteristic specification	Azimuth Servo Without controller	Azimuth Servo With ANFIS controller	Elevation Servo without controller	Elevation Servo with ANFIS controller
Rise time t_r (s)	0.6	0.1	0.6	0.3
settling time t_s (s)	0.6	0.5	1.2	0.5
Peak time t_p (s)	1.0	0.2	0.7	0.2
Delay time t_d (s)	0.3	0.2	0.3	0.1
Maximum Overshoot M_p (%)	1.1	1.0	1.2	1.0

4.1 Result Comparison of Anfis with PID and Fuzzy

To show the performance of ANFIS controller in comparison to the conventional PID and FUZZY on the same servo motor transfer function The result plot for the responses is displayed in scope

plot fig 21 and is summarized in table 3 ANFIS controller output was found the best in terms of faster rise time, settling time and position stabilization.

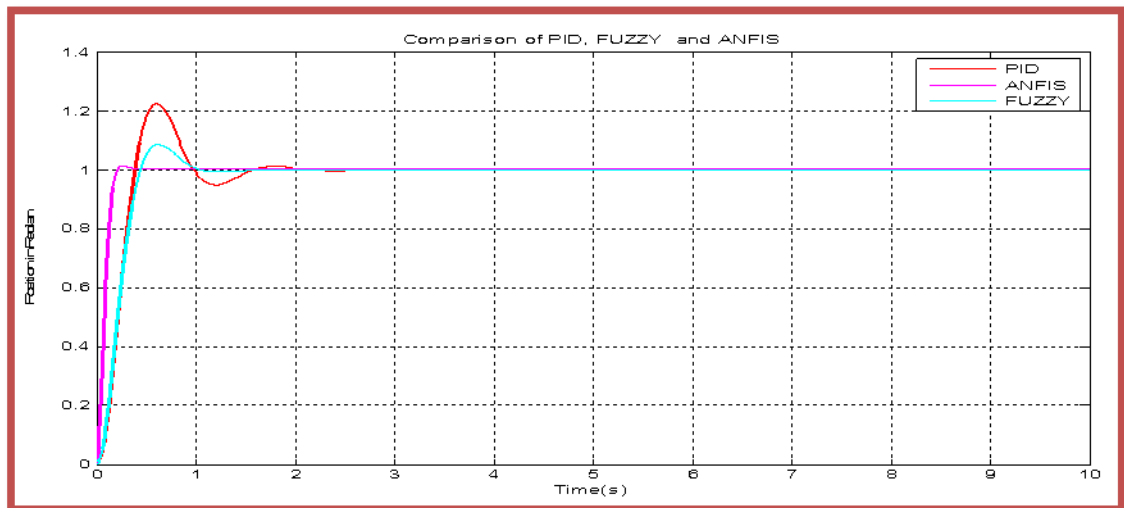


Figure 21 Step input Comparison Plot of PID, FUZZY and ANFIS

Table 3 Step input transient result of PID, FUZZY and ANFIS

Characteristics	PID Controller	FUZZY Controller	ANFIS Controller
t_r (s)	0.6	0.5	0.2
t_s (s)	2.0	1.1	0.5
t_p (s)	0.7	0.6	0.3

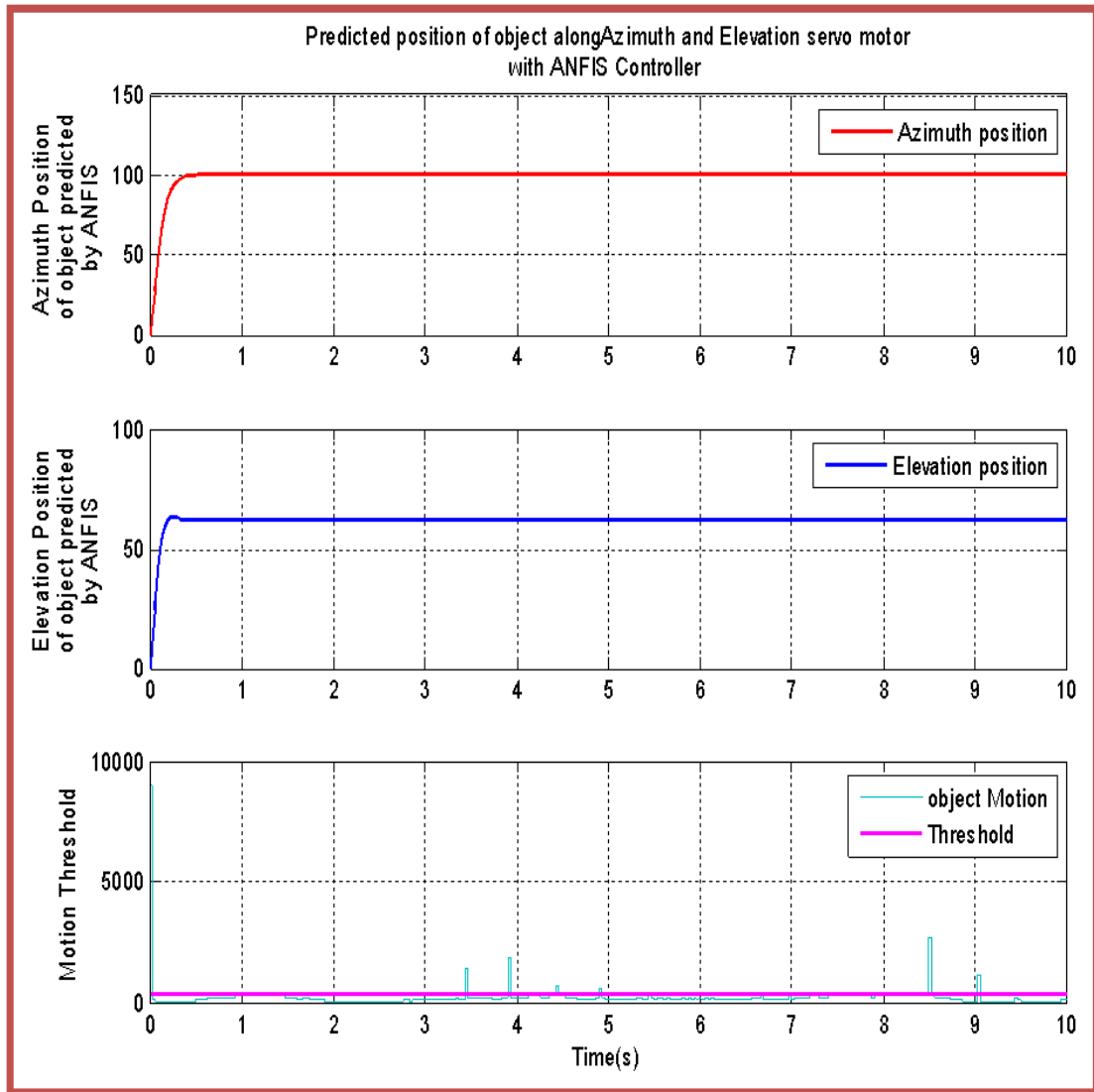


Fig 22 Response of azimuth and elevation positions with ANFIS controller with motion prediction.

Figure 22 shows the separate 2-dimension track position result and motion prediction. The red line in the figure represents the azimuth position and the blue line represents the elevation position. The purple line represents motion threshold during segmentation i.e. all signals above the threshold represent number of motion captured by segmentation.

4.2 Tracking chaotic trajectory with Anfis

The chaotic trajectory result generated using mackley Glass chaotic time series model which is sensitive to initial condition on which the Anfis is to be train for azimuth and elevation trajectory respectively. This chaotic trajectory is necessary since tracking object positions in real life situations

are nonlinear (chaotic). Using chaotic signal input the ANFIS without training were used to track various angular positions displayed shown in Figure 23. However, using ANFIS to learn about this trajectory will produce a better result. The data are trained and validated (checking and testing) on the trajectories. The result plot result Figure 23 shows a trajectory (blue signal) and ANFIS output (red) before training. It can be observed that the ANFIS path which represented by red signal is not able to track the chaotic trajectory represented by blue signal. However Figure 24 shows the plot result of the two signals after ANFIS training. It was noticed that the train ANFIS signal path tracks the trajectory path and was able to follow the chaotic trajectory of object

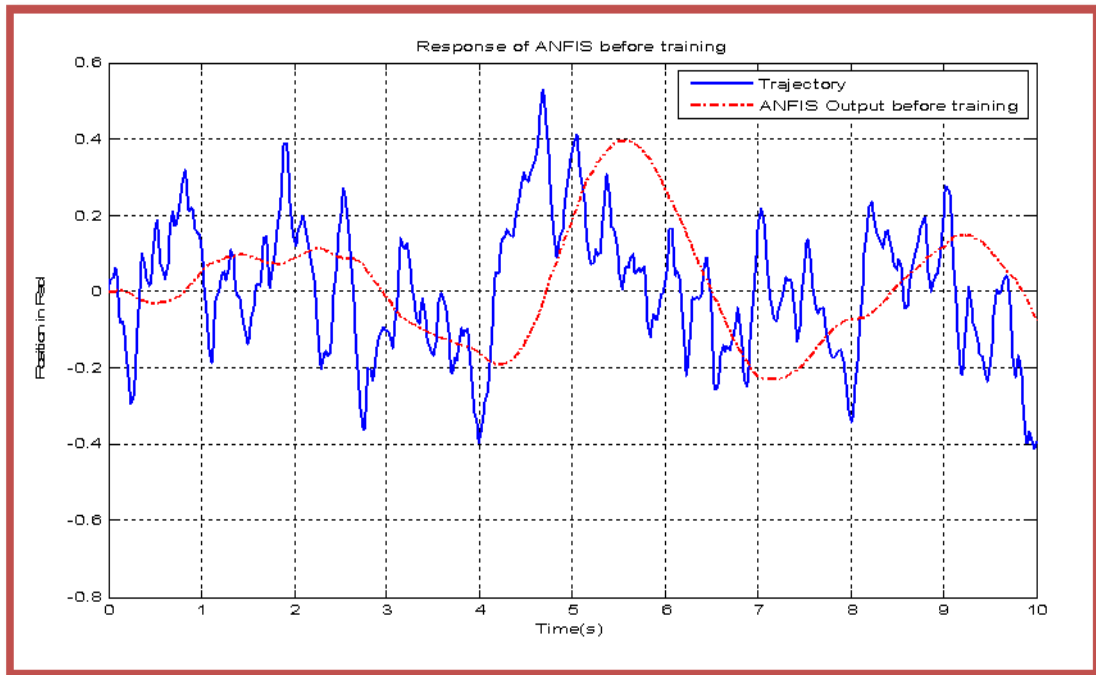


Fig 23 Tracking position along trajectory with servo motor before training

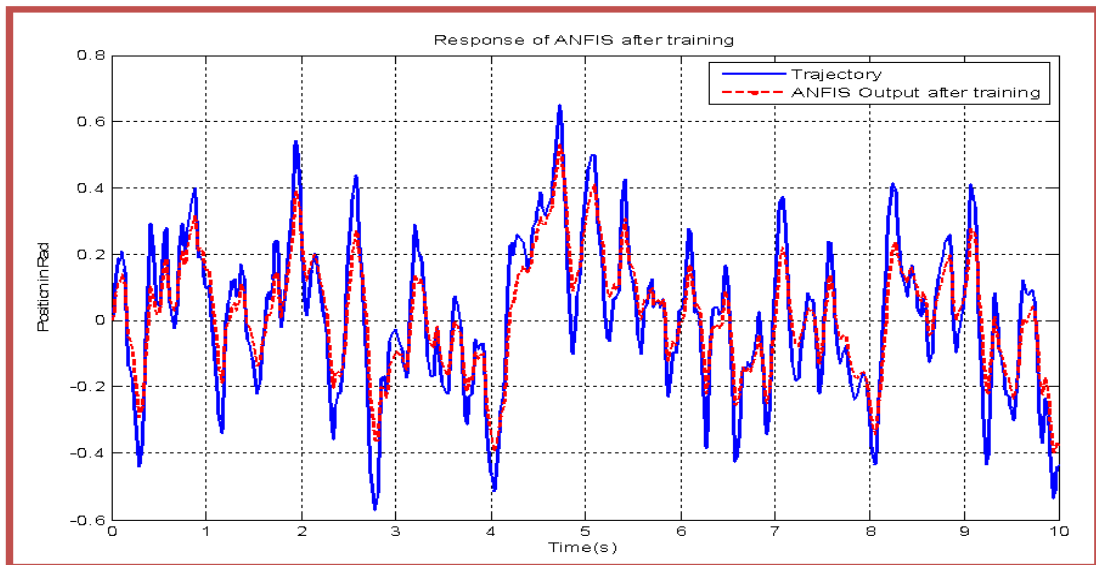


Fig 24 tracking position along trajectory with servo motor after training

5.1 Conclusion

The objective of this paper to design ANFIS Controller for self tuning of DC servomotor has been achieved. ANFIS controller is self tuning the self tuning results a robust control In ANFIS hybrid system. Neural networks are used to tune membership functions of fuzzy systems that are employed as decision-making systems for controlling equipment. The ANFIS controller is efficient with servomotors which have nonlinear characteristics. The prediction by ANFIS compensates the System delay and thus allows precise and fast motion

control viewed through segmentation. ANFIS controller output have faster rise time, settling time, reduced time delay and faster position stabilization in tracking object

5.2 Recommendation

Further work may focus on the hardware implementation application of the developed Neuro-fuzzy system to achieve automatic and real time object tracking with video camera

References

Matlab Image Processing Toolbox User Guide.
(2004).

- [1] Sunitha.M, S. (2013). Real time object Tracking. *International Journal of Emerging Technology and Advance Engineering.*, 3(3), 2250–2459.
- [2] Ramya G, (2014). Real time visual surveillance. *Global Journal of Researches in Engineering*, 14(6).
- [3] Jain A. (1999). Object tracking using Fuzzy Logic for khepera 11 Robot. *Journal of Electrical and Electronics Engineering*, 46(5), 315.
- [4] Lopes. (2011). *Fuzzy Logic based approach for object features.*
- [5] Landge. (2014). Tracking using Background Subtraction. *An international Journal of Advanced Research in Electrical, Electronics and Instrumentation Engineering*, 3(7), 45-65
- [6] Ghate & Gawi. (2014). *Object detection using Neural Network. 1(2)*.
- [7] Zhong QU, Quingqing Zhang, T. G. (2012). Moving Object Tracking based on Codebook and Particle Filter. *Internatinal Workshop on Information*
- [8] Yilmaz Alper, J. O. and S. M. (2006). Object Tracking: A survey”. *ACM Compt. Surv.*, 1–45.
- [9] Evlampios Apostolidis. (2013). Fast object Re-detection and Localization in video For Spatio- Temporal fragmen. In *International Conference on fast* Molina, José M,
- [10] Jesús García, (2003). Neuro-Fuzzy Technique for image analysis. *IEE Journal of Advance Science Technology*, 5(8), 209–231.
- [11] Jang, S. (2015). Fuzzy Control of data systems for moving vehicle using Robust Cotrollers. *Journal of science Mathematics and Physics* , 36-46.
- [12] Sidney R. Bowes, Fellow, Derrick Holliday. (2004). *New Natural Observer Applied to Speed-Sensor less DC Servo and Induction Motors. IEEE Conference Control.*
- [13] Javiya, K. a. (2016). Comparisons of Different Controller for Position Tracking of DC Servo Motor. *International Journal of Advanced Research in Electrical Engineering*, Vol. 5 (Issue 2), 966-967.
- [14] Bolton, W. (*Experiment Note,1999*). pp. 1-10.
- [15] Jane,(Handbook of Servo Control,2014)
- [16] Lofti A. Zadeh and Berkeley, C. (1995). *Fuzzy Logic Toolbox User's Guide.*

Anomaly separation of La, Ce and Nd in Se-Chahun iron ore deposit, Bafq district, central Iran

Mohammadali Sarparandeh
Department of mining and
metallurgical engineering
Amirkabir university of
technology
Tehran, Iran

Ardeshir Hezarkhani
Department of mining and
metallurgical engineering
Amirkabir University of
technology
Tehran, Iran

Bashir Shokouh Saljooghi
Department of mining and
metallurgical engineering
Amirkabir University of
technology
Tehran, Iran

Abstract: Increase in global prices of rare earth elements (REEs) in recent years has attracted many exploration researchers, especially in Iran. There are some promising areas in central Iran which contain significant amounts of light rare earth elements (LREE). Se-Chahun metasomatic iron ore deposit is one of them. Concentrations of La, Ce and Nd are considerable in some parts of this deposit. On the other hand, one of the most important steps in geochemical exploration of precious elements is separation of anomaly from background. For this purpose, some methods such as classical statistics and fractal models are common. However, application and simplicity are the two main parameters for choosing a proper method. In this study, classical statistics approach (using the mean and standard deviation), and also probability graph and C-A fractal model (Concentration Area) were applied for anomaly-background separation of La, Ce and Nd. Comparing the results of the methods with mineralogy and chemistry of the samples, showed that probability graph had the best performance in anomaly separation. Therefore, considering the results as well as simplicity of the method, it concluded that probability graph is more applicable and a better approach in comparison to others.

Keywords: classical statistics; probability graph; C-A fractal; anomaly separation of REEs; Se-Chahun; Central Iran

1. INTRODUCTION

Kiruna-type iron ore deposit of Se-Chahun is enriched in light rare earth elements (LREEs) including La, Ce and Nd. Some studies on Kiruna-type iron oxide-apatite (IOA) deposits in Bafq mining district showed the potential for REEs (i.e. Se-Chahun [5, 35]; Choghart: [34, 37]. In addition, some numerical models were applied to predict the hidden patterns of REEs in Choghart iron ore deposit [34, 46]. The REEs are mainly concentrated in specific types of rocks and deposits. Moreover, they are potentially known as an important by-product of iron oxide-apatite (IOA) deposits [39]. Apatite is the main mineral of REEs in the study area. Furthermore, there are some amounts of monazite. Fleischer and Altschuler [16] showed that in apatites from granitic rocks and granitic pegmatites, Ce is dominant, but some analysis showed maximum amounts of Nd, Gd, Dy, or Yb. In anomaly X of Se-Chahun, Ce, Nd and La are more abundant among all REEs. It should be noted that principally, all deposits contain much more LREE than HREE. Most of the deposits have only few percentages of yttrium and other HREEs [36].

Separation of geochemical anomalies from background is one of the important steps in geochemical explorations. Statistical analysis methods play an important role in separating anomalies from background. These methods focus on the frequency distribution of concentrations [20]. Traditional way of anomaly separation is to use the sum of mean (μ) and standard deviation (S) as the threshold. This method is still used as a practical way. In geochemical explorations, values within the ranges $\mu \pm S$ or $\mu \pm 2S$ are usually defined as the background [1, 3, 6, 19, 32, 38].

Probability graph is one of the best graphical displays of geochemical distributions, which has been originally introduced to geochemists by Tennant and White [42] (quoted from [32]). This method has been used widely by researchers (for example: [1, 33, 40, 45 and others]).

Since Mandelbrot's invention of the concept of fractals [23], fractal and multi-fractal models have been applied for

separation of anomaly from background values. Main applicable fractal models are Concentration–Area model (C–A: [7]), Spectrum–Area model (S–A: [10]), Multi-fractal Singular Value Decomposition (MSVD: [21]), Concentration–Distance (C–D) model [20], mapping singularity technique [11, 12]. These methods are gradually being adopted as an effective and efficient means to analyze the spatial structures in metallic geochemical systems. In this regard, Mahvash Mohammadi, et al. [22] applied the concentration–area model (C–A) to separate the anomaly from background in Khooni mineral district (Central Iran). They compared the results of C–A fractal with U-statistic method and showed that the U-statistics method has performed better than C–A method.

Though it has been some decades since the development of fractal methods, and even before that the classical statistics, geostatistics and probability graph methods were common, yet the use and preference of these methods are debatable. In the past few decades, many articles were dedicated to usage and preference of fractal methods. Considerable group of researchers believe that these methods are more accurate and precise because of considering data geometry. They have presented many different case studies as examples and proofs for this idea. In comparison, lots of researchers insist on the simplicity and usability of classic methods. In the cases with low data volume and low complexity of dataset, they make an obvious assumption that the simplest method gives more accurate and more real responses. But the first group, based on the literature review and conducted studies, believe in the absolute preference of fractal methods.

The current study, without any orientation, argues about the use of both approaches: 1- traditional methods ($\mu+nS$ and probability graph) and 2- C-A fractal method. The studied elements are rare earths including La, Ce and Nd, which are usually correlated with each other because of their chemical similarity. They usually form with each other. It is notable that studied deposit has been enriched due to the secondary processes and the effect of metasomatic fluids. The abundant of actinolite is a confirmation for metasomatism.

In this study, 42 bulk lithology samples were collected from anomaly X of Se-Chahun iron ore deposit. They are from pit 1, 2 and 4 (supplementary part of pit 2 is known as pit 4, Figure 1). Samples were taken from ore body and metasomatic host rock. After preparing and analysis of the samples, three methods (i.e. classical statistics based on the mean and standard deviation, probability graph and C-A fractal model) were applied for anomaly-background separation of La, Ce and Nd.

2. GEOLOGICAL SETTINGS OF STUDY AREA

The Bafq district, extending from Bafq to Saghand, is part of the central Iranian micro plate which is now embedded within the Alpine-Himalayan orogenic system. This district is located in central Iran and is between 31°, 30' to 32°, 45' north latitude and 55°, 20' to 55°, 50' east longitude [44]. The central Iranian terrane is divided into three major crustal domains, from east to west: the Lut Block, Tabas Block and the Yazd Block [2]. The Tabas and Yazd blocks are separated by a nearly 600 km long, 80 km wide, arcuate and structurally complex belt (Kashmar-Kerman Tectonic Zone) composed of variably deformed and fault-bound supracrustal rocks [31]. Bafq mining district hosts several Kiruna-type iron oxide-apatite (IOA) deposits such as Se-Chahun, Choghart, Chahgaz, Esfordi, Mishdovan [4, 14, 46]. The Early Cambrian igneous rocks of the Bafq mining district have a bimodal nature. The chondrite-normalized REEs patterns display significant variation from LREEs to HREEs with no considerable Eu anomalies for basaltic rocks, and show obvious enrichment in the LREEs with important negative Eu anomalies for the rhyolitic domes [30]. The REEs enrichment is intensely associated with the formation of phosphate minerals in many IOA deposits. However, sometimes bastnasite and allanite are significant [28]. Edfelt [15] explained that there are few complications in the phosphate-REE relationship in some Kiruna districts. Hence, the relationship between REEs and phosphate minerals in such deposits should be more understood. In these deposits, apatites characteristically comprise 2000–6000 ppm REEs [17, 18]. Daliran [13] claimed that Bafq district apatites contain up to 1.75 wt. % REEs. Some researches present that post-depositional REE leaching could be occurred in apatite in which the inclusions of monazite and xenotime might be seen [5, 41, 43]. The U–Pb dating of monazite inclusions in apatite demonstrates that the REEs redistribution in apatite might be happened frequently throughout hydrothermal processes several million years after the formation of the IOA deposits [41].

The Se–Chahun deposit is composed of two major groups of ore bodies called the X and XI anomalies [26]. Anomaly X contains 11 Mt iron ore reserve with mainly rich magnetite ore [44]. Anomaly XI occurs 3 km northeast of anomaly X. Each anomaly consists of two or three smaller tabular to lens shaped ore bodies in association with other small bodies [5]. The mineralization is mainly hosted by metasomatized tuffs of andesite composition. Host rocks are known as metasomatites in this deposit [26]. The ore bodies map (anomaly X of Se-Chahun deposit), as well as the location of samples within the study area are shown in Figure 1.

The host rocks have a gradual boundary. Samples mainly include iron ores, low-grade ores (transition zone, consisting of plagioclase and actinolite) and metasomatitic rocks (mainly consists of actinolite and plagioclase). The host rocks are composed of metasomatized andesitic tuffs. Limestones and dolomites are observed in limited areas. Ore body is

comprised of high grade magnetite. The most important REE-bearing minerals in Se-Chahun deposit are apatite and monazite. The content of rare earth elements is directly related to the amount of apatite. The more the apatite, the more REE is. Monazites are very fine grained and just can be distinguished in SEM images.

3. GEOCHEMICAL DATASET

42 samples were taken from Se-Chahun iron ore deposit. The strategy of sampling was bulk lithology sampling with least number of samples (to consider the cost) which shows the most variances and the most features and reality of the deposit. They are about 1 to 1.5 kg weight and have been taken from ore body and metasomatic host rock. After preparation, samples were analyzed with Inductively Coupled Plasma Mass Spectrometry (ICP-MS). Concentrations of La, Ce, Nd, P and some statistical parameters of these elements and logarithmic value of them are shown in Table 1. La, Ce and Nd are the most concentrated elements among all REEs. Histograms of them are illustrated in Figure 2. Normal Q-Q plots of Ln (La), Ln (Ce) and Ln (Nd) show lognormal distribution of them (Figure 3). In addition, after taking logarithms, because of logarithmic distribution of data, histograms with normal curves were drawn once more (Figure 4).

4. METHODOLOGY

The first method which was applied in this study is the traditional method for separation of anomaly from background (i.e. using mean (μ) and standard deviation (S)). In this regard, values upper than $\mu+S$ and $\mu+2S$ were defined as anomaly and High anomaly, respectively. Another approach for dividing the populations (or anomaly background separation) is probability graph. In this method, cumulative frequency curve is plotted on a logarithmic graph and a change in the slope of the curve or point of inflection indicates the presence of more than one distribution [45]. For this purpose, cumulative frequencies of each element (in percent) were calculated in logarithmic distances and then, they were plotted on the logarithmic graphs. On the other hand, C-A fractal model was applied as the third approach. The C-A fractal [7, 8, 9] is one of the most widely used fractal models. The C-A model, originally developed by Cheng et al. [7], represents the first important step in fractal/multifractal modeling of geochemical data and has been “a fundamental technique for modeling of geochemical anomalies” [6, 25, 29]. The expression is given in Eq. (1).

$$A(\geq c) \propto c^{-\alpha} \quad (1)$$

In this model, the measure $A(\geq c)$ is the area enclosed by contours with values greater than or equal to c on a geochemical contour map. It can also be estimated using box-counting techniques, which involves counting the number of pixels with averaged concentration values greater than or equal to c on interpolated geochemical images. The exponent α may have different values for different ranges of c . If the geochemical data is composed of multiple populations (for example, a mineralization-related anomalous population and a background population), the distribution of the points on a log $A(\geq c)$ -log (c) plot fits more than one line segment. Each line segment is presumed to represent a different population characterized by a different value of the exponent α . The right-most breakpoint joining the line segments is generally taken as the threshold for separating anomaly from background [9, 24, 27, 29].

5. RESULTS AND DISCUSSION

Because of lognormal nature of dataset, which has been discussed in section 3, logarithmic values of the concentrations of La, Ce and Nd were used in method of classical statistics. Consequently, using $\mu+S$ and $\mu+2S$ as the thresholds, anomaly and high anomaly zones, were determined (Table 2). The average values of La, Ce and Nd as well as the number of samples for each zone are illustrated in Table 2. As it can be seen in Table 2, the threshold of $\mu+2S$ has separated just 2 samples for La and 1 sample for Ce and Nd, with highest concentrations. Therefore, it seems to be more reasonable to use $\mu+S$ as the threshold.

Cumulative probability graphs for La, Ce and Nd were plotted and showed in Figure 5. Intervals are logarithmic and the lower limit of each class was plotted. It is possible to identify the populations of the same samples by such graphs. However, in this study, the purpose is to determine the appropriate thresholds for anomaly-background separation. The thresholds for anomalies were found visually on these graphs. These points were determined with changes in the slopes of the curves at the ends. The thresholds are 90.1, 148.5 and 90.1 ppm for La, Ce and Nd, respectively. The averages of La, Ce and Nd in anomalous parts are 257.7, 500.5 and 247.5 ppm, respectively. By applying these thresholds, anomalies were determined. A summary of this method is illustrated in Table 3.

Distribution maps of La, Ce and Nd are shown in Figure 6. These maps were plotted based on the samples and interpolation using inverse distance method. Red color demonstrates the anomalous areas and highest concentrations and in contrast blue color represents the background areas with least concentrations. As it can be seen, the most concentrated area is located in south part in pit 4. Figure 7 shows the log-log plots of Concentration-Area for La, Ce and Nd with determined thresholds of anomaly zones. Moreover, Anomalies which have been resulted by fractal model and threshold value corresponding to each one, are illustrated in Table 4. The thresholds were determined in points where the

6. CONCLUSION

Whatever the variance is lower, the outputs of methods will be closer together. Nd has more similar results in the three methods because of its lower variance. The amount of variance in the study area is high. Therefore, for anomaly-background separation of REEs in this area, it is important to find an appropriate method. Results of probability graph have the best matches with geological and experimental information in comparison to traditional method of using $\mu+S$

slopes are changed from the ends of the curves. They are 106.4, 244.7 and 111.2 ppm for La, Ce and Nd, respectively. In addition, the averages of La, Ce and Nd in anomalous parts are 452.2, 798 and 295.2 ppm, respectively.

A comparison between all three methods can be seen with a quick look in Table 5. Finally, the validity of each of these methods is possible only by comparing the geological information. For that matter, the results were compared with geological surveys and field studies as well as experimental analysis of samples such as XDR and microscopic analysis. As a conclusion and summary of findings, 10 samples that were determined as the anomaly by all three methods, were collected in Table 6. It should be noted that all of these samples have anomalous condition and almost they are all of the anomalous samples. Geological studies show that REEs of Se-Chahun deposit are mainly in apatite and some amounts in monazite. These minerals were detected in 9 of these 10 samples (Table 6). Some apatites are depleted from REEs, as it has been discussed by Bonyadi et al. [5]. However, all of the 10 samples, more or less, have considerable amounts of La, Ce and Nd. Therefore, it can be concluded that all three methods, have shown the anomaly correctly. But, probability graph identified completely and fractal model identified samples with higher concentrations in comparison to others. In addition, anomaly and the changes in the slopes of the curves are more recognizable in probability graphs comparing with Concentration-Area plots. Results of Nd have the most similarity in the three methods. This element has the least variance.

The results showed that at least in cases such as this study, in which there are few number of data, more simple methods have the more appropriate responses. Though some researchers consider this a fact, lots of others use the articles of fractal methods as a basis to their studies, and insist on it. But this study showed that this hypothesis is not always correct. The probability graph provided more accurate answers, which are consistent with the geological evidences that are summarized in Table 6.

and $\mu+2S$ as well as C-A fractal model. According to results and simplicity of the method, probability graph is more applicable and better approach in comparison to others. Moreover, it concluded that in cases, which there are few number of data, more simple methods have the more appropriate responses.

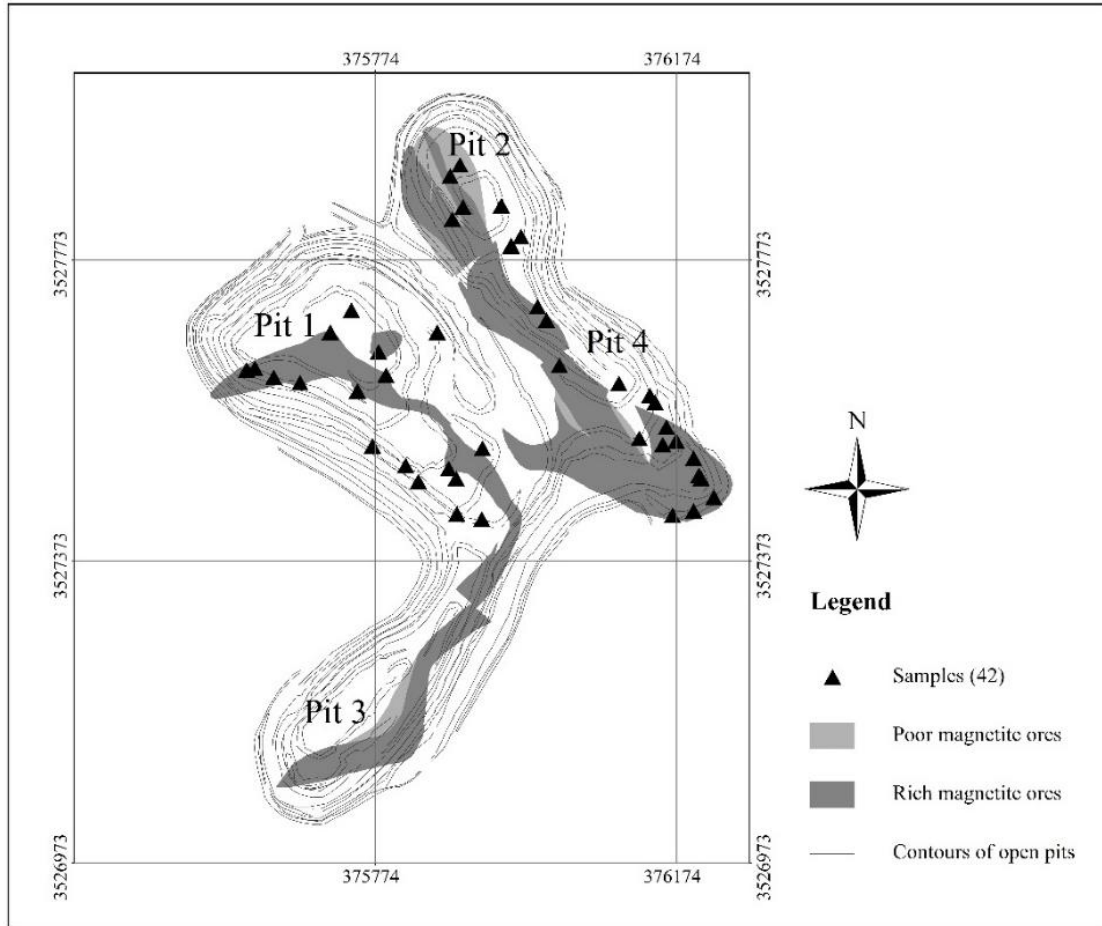


Figure 1 Ore bodies (anomaly X of Se-Chahun deposit), and sample locations. Contours of open pits are shown in the map and the open pits are numbered from 1 to 4 (supplementary part of pit 2 is known as pit 4) (modified after [26]).

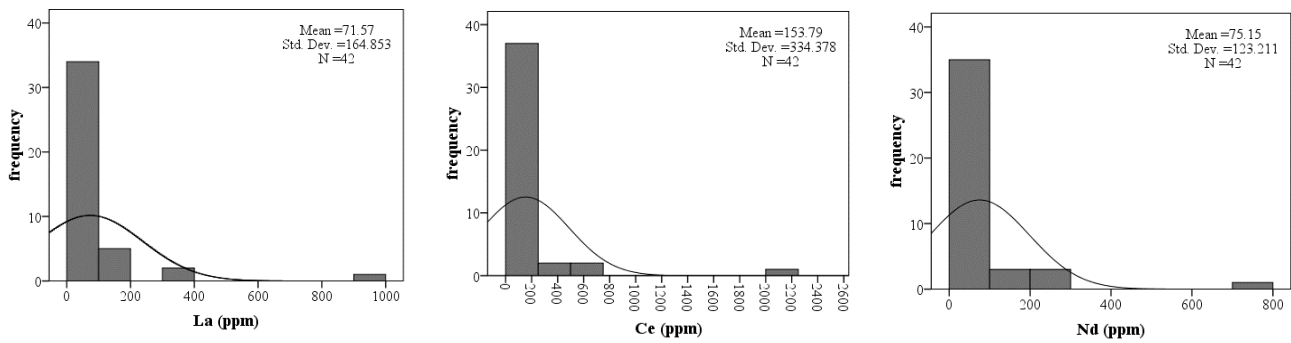


Figure 2 Histograms of La, Ce and Nd with distribution curves (42 samples).

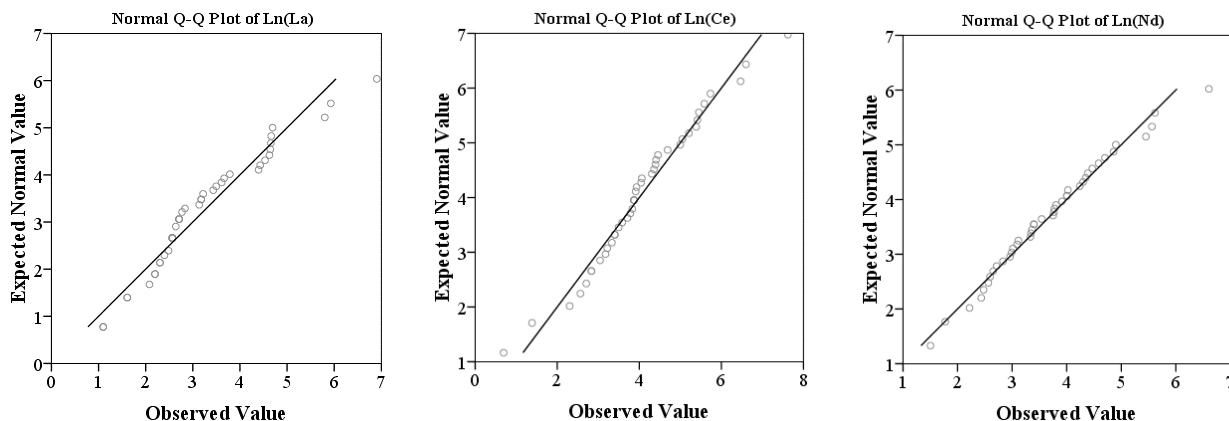


Figure 3 Normal Q-Q plots for logarithmic values of La, Ce and Nd. Plots show the lognormal distribution.

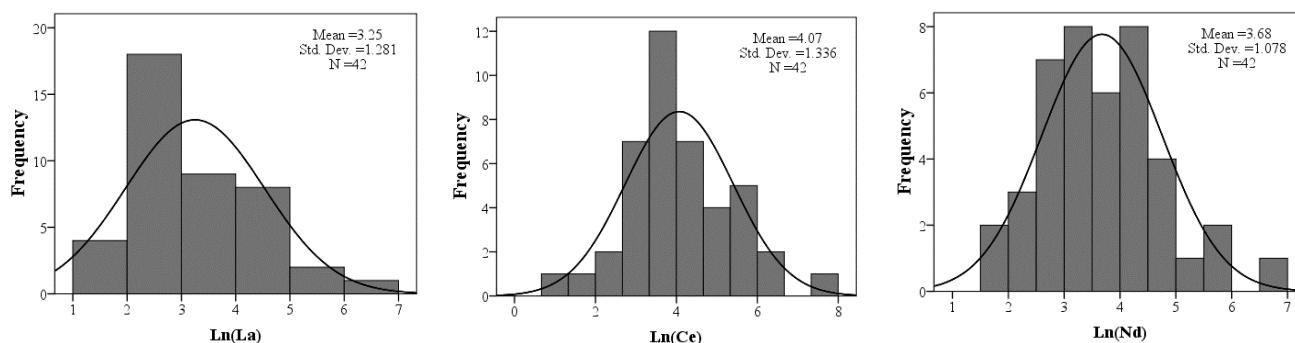


Figure 4 Histograms of La, Ce and Nd (logarithmic data) with distribution curves.

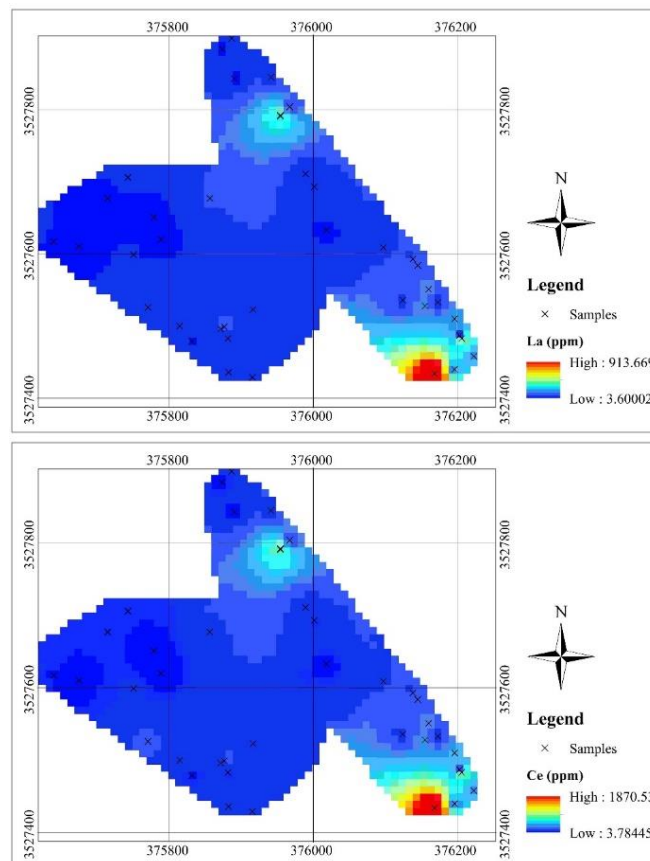
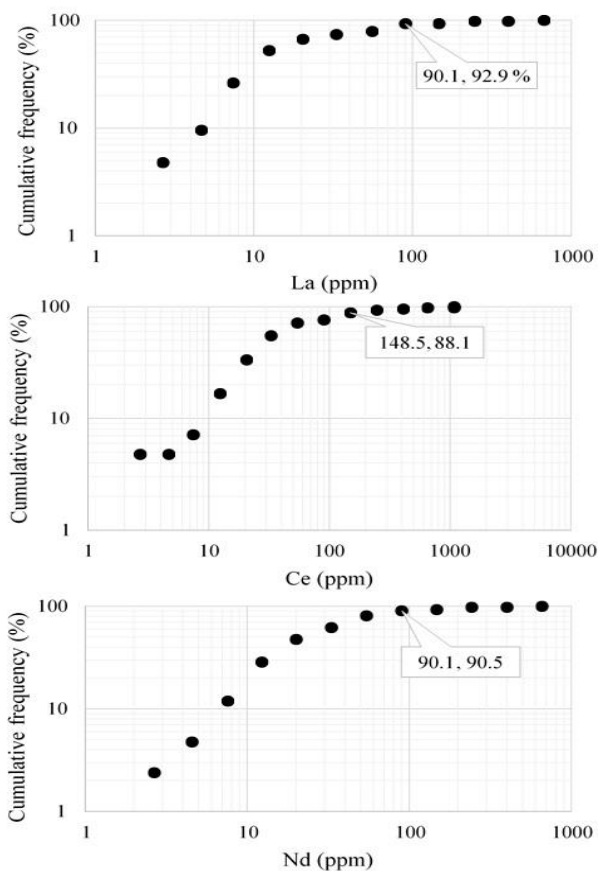


Figure 5 Cumulative probability graphs of La, Ce and Nd with thresholds of anomaly zones.

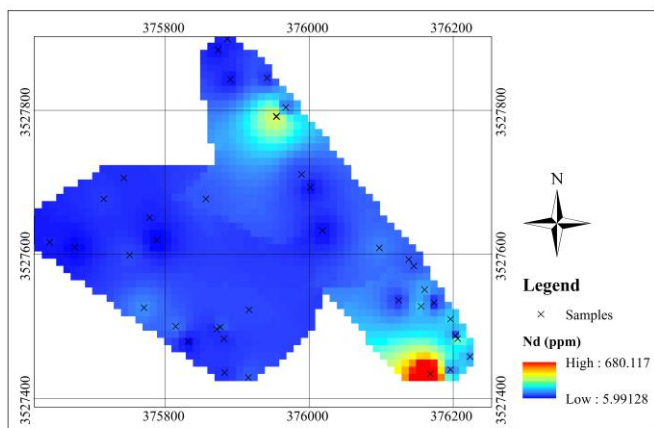


Figure 6 Distribution maps of La, Ce and Nd, based on the samples (Interpolation by inverse distance method).

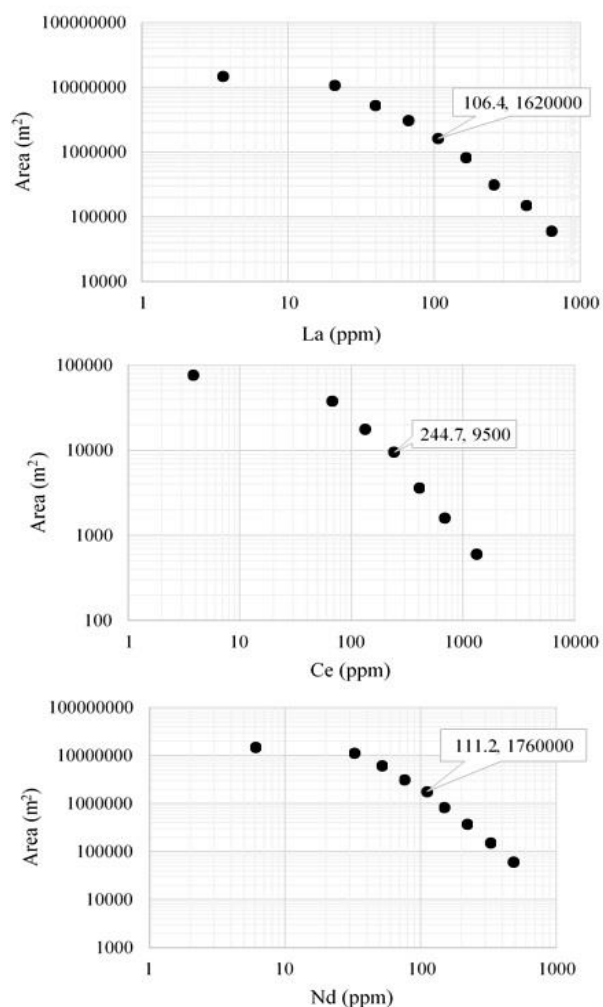


Figure 7 Concentration-Area plots of La, Ce and Nd with determined thresholds of anomaly zones.

Table 1 Assayed REEs and some statistical parameters.

Elements (ppm)	La	Ce	Nd	Ln(La)	Ln(Ce)	Ln(Nd)
Mean	72	154	75	3.25	4.07	3.68
Median	17	49	39	2.8	3.89	3.65
Variance	271	1118	151	1.64	1.78	1.16
Standard deviation	165	334	123	1.28	1.34	1.08
Minimum	3	2	5	1.1	0.69	1.5
Maximum	995	2037	740	6.9	7.62	6.61
Skewness	5	5	4	0.8	0.18	0.43
Kurtosis	25	26	21	0.575	0.91	0.28

Table 2 Results of classical statistics using $\mu+S$ and $\mu+2S$ as the thresholds for anomaly and high anomaly.

	Ln(La)	Ln(Ce)	Ln(Nd)
$\mu+S$	4.53	5.41	4.75
$\mu+2S$	5.81	6.74	5.83

Element	Range	Threshold	Mean (ppm)	Number of samples
La	Anomaly	92.9	257.7	9
	High anomaly	334.6	685	2
Ce	Anomaly	222.9	635.4	7
	High anomaly	847.9	2037	1
Nd	Anomaly	116	295.2	6
	High anomaly	341	739.5	1

Table 3 The resulted anomalies by probability graphs.

Element	Threshold	Mean (ppm)	Number of samples
La	90.1	257.7	9
Ce	145.5	500.5	10
Nd	90.1	247.5	8

Table 4 Anomalies which have been resulted by fractal model

Element	Threshold	Mean (ppm)	Number of samples
La	106.4	452.2	4
Ce	244.7	798	5
Nd	111.2	295.2	6

Table 5 Comparison between three methods.

Element	M+S			Probability graph			Fractal model		
	Threshold	Mean (ppm)	No.	Threshold	Mean (ppm)	No.	Threshold	Mean (ppm)	No.
La	92.9	257.7	9	90.1	257.7	9	106.4	452.2	4
Ce	222.9	635.4	7	145.5	500.5	10	244.7	798	5
Nd	116	295.2	6	90.1	247.5	8	111.2	295.2	6

Table 6 Concentration of La, Ce and Nd in all determined anomaly samples with detection of apatite and monazite by XRD and SEM methods (* marked concentrations are under the thresholds).

Sample code	La (ppm)	Ce (ppm)	Nd (ppm)	Apatite (XRD)	Apatite (SEM)	Monazite (SEM)
1-19	84*	156	77.3*	–	Not checked	Not checked
2-6	109	309	260.3	–	–	✓
2-9	375	734	275.3	✓	Not checked	Not checked
4-1	330	644	233	✓	–	✓
4-3	104	266	134.3	✓	✓	✓
4-5	995	2037	739.5	✓	✓	✓
4-6	93	183	69.4*	✓	✓	✓
4-7	106	225	98.1	✓	–	–
4-9	102	218	110.2	✓	✓	✓
4-10	105	233	128.9	✓	✓	✓

7. REFERENCES

- [1] Abd El Nabi, S.H. (2001). Evaluation of airborne gamma-ray spectrometric data for the Missikat uranium deposit, Eastern Desert, Egypt. *Applied Radiation and Isotopes*, 54, 497–507.
- [2] Alavi, M. (1991). Tectonic map of the Middle East (scale 1:5, 000, 000). Geological Survey of Iran.
- [3] Ander, E.L., Johnson, C.C., Cave, M.R. et al. (2013). Methodology for the determination of normal background concentrations of contaminants in English soil. *Science of the Total Environment*, 454–455, 604–618.
- [4] Barton, M.D. (2014). Iron oxide(-Cu-Au-REE-P-Ag-U-Co) systems. *Treatise on Geochemistry*, 13, 515-541.
- [5] Bonyadi, Z., Davidson, G.J. Mehrabi, B. et al. (2011). Significance of apatite REE depletion and monazite inclusions in the brecciated Se-Chahun iron oxide apatite deposit, Bafq district, Iran: insights from para-genesis and geochemistry. *Chemical Geology*, 281, 253–269.
- [6] Carranza, E.J.M. (2009). Geochemical anomaly and mineral prospectivity mapping in GIS. *Handbook of exploration and environmental geochemistry* (M. Hale, Editor), 11, 51–84.
- [7] Cheng, Q., Agterberg, F.P., Ballantyne, S.B. (1994). The separation of geochemical anomalies from background by fractal methods. *Journal of Geochemical Exploration*, 51, 109–130.
- [8] Cheng, Q., Agterberg, F., Bonham-Carter, G. (1996). A spatial analysis method for geochemical anomaly separation. *Journal of Geochemical Exploration*, 56, 183–195.
- [9] Cheng, Q., (1999). Spatial and scaling modelling for geochemical anomaly separation. *Journal of Geochemical Exploration*, 65, 175–194.
- [10] Cheng, Q., Xu, Y., Grunsky, E. (2000). Integrated spatial and spectrum method for geochemical anomaly separation. *Natural Resources Research*, 9, 43–51.
- [11] Cheng, Q. (2007). Mapping singularities with stream sediment geochemical data for prediction of undiscovered mineral deposits in Gejiu, Yunnan Province, China. *Ore Geology Reviews*, 32, 314–324.
- [12] Cheng, Q. (2008). Non-linear theory and power-law models for information integration and mineral resources quantitative assessments. *Mathematical Geosciences*, 40, 503–532.
- [13] Daliran, F. (2002). Kiruna-type iron oxide-apatite ores and apatites of the Bafq district, Iran, with an emphasis on the REE geochemistry of their apatites. *Hydrothermal iron oxide copper-gold & related deposits: a global perspective*, 2, 303–320.
- [14] Daliran F., Stosch H.G., Williams P.J., et al. (2010). Lower cambrian iron oxide-apatite-REE (U) deposits of the Bafq district, east-central Iran. *Exploring for iron oxide copper-gold deposits: Canada and global analogues*, Geological Association of Canada, Short Course Notes 20, 143–155.
- [15] Edfelt, A. (2007). The Tjarrojakka apatite-iron and Cu (-Au) deposits, northern Sweden: products of one ore

- forming event. Dissertation, Lulea University of Technology, Sweden.
- [16] Fleischer, M. (1969). The lanthanide elements in fluorite. *Indian Mineral*, 10, 36-39.
- [17] Frietsch, R. (1982). On the chemical composition of the ore breccia at Luossavaara, northern Sweden. *Mineralium Deposita*, 17, 239-243.
- [18] Frietsch, R., Perdahl, J.A. (1995). Rare earth elements in apatite and magnetite in Kiruna-type iron ores and some other iron ore types. *Ore Geology Reviews*, 9, 489-510.
- [19] Galuszka, A. and Migaszewski, Z.M. (2011). Geochemical background – an environmental perspective. *Mineralogia*, 42 (1), 7-17.
- [20] Li, C., Ma, T. and Shi, J. (2003). Application of a fractal method relating concentration and distances for separation of geochemical anomalies from background. *Journal of Geochemical Exploration*, 77, 167-175.
- [21] Li, Q. and Cheng, Q. (2004). Fractal singular-value (eigenvalue) decomposition method for geophysical and geochemical anomaly reconstruction. *Earth Science-Journal of China University of Geosciences*, 29, 109-118 (in Chinese with English abstract).
- [22] Mahvash Mohammadi, N., Hezarkhani, A., Shokouh Saljooghi, B. (2016). Separation of a geochemical anomaly from background by fractal and U-statistic methods, a case study: Khooni district, Central Iran. *Chemie der Erde*, 76, 491-499.
- [23] Mandelbrot, B.B., Passoja, D.E., Paullay, A.J. (1984). Fractal character of fracture surfaces of metals. *Nature*, 308, 721-722.
- [24] Meigoony, M.S., Afzal, P., Gholinejad, M. et al. (2014). Delineation of geochemical anomalies using factor analysis and multifractal modeling based on stream sediments data in Sarajeh 1: 100,000 sheet, Central Iran. *Arabian Journal of Geosciences*, 7, 5333-5343.
- [25] Mokhtari, Z., Boomeri, M., Bagheri, S. (2015). Application of multifractal modeling technique in systematic litho-geochemical survey to identify Au-Cu anomalies in the Siah-Jangal area, Southeastern of Iran. *Arabian Journal of Geosciences*, 8, 9517-9530.
- [26] National Iranian Steel Corporation (1975). Report on detailed exploration of Se-Chahun iron ore deposit in central Iran. Tehran, National Iranian Steel Corporation (NISCO).
- [27] Nazarpour, A., Omran, N.R., Paydar, G.R. et al. (2015). Application of classical statistics, logratio transformation and multifractal approaches to delineate geochemical anomalies in the Zarshuran gold district, NW Iran. *Chemie der Erde-Geochemistry*, 75, 117-132.
- [28] Oreskes, N., Einaudi, M.T. (1990). Origin of rare earth element-enriched hematite breccias at the Olympic dam Cu-U-Au-Ag deposit, Roxby Downs, South Australia. *Economic Geology*, 85, 1-28.
- [29] Pazand, K., Hezarkhani, A., Ataei, M. et al. (2011). Application of multifractal modeling technique in systematic geochemical stream sediment survey to identify copper anomalies: a case study from Ahar, Azarbaijan, Northwest Iran. *Chemie der Erde-Geochemistry*, 71, 397-402.
- [30] Rajabi, A., Canet, C., Rastad, E., et al. (2015). Basin evolution and stratigraphic correlation of sedimentary-exhalative Zn-Pb deposits of the early cambrian Zarigan-Chahmir basin, Central Iran. *Ore Geology Reviews*, 64, 328-353.
- [31] Ramezani, J., Tucker, R.D. (2003). The saghand region, Central Iran: U-Pb geochronology, petrogenesis and implications for gondwana tectonics. *American Journal of Science*, 303, 622-665.
- [32] Reimann, C., Filzmoser, P., Garrett, R.G. (2005). Background and threshold: critical comparison of methods of determination. *Science of the Total Environment*, 346, 1-16.
- [33] Risdianto, D., Kusnadi, D. (2010). The Application of a Probability Graph in Geothermal Exploration. *Proceedings World Geothermal Congress, Bali, Indonesia*, 25-29 April.
- [34] Sarparandeh, M. and Hezarkhani, A. (2016). Application of self-organizing map for exploration of REEs' deposition. *Open Journal of Geology*, 6, 571-582.
- [35] Sarparandeh, M. and Hezarkhani, A. (2016). Studying distribution of rare earth elements by classifiers, Se-Chahun iron ore, Central Iran. *Acta Geochimica*, 35, 140, 1-8.
- [36] Schuler, D., Buchert, M., Liu, R., et al. (2011). Study on rare earths and their recycling, Final report for the Greens/EFA group in the european parliament, The Greens/European free alliance, 42-59.
- [37] Shekarian, Y. (2014). Geochemical investigations on REEs in N-NE Choghart iron deposit and their economic evaluations. Dissertation, Amirkabir University of Technology (Tehran Polytechnic), Tehran.
- [38] Siegel, F. R. (2002). *Environmental geochemistry of potentially toxic elements*. Springer-Verlag, Berlin, 80-81
- [39] Simandl, G. (2014). Geology and market-dependent significance of rare earth element resources. *Mineralium Deposita*, 49, 889-904.
- [40] Sinclair A.J. (1974). Selection of threshold values in geochemical data using probability graphs. *Journal of Geochemical Exploration*, 3, 129 - 149.
- [41] Stosch, H.G., Romer, R.L., Daliran, F., et al. (2011). Uranium-lead ages of apatite from iron oxide ores of the Bafq district, east-central Iran. *Mineralium Deposita*, 46, 9-21.
- [42] Tennant C.B., White M.L. (1959). Study of the distribution of some geochemical data. *Economic Geology*, 54, 1281- 1290.
- [43] Torab, F., Lehmann, B. (2007). Magnetite-apatite deposits of the Bafq district, central Iran: apatite geochemistry and monazite geochronology. *Mineralogical Magazine*, 71, 347-363.
- [44] Torab, F. (2008). Geochemistry and metallogeny of magnetite apatite deposits of the Bafq mining district, Central Iran. Dissertation, Clausthal University of Technology, Germany.

[45] Williams, X. K. (1967). Statistics in the interpretation of geochemical data. *New Zealand Journal of Geology and Geophysics*, 10 (3), 771–797.

[46] Zaremotlagh, S., Hezarkhani, A. (2016). A geochemical modeling to predict the different concentrations of REE

and their hidden patterns using several supervised learning methods: Choghart iron deposit, bafq, Iran. *Journal of Geochemical Exploration*, 165, 35–48.

f

DESIGN OF A GRID CONNECTED SOLAR SYSTEM FOR YOLA NORTH AND SOUTH, ADAMAWA STATE

Engr. Alfred, Ba'amani Baams
Department of Electrical & Electronics Engineering,
Modibbo Adama University of Technology, Yola, Nigeria

Engr. Dr. Iliya Tizhe Thuku
Department of Electrical & Electronics Engineering,
Modibbo Adama University of Technology, Yola, Nigeria

Engr. Simon Samuel
Department of Electrical & Electronics Engineering,
Modibbo Adama University of Technology, Yola, Nigeria.

ABSTRACT: In this research work, a grid connected solar photovoltaic (PV)-battery energy storage system (PV/BESS) was designed to improve the power supply of Yola north and south. The solar photovoltaic panel model adopted is 100W monocrystalline photovoltaic panel, and the average solar radiation of the study area is 654.40W/m². The system consists of modeled PV Array, Boost converter model, three-phase power inverter model, step-up power transformer and modeled Phase locked loop. The designed solar photovoltaic model generated 3.40MW of electric power via the step-up transformer, which was integrated into the utility grid of the study area. The output signal of the solar PV array was optimized using boost converter. The inverter inverted the output of the PV array to AC signal, which is connected to step-up power transformer to step-up the three-phase AC voltages to the grid voltages level. PLL was designed for proper synchronization of the solar PV model with the grid without harmonic distortions. The designed solar PV array model was able to supplement the deficit power of 3.40MW to the grid of the study area.

Keywords: Photovoltaic System, Boost Converter, 3-phase power Inverter, PLL, step-up power transformer and grid source.

1. INTRODUCTION

This paper focuses on the design and simulation of a grid connected PV system that will augment the shortfall in power supply in Yola North and South as well as to overcome the problem of load shedding. The increase of the study area energy demand, due to modern industrial development, population growth and global warming, encourages investments in renewable energy. Hence, alternative energy in particular solar energy serves as solution to the inadequate power supply of the study area. However, battery energy storage system (BESS) is connected to the systems for use at night and during cloudy days. The solar power system used photovoltaic (PV) cell to convert solar radiation to electricity [20]. The PV cell produces only a small amount of current and voltage. So, in order to meet a large load demand, the photovoltaic cell has to be connected into modules and the modules connected into arrays [1]. The grid connected solar

photovoltaic system is designed in cognizance of the effect of environmental weather conditions. The PV array model output signal connected to the utility network is converted to AC signals compatible with the grid AC voltage. This paper discusses the detailed modeling and simulation of the complete grid-connected PV array system. The solar PV array model is connected to the utility grid by a DC-DC boost converter that boosted the PV array model output voltage, and DC-AC inverter inverted the DC output voltage of the PV array into the three-phase AC voltages. The PI control circuit of the DC-converter was used to maintain constant DC input of the inverter. The model of the entire system is simulated in Matlab/Simulink environment. The block diagram of the design is shown in Figure 1. It consists of photovoltaic Array, DC-DC boost converter, BESS, 3-phase Inverter, 3-phase PLL, 3- phase step-up transformer, 3-phase load and 3-phase utility grid source.

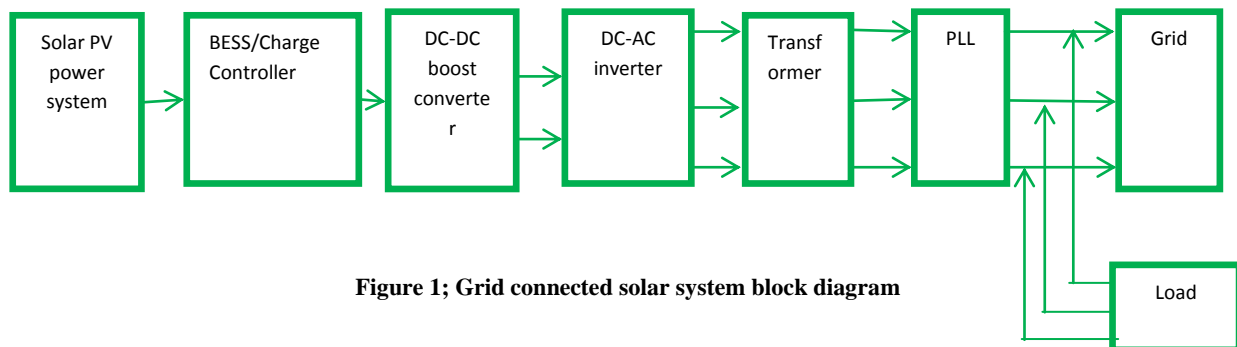


Figure 1; Grid connected solar system block diagram

2. System design

This section deals with the modeling and simulation of the complete designed of grid connected solar PV array that formed the sub-systems. The following steps were considered for the actualization of the design; Data collected on load demand and weather conditions of the study area from YEDC, TCN and NAMA Yola, design and simulation of solar PV array system in Matlab/Simulink programs and synchronization in order to control the disturbances on the lines.

3. Solar array sizing

The power of one module is not enough to meet the power requirement of the study area. Some of the modules in a PV array are connected in series to obtain the desired voltage while some are connected in parallel to produce current that made up the required power [9]. However, diodes are connected alongside the photovoltaic cells to avoid reverse currents, in case of partial or total shading [13]. The total number of photovoltaic (PV) modules required for the grid connected solar system for the study area is calculated using the equations given as follows;

$$E_r = \frac{\text{Daily average consumption demand}}{\text{product of components efficiency}}$$

$$E_r = \frac{E}{\eta_{\text{overall}}} \quad (1)$$

[6]

Where;

E_r = Require energy

E = Daily energy or demand in Watt-hours

η = Component efficiency

The peak power (P_p) is equal to the required energy (E_r) divided by the average sun hours (T_{\min}) per day for a particular geographical location [2]. The equation 2 computes the P_p .

$$P_p = \frac{\text{Daily Energy requirement}}{\text{minimum sun peak hours per day}}$$

$$P_p = \frac{E_r}{T_{\min}} \quad (2)$$

Where;

E_r = Require energy

P_p = peak power

T_{\min} = period

The total direct current (I_{dc} measure in Amp) of the photovoltaic module is given by equation 3

$$I_{dc} = \frac{\text{peak power}}{\text{system DC Voltage}} = \frac{P_p}{V_{dc}} \quad (3)$$

Where;

I_{dc} = total dc current

P_p = Peak power

V_{dc} = DC-voltage

The mathematical expression of modules connected in series (N_s) and parallel (N_p) for the production of the current and

voltage obtain the power demand of the study area are presented in equations 4 and 5.

$$N_s = \frac{\text{system DC Voltage}}{\text{One module Rated Voltage}} = \frac{V_{dc}}{V_r} \quad (4)$$

$$N_p = \frac{\text{Whole Module current}}{\text{Rated current of one module}} = \frac{I_{dc}}{I_r} \quad (5)$$

[16]

Where;

N_s = Number of modules in series

N_p = Number of modules in parallel

V_r = Rated voltage of each module

I_r = Rated current of a single module

I_{dc} = Whole DC current

The total number of photovoltaic modules needed for the power requirement of the study area is calculated using equation 6.

$$N_m = N_s \times N_p \quad (6)$$

P_p of 3.40MW and V_{dc} of the system 4000V

The total dc current (I_{dc}) is calculated using the equation 3 to give;

$$I_{dc} = \frac{\text{peak power}}{\text{System DC Voltage}} = \frac{P_p}{V_{dc}}$$

$$I_{dc} = \frac{3.40\text{MW}}{4000\text{V}} = 850\text{A}$$

To determine the number of PV modules in series (N_s) the equation 4 is used;

$$N_s = \frac{\text{system DC Voltage}}{\text{One module Rated Voltage}}$$

$$N_s = \frac{V_{dc}}{V_r} = \frac{4000\text{V}}{17.40\text{V}} = 230 \text{ modules.}$$

Calculation of number of modules in parallel using equation 5 is shown as Follow;

$$N_p = \frac{\text{Whole Module current}}{\text{Rated current of one module}}$$

$$N_p = \frac{I_{dc}}{I_r} = \frac{850\text{A}}{5.75\text{A}} = 148 \text{ modules.}$$

The total number of modules required for the complete design of the system is calculated using equation 6 as follows:-

$$N_m = N_s \times N_p = 230 * 148 = 34,040 \text{ Modules}$$

4. PV System Modeling

Photovoltaic module has standard mathematical modeling equations [12]. These equations are used in modeling and

simulation of the system using matlab-simulink program. The characteristic equations of solar photovoltaic cell are applied in the formation of the photovoltaic arrays. These characteristic equations of the PV cell are given as;

i. Reverse saturation current (I_{rr}) equation;

$$I_{rr} = \frac{I_{scr}}{\exp\left(\frac{QV_{oc}}{N_s k A T_{rk}} - 1\right)} \quad (7)$$

Where;

I_{scr} = Short Circuit Current = 6.32A,
 Q = Electron charge = 1.6×10^{-19} C,
 V_{oc} = Open circuit v
 Voltage = 21.60V
 N_s = Number of modules in series = 230
 k = Boltzmann's constant = 1.3805×10^{-23} J/K,
 A = Ideality factor of diode = 1.3,
 T_{rk} = Reference temperature = 298.15K

ii. Band gap of solar cell (E_G) equation;

$$E_G = E_{G(0)} - \frac{\alpha(T_{op})^2}{T_{op} + \beta} \quad (8)$$

[17]

Where;

α = alpha = 0.473
 $E_{G(0)}$ = 1.166
 β = beta = 636
 T_{op} = operating temperature = 305.7K

iii. Reversed saturation current at T_{op} (I_{rs});

$$I_{rs} = I_{rr} \left[\frac{T_{op}}{T_{rk}} \right] * \text{Exp} \left(\frac{Q E_G}{K A} \left[\frac{1}{T_{op}} - \frac{1}{T_{rk}} \right] \right) \quad (9)$$

Where;

I_{rr} = Reverse saturation current
 T_{op} = operating temperature = 305.7K
 T_{rk} = Reference temperature = 298.15K
 Q = Electron charge = 1.6×10^{-19} C
 E_G = Band gap energy
 k = Boltzmann's constant = 1.3805×10^{-23} J/K
 A = Ideality factor of diode = 1.3

iv. Photo-current (I_{ph}) equation;

$$I_{ph} = [I_{scr} + K_i(T_{op} - T_{rk})] * S \quad (10)$$

Where;

I_{scr} = Short circuit current = 6.32A.
 K_i = short-circuit current of cell at = 0.00023
 T_{op} = operating temperature = 305.7K
 T_{rk} = Reference temperature = 298.15K
 S = solar irradiation (W/m²) of the study area with average value 654.40 W/m²

v. Thermal Voltage (V_{th}) equation;

$$V_{th} = \frac{Q}{k T_{op}} \quad (11)$$

[4]

Where;

Q = Electron charge = 1.6×10^{-19} C

k = Boltzmann's constant = 1.3805×10^{-23} J/K
 T_{op} = operating temperature = 305.7K

vi. Current source output (I) equation;

$$I = N_p I_{ph} - N_p I_{rs} \left[\exp\left(\frac{Q}{A k T} * \frac{V_{th}}{N_s}\right) - 1 \right] \quad (12)$$

Where;

N_p = Number of modules in parallel = 148
 I_{ph} = Photo-current
 I_{rs} = Reversed saturation current at T_{op}
 Q = Electron charge = 1.6×10^{-19} C
 k = Boltzmann's constant = 1.3805×10^{-23} J/K
 A = Ideality factor of diode = 1.3
 V_{th} = Thermal Voltage
 N_s = No. of modules in series = 230
 [14]

The mathematical equations of these components were modeled individually and networked together to determine the functionality of the PV array. Hence, these equations are important for the design of the PV array [5], because it determine the desired output of the system. The first step in photovoltaic system modeling is to know the PV array size, determined using equation 6.

5. Modeled solar PV array system.

The modeling and simulation of the components of the photovoltaic system formed the masked subsystem of the PV array as shown in Figure 2. The subsystem of the PV array was simulated on a matlab-simulink environment. The result of the simulated solar PV array masked subsystem was satisfactory, and it serves as an input to the boost converter.

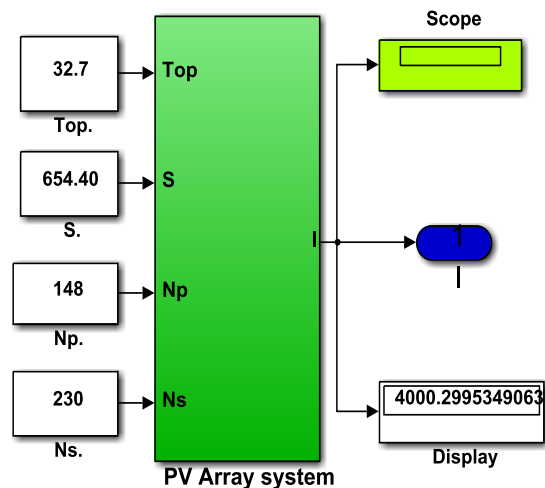
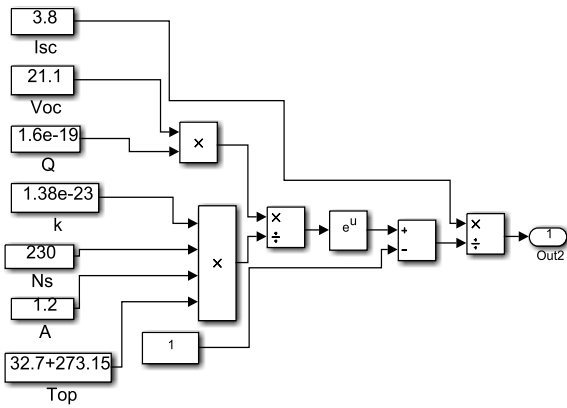


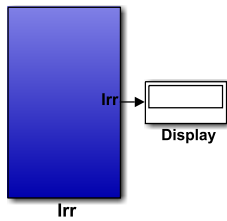
Figure 2; Modeled Photovoltaic (PV) array system

The internal structure of the masked subsystem of PV array of figure 2 such as figure 3, 4, 5, 6, 7 and 8 are given as follows;

5.1; Reverse saturation current (I_{rr}) model



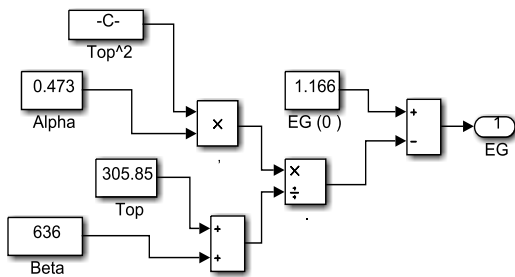
(a) I_{rr} simulink blocks.



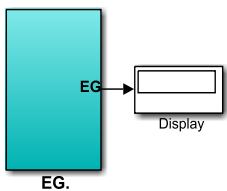
(b) I_{rr} subsystem

Figure 3; (a) Reversed saturation current (I_{rr}) Simulink Block and (b) I_{rr} simulink block converted to I_{rr} subsystem

5.2. Band gap of the solar cell (EG) model



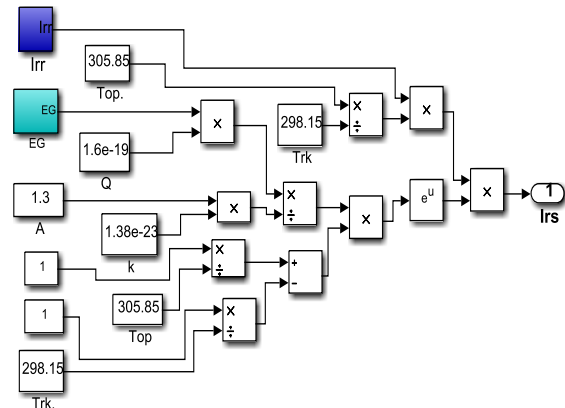
(a) EG simulink blocks.



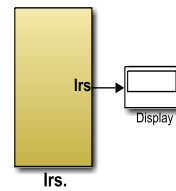
(b) EG subsystem

Figure 4; (a) Band gap of the solar cell (EG) Simulink block and (b) EG Simulink block converted to EG subsystem

5.3; Reversed saturation current at T_{op} (I_{rs}) model



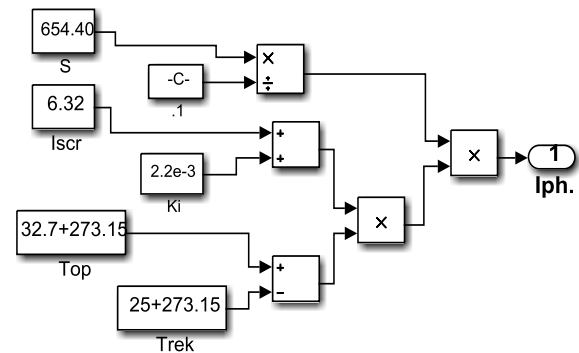
(a) I_{rs} simulink blocks.



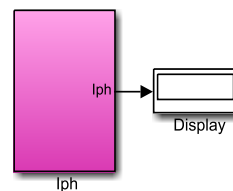
(b) I_{rs} subsystem

Figure 5; (a) Reversed saturation current at T_{OP} (I_{rs}) simulink block and (b) I_{rs} simulink block converted to subsystem

5.4; Photo-current (I_{ph}) model



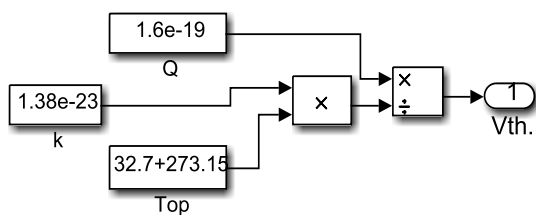
(a) I_{ph} simulink blocks.



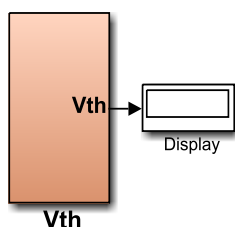
(b) I_{ph} subsystem

Figure 6; (a) Photovoltaic Current (I_{ph}) Simulink Block and (b) I_{ph} Simulink Block converted to subsystem

5.5; Thermal voltage (V) model



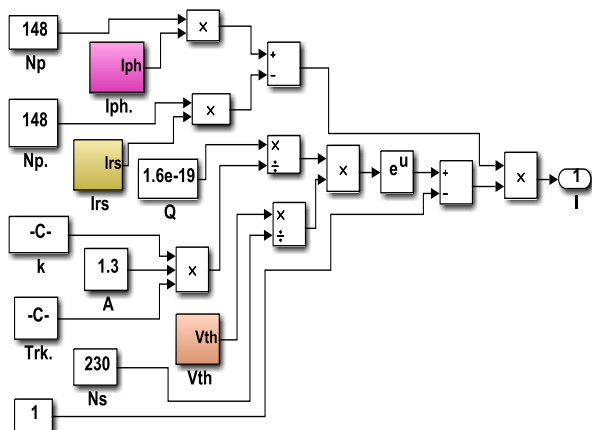
(a) Vth simulink blocks.



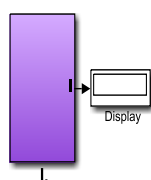
(b) Vth subsystem

Figure 7; (a) Thermal Voltage (V) Simulink Block and (b) V Simulink Block converted to subsystem.

5.6; Current source output (I) model



(a) I simulink blocks.



(b) I subsystem

Figure 8; (a) Current source output (I) simulink block and (b) I simulink block converted to subsystem.

7; Design and modeling of the Boost Converter

The boost converter is a system designed to convert low input signal (DC voltage) to high output signal (DC voltage). The unregulated input DC signal is filtered and then boosted to regulated output DC signal [7]. Here, the input DC source of the converter is PV output signal (DC voltage), which is boosted to a desired output of the converter. The design of boost converter is important, because it will help in controlling both the current (CRF) and voltage ripples (VEF). CRF was selected as 10% and VRF was also selected as 5%, in line with International Electro-technical Commission (IEC) harmonized standard which is bounded within the range 0-30% [12]. Where Switching Frequency (f_s)=100KHz, $\Delta I_o/I_o = 10\%$ and $\Delta V_o/V_o = 5\%$ are values for CRF and VRF used in the design to produce output with minimal ripples. The capacitor, inductor and the duty cycle are calculated using the given parameters of Input voltage (V_g) and output voltage (V_o) of the system converter where input and output voltage is 4000V and 7400V.
 $V_g = 4000V$,
 $V_o = 7400V$
 $I_o = 275A$

Calculation of the duty cycle (D):-

$$\begin{aligned} V_o/V_g &= 1/((1 - D)) \\ 1/((1 - D)) &= V_o/V_g \\ 1/((1 - D)) &= 7262/4000 = 0.449 \\ D &= 0.449 \quad (\text{duty cycle } D) \end{aligned}$$

Inductor (L) calculation:-

$$\begin{aligned} \Delta I &= (0.1 * 275) A = 27.5A \\ L &= \frac{DV_g}{f_s(\Delta I_L)} = \frac{(4000 * 0.449)}{(275 * 100 * 10^3)} = \frac{1796}{27500000} \\ L &= 0.0000653H = 0.065mH \\ R_o &= V_o/I_o = 7262/275 = 26.41 = 26.41\Omega \end{aligned}$$

Calculation of the Capacitor (C) as follows:-

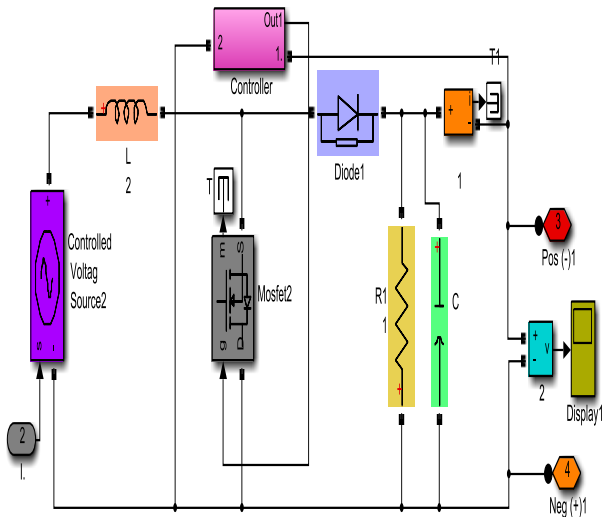
$$\frac{\Delta V_o}{V_o} = \frac{DT_s}{CR_o} \quad \text{where } C = \frac{D}{R_o f} * \frac{1}{\frac{\Delta V_o}{V_o}}$$

Therefore,

$$C = \frac{0.449}{26.41 * 100 * 10^3 * 0.05}$$

$$C = 3.4\mu F$$

The boost converter of figure 9 was modeled and simulated on Matlab-Simulink environment, which then boosted the input DC voltage to 7400V. However, the pulse width modulation controller and its duty cycle were used to turn and stabilize the converter output. Hence, figures 10 shows the PV array connected to boost converter model



(b) DC-DC boost converter Simulink block

Figure 9; Boost converter simulink block.

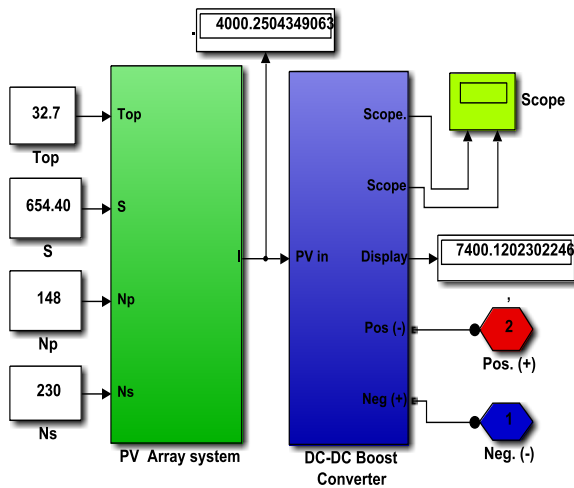


Figure 10; The interfaced of the PV array and boost converter model

8; Design of Battery energy storage system (BESS)

The battery storage system is the most efficient method of storing generated energy from solar PV system for use at night, cloudy, rainy and dusty days [18]. The BESS also maintaining power stability between the PV system and the utility grid [15]. In sizing the battery bank estimated energy storage is first determined [3]. The type of battery used is deep-cycle lead acid. The capacity of the entire battery bank is computed in ampere-hours, Electrical characteristics of the battery are given as; Number of Days of Autonomy (D_{aut}) = 3
Where

E_{est} = Estimated Energy Storage

E_{safe} (Wh) = Safe Energy Storage

C_{tb} (Ah) = Total Capacity of Battery Bank

N_{tb} = Total Number of Batteries in Bank

N_{sb} = Number of Batteries in Series

N_{pb} = Number of Batteries in Parallel

C_b = 250 Ah,

V_b = 12 V,

D_{disch} = 80%

$$E_{est} = E_d * D_{aut} \quad (13)$$

$$E_{safe} = \frac{E_{est}}{D_{disch}} \quad (14)$$

$$C_{tb} = \frac{E_{safe}}{V_b} \quad (15)$$

$$N_{tb} = \frac{C_{tb}}{C_b} \quad (16)$$

$$N_{sb} = \frac{V_{dc}}{V_b} \quad (17)$$

$$N_{pb} = \frac{N_b}{N_{sb}} \quad (18)$$

[10]

$$E_{est} = E_d * D_{aut} = 3400000 * 3 = 10200Kwh$$

$$E_{safe} = \frac{E_{est}}{D_{disch}} = \frac{10200000}{80\%} = 12750Kwh$$

$$C_{tb} = \frac{E_{safe}}{V_b} = \frac{12750000}{12} = 1062.5KAh$$

$$N_{tb} = \frac{C_{tb}}{C_b} = \frac{1062500}{250} = 4250 Batteries$$

(Total Batteries required = 4250)

$$N_{sb} = \frac{V_{dc}}{V_b} = \frac{4000}{12} = 333.3$$

(Number of Batteries in Series = 333.3)

$$N_{pb} = \frac{N_b}{N_{sb}} = \frac{4250}{333.3} = 12.8$$

(Number of Batteries in parallel = 12.8)

9; Charge controller (CC) design

A battery charge controller (BCC) is a device that controls the power flow within the system and regulates the system voltage to a specified range. Its purpose is to keep batteries properly fed and safe for the long term [11]. The system also block reverse current and control battery overcharge [18]. The design of a suitable CC starts by computing the required total current that the controller should withstand. The properties of the selected CC are as follows:

V_{cc} = 24,

I_{cc} = 60 A (dc),

Safety Factor (F_{safe}) = 1.25

The numbers of desired CC are calculated as follows;

N_{ccn} = Number of Charge Controllers

I_{rcc} (A) = Required CC Current

N_{pm} = Number of modules in parallel = 148

$I_{sc}M$ = Short circuit current of the selected module = 6.32A

N_{cc} = Number of CC

$$I_{rcc} = I_{sc}M * N_{pm} * F_{safe} \quad (19)$$

$$N_{cc} = \frac{I_{rcc}}{I_{cc}} \quad (20)$$

$$I_{rcc} = I_{sc}M * N_{pm} * F_{safe} = 6.32 * 148 * 1.25$$

$$I_{rcc} = 1169.2A$$

$$N_{cc} = \frac{I_{rcc}}{I_{cc}} = \frac{1169.2}{60} = 19.49 = 20$$

Number of Charge Controllers required = 20

10; Power AC Inverter design

All power generating plants that generate DC power normally need inverters to convert the power generated to AC power for use by AC rated appliances [11]. The subsystem of PV system-inverter shown in figure 11 is a complete block diagram of interfaced PV array model, DC converter and AC inverter model. The 3-phase AC output signals of the PV system-inverter model are the signals injected into the grid. The output of this model is a 3-phase sinusoidal signals module serves as an input to 3-phase step-up transformer to be connected to the grid system.

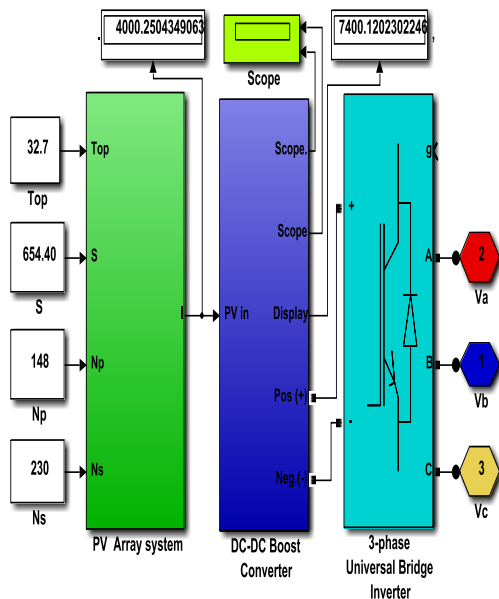


Figure 11; The block diagram of complete interfaced PV system with Booster and inverter.

11; Phase locked loop (PLL) modeling

The PLL is designed to control the phase difference and other harmonic distortion. The phase of generated signals of solar system is automatically adjusted to match the phase of an input signals of the grid. Figure 12 is the PLL Simulink block and as well an internal structure of figure 13. The model was simulated using Matlab/Simulink software.

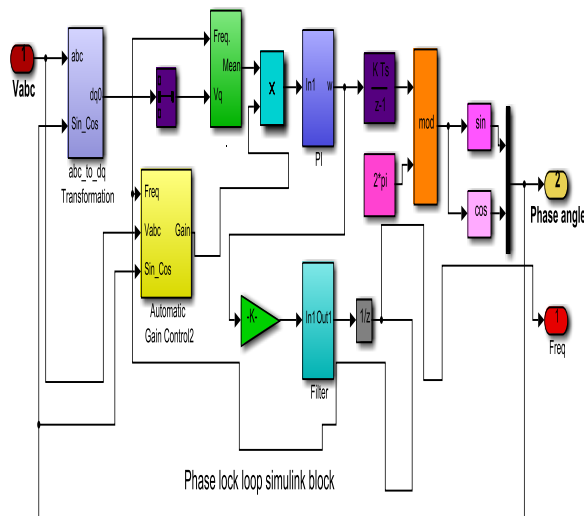


Figure 12; PLL Simulink block

The three blocks subsystem of PLL shown in figure 13 consists of the followings; phase detector (PD), loop filter (LF) and voltage controlled oscillator VCO. The PD is a comparator, which compares the input signals and the feedback signals. The output signal generated by the PD is proportional to the phase difference between the input signals and the signals generated by the internal oscillator called VCO. The output of the PD is an input to the LF. The LF is characterized with low pass filtering to attenuate high-frequency AC components from the PD output and provide DC controlled signal to VCO which acts as an integrator. The VCO generates at its output a periodic AC voltage signal provided by the LF [19].

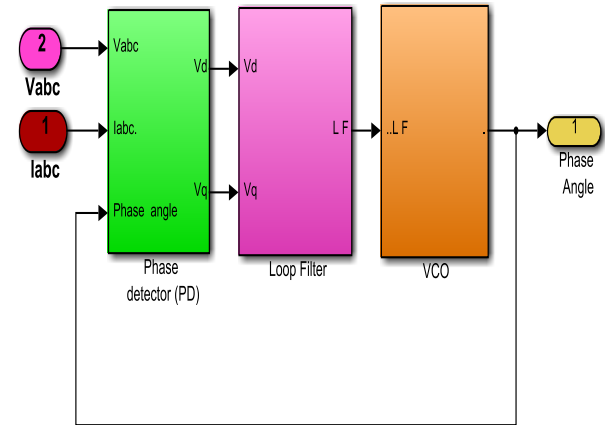


Figure 13; Subsystems of the PLL

The complete sub-system of the PLL is shown in Figure 14 which formed by masking the three blocks subsystem of PLL of figure 13.



Figure 14; Subsystem of the phase locked loop (PLL)

12; The complete modeled grid-connected solar system

The model is a network of the major subsystems which comprises of the following; PV array model that saves as a DC voltage source, DC- DC boost converter model, power AC inverter model, PLL model, step up transformer, protective and measuring devices, grid source (AC), and three-phase Load. The modeling and simulation were done on individual subsystems. The PV array model was simulated, which generated 4000V DC voltage as the main DC source to the boost converter. The generated 4000V was then optimized by the converter to 7400V DC voltage. The 7400V output DC voltage of the converter model is converted to 3-phase AC voltages (V_{abc}) by the power inverter. However, the 3-phase output AC voltage (V_{abc}) of the inverter is connected to 3-phase step up transformer, which synchronized with the utility grid voltage of 33KV.

13; The modeled complete photovoltaic grid connected without phase locked loop (PLL).

The model of figure 15 was simulated without the PLL. The result obtained from the simulated grid connected solar PV

array model without PLL was not quite clear as displayed by the waveforms. Based on observation, the system output is distorted by flickers. Therefore, it clearly shows that, both the solar PV array system and the utility grid are not having same characteristics.

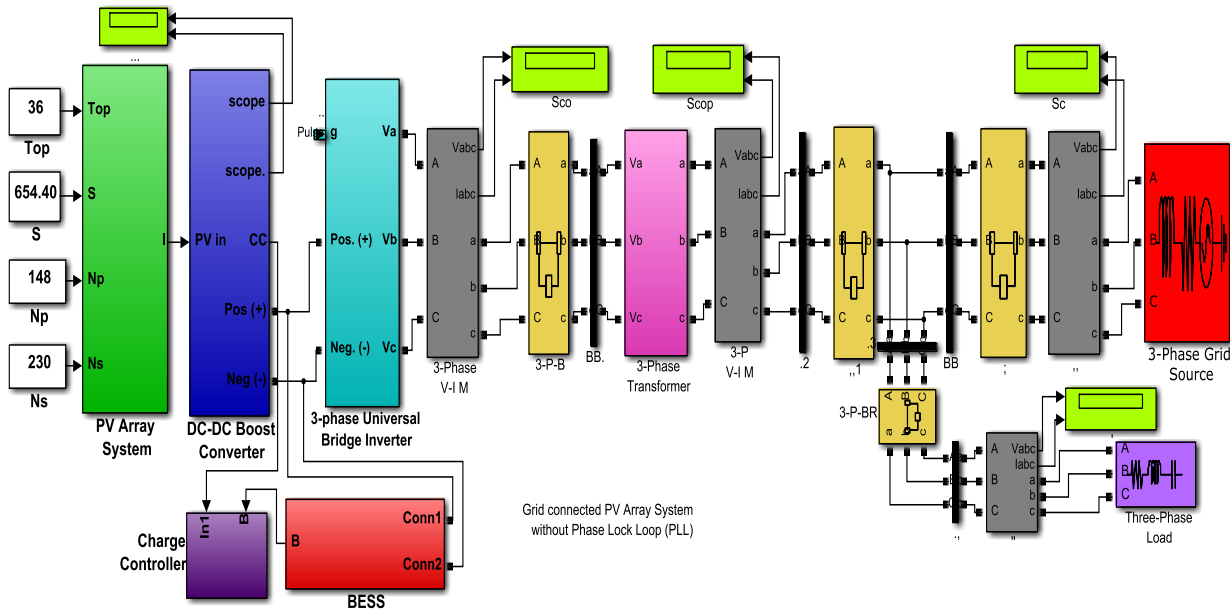


Figure 15; Simulink model of complete PV grid connected without PLL system

14; The modeled grid connected PV system with PLL

The grid-connected PV array model with PLL is shown in figure 16. Here, PLL was connected to figure 16 Model because of the distorted output of figure 15 model. The device was used to clear flickers on the lines such as phase difference, harmonics. So, synchronizing the solar PV array

system with the utility grid using PLL has given a better result. The results obtained from the simulated figure 15 model shows that the model output AC voltage is 33KV with the same frequency, amplitude and phase angle. The result obtained indicated that the grid-connected solar PV system with battery energy storage system have succeeded in tackling the problem of power supply in the study area.

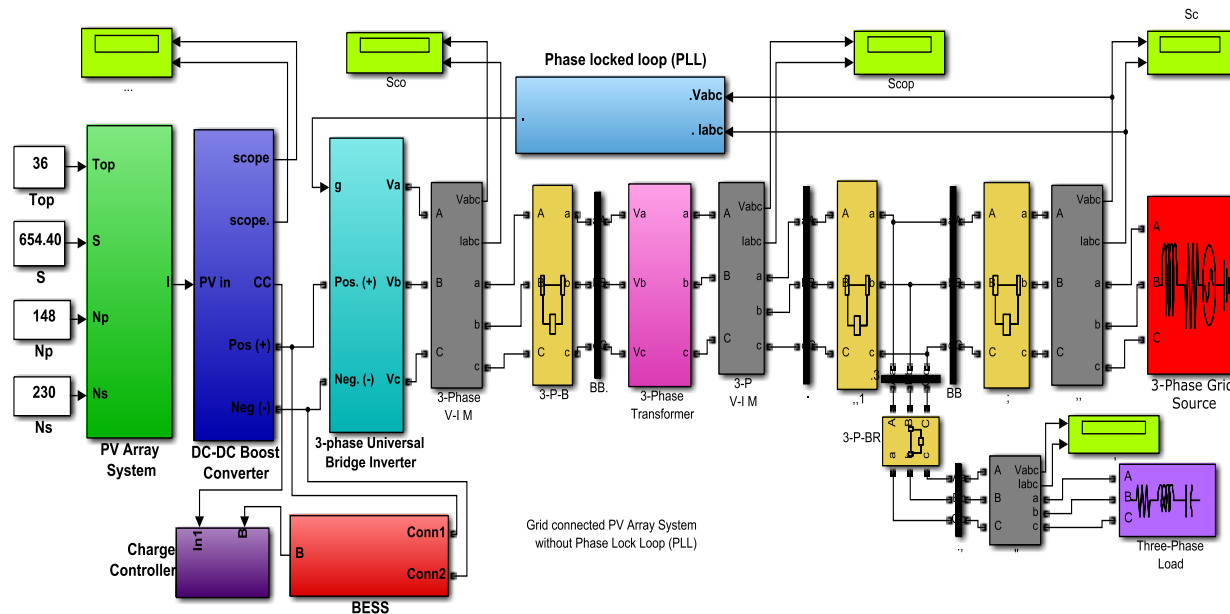


Figure 16; Simulink model of complete photovoltaic grid connected with PLL.

15; Modeled photovoltaic array system result.

The simulated result of PV array model of figure 2 is shown in figure 17. The output of the simulated PV array model consists of DC voltage (V_{dc}), DC current (I_{dc}) and

power (P) waveforms displayed by the scope, as shown in figure 16. Hence, the generated DC voltage of the PV array system is 4000V as displayed by the digital display system. Therefore, based on the output of the photovoltaic array the desired result has been obtained.

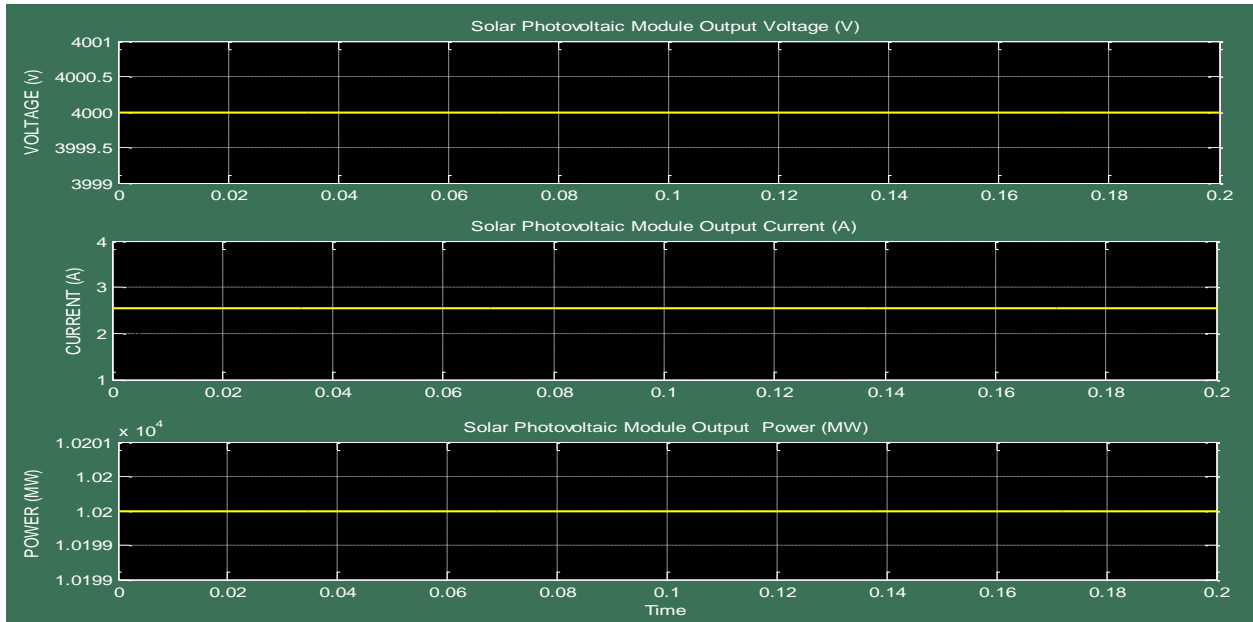


Figure 17; Solar PV array output result consists of DC-voltage, current and power.

16; The result of DC-DC boost converter.

The PV-boost converter model of figure 10 was simulated in Matlab/Simulink environment according to the standards IEC with result shown in figure 18 and 19. The scope and digital display system was connected at the output terminal

of the converter for the output result analysis. The generated 4000V DC source of the PV array model was boosted to 7400V_{dc}.

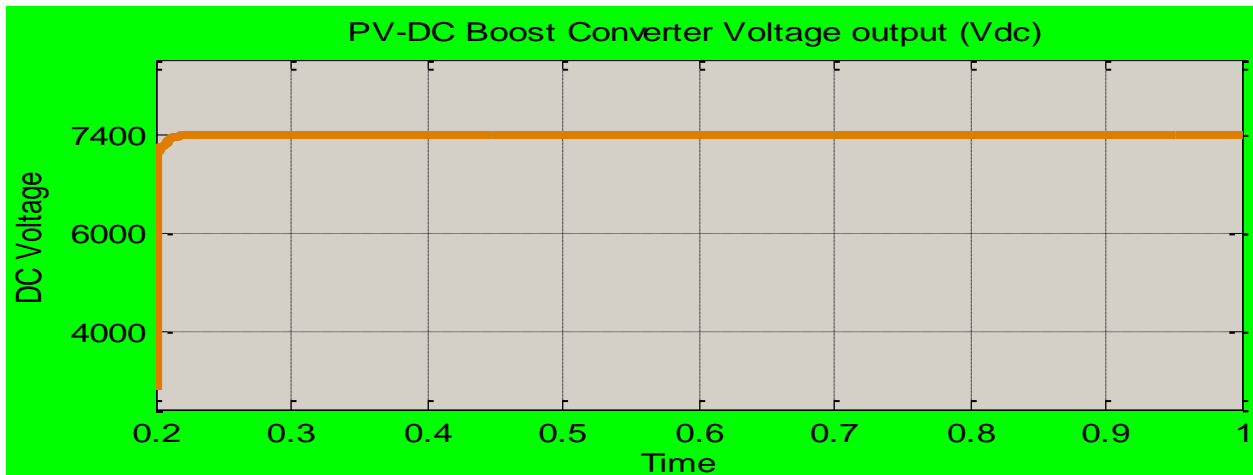


Figure 18: Photovoltaic-DC Boost Converter voltage output (Vdc)

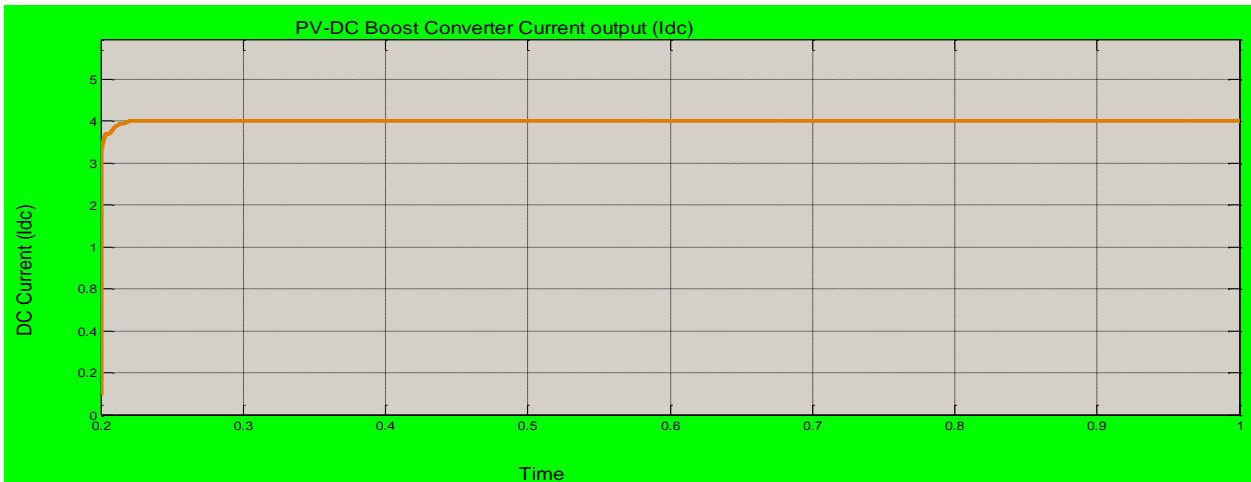


Figure 19: Photovoltaic-DC Boost Converter current output (Idc)

17; Three-phase universal bridge inverter output.

Matlab/Simulink software was used in the simulation of complete system of figure 11, given the output result of generated three-phase AC waveforms of figure 20. The

inverter does not boost or step-up the input voltage but generate the input signals into sinusoidal AC signals. In this case V_{abc} is fed to a step-up transformer for the purpose of boosting the AC signal to a grid voltage level of 33KV.

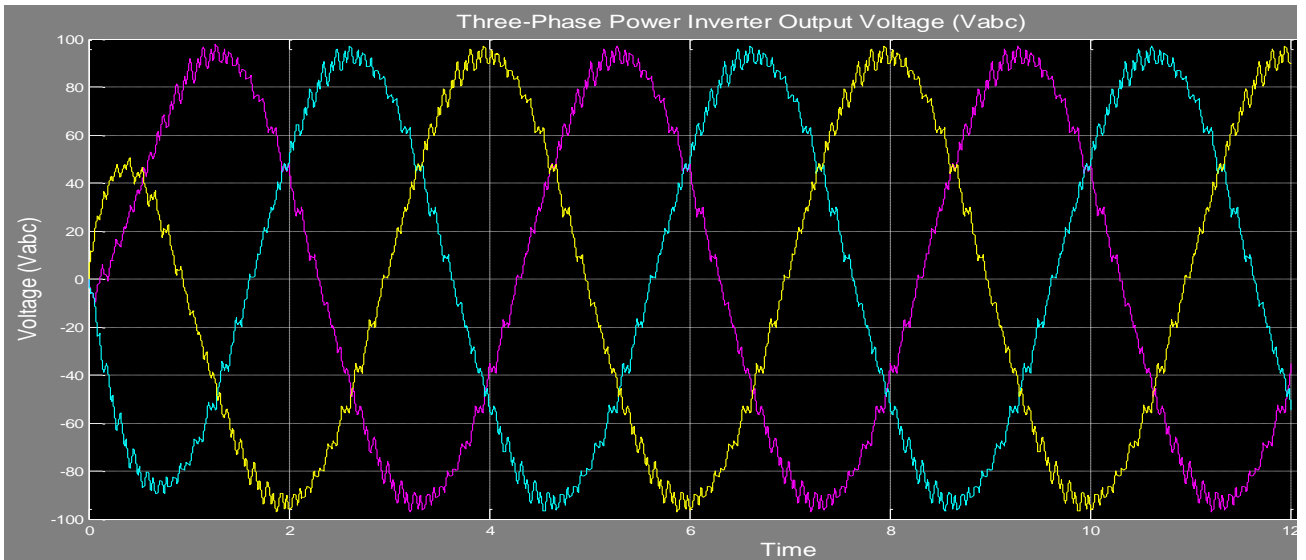


Figure 20; Three-phase universal bridge inverter result.

18; Result of complete solar PV grid system connected without PLL system;

The complete grid connected solar PV model of figure 15 was connected without control (PLL). The simulation of the modeled grid connected solar PV system of figure 15 output result is shown in figure 21. The output result

clearly indicated that the synchronization was unbalanced due to the absent of PLL. Therefore, due to the poor result obtained from the system PLL is needed in the system to clear the distortions on the lines

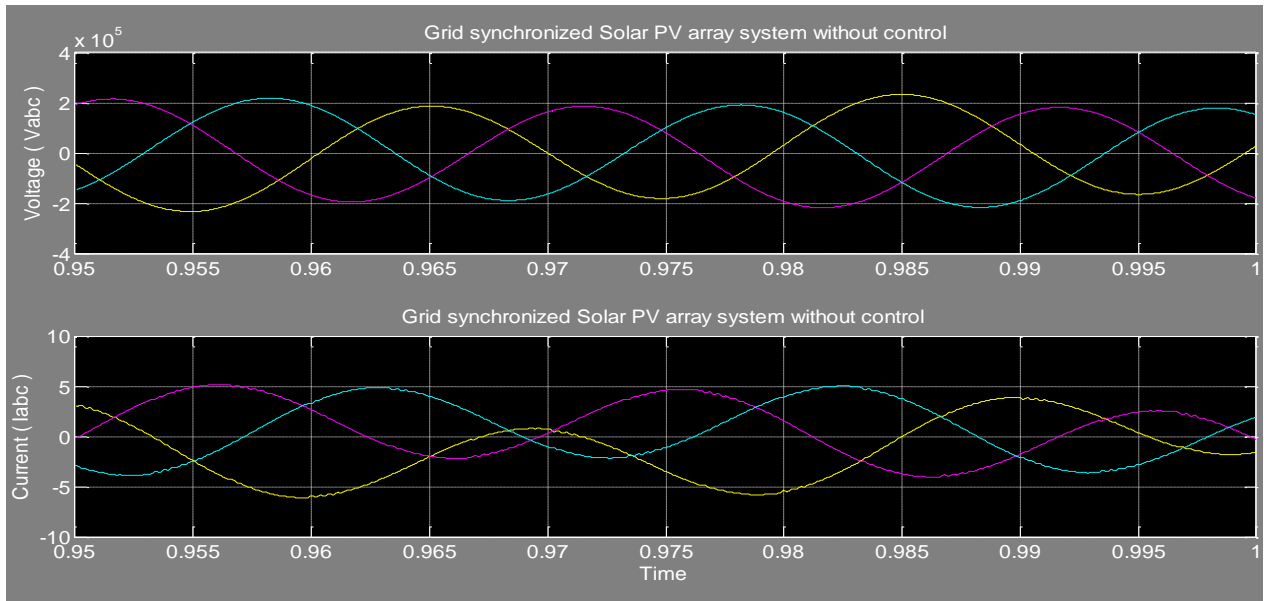


Figure 21; The result of grid synchronized Solar PV array system without a PLL system

19; Result of simulated complete grid connected solar PV system with PLL

The simulated result of the grid-connected solar PV system of figure 16 synchronized with PLL is shown in figure 22. The introduction of the PLL into the system was due to the unbalanced output result observed from figure 20. The selection of Phase lock loop was due to its high degree of

immunity and insensitivity to disturbances, harmonics, unbalance and sags. Hence, based on the analyzed result, the generated 3.40KV by the PV array system injected into the utility grid network, via the three-phase step-up transformer has been satisfactory, and has complied with IEC standards.

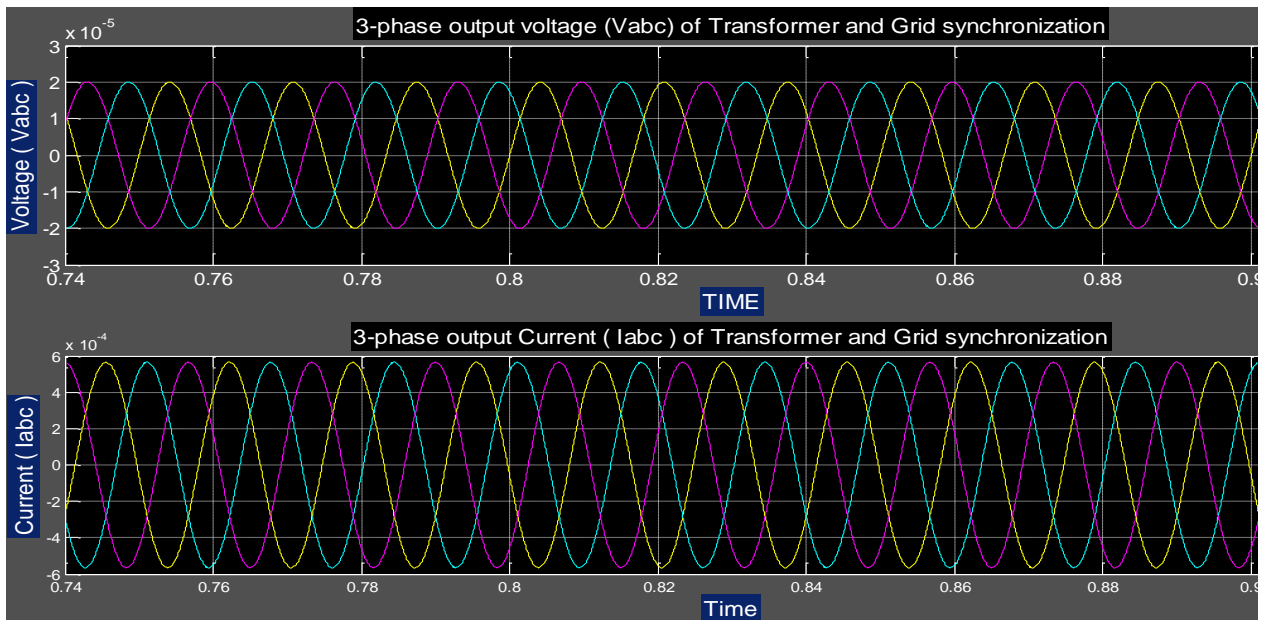


Figure 22; Solar PV array and Grid synchronization output.

20; Discussion of Results

Solar energy sources are important part of energy supply to the utility grid Network. In this study, grid connected photovoltaic-battery energy storage system generation system was modeled and simulated in MATLAB/Simulink environment. The PV array was designed based on the standard mathematical modeling equations, and as well considering the effect of environmental weather conditions (temperature, relative humidity, rainfall, solar radiation and sunshine). The equations are put together in the form of block diagrams, and simulation is carried-out using matlab-simulink program. The photovoltaic array subsystem model was simulated using Simulink program, which generated 4000V DC voltage as the main DC source. The designed photovoltaic (PV) array system was able to supplement power shortfall of 3.40MW of the study area. The DC/DC boost converter was connected to photovoltaic (PV) array where the output DC voltage of the photovoltaic (PV) system was boosted by the designed boost converter to the desired output DC voltage of 7400V. The battery energy storage system (BESS) formed part of the system, which charged or discharge by using the DC/DC bidirectional converter to maintain the power balance between photovoltaic (PV) power generation and the load demand. Simulation results prove that the grid-connected photovoltaic-battery energy storage system (PV/BESS) provides stable and reliable power for loads or power grid during its operation modes. However, the output DC voltage of the converter was inverted to 3-phase AC voltages (Vabc) using inverter, which was synchronized with 150MVA step up transformer used to step it up to the utility grid voltage of 33KV. The transformer's output (i.e. 33KV), is the output of the entire system that is synchronized with the utility grid. The synchronizer (PLL) was connected to the system to clear disturbances on the lines. The results obtained from the simulated system are the same frequency, amplitude, and phase angle, which indicated that the designed grid-connected solar photovoltaic system have succeeded in tackling the problem of power supply in the study area.

21; Conclusion

This thesis presents a complete modeled grid-connected solar system that includes solar photovoltaic array system, DC-DC converter, battery energy storage system, phase locked loop, power inverter, step-up transformer and grid source. The objectives for this thesis have been successfully realized through the modeling, simulation and performance analysis of designed system using Matlab/Simulink tools. The designed system was based on weather condition and load demand obtained from the YEDC that gives the power supply deficit 3.40MW of the study area. The shortfall (3.40MW) of power supply from the grid was augmented by the designed solar photovoltaic-battery energy storage system (PV/BESS). Based on the result the solar photovoltaic array system was able to inject a total power of 3.40MW to the grid.

REFERENCES

- [1] Ahmed, A. A. A.-R. (2013). Digital Control Techniques for Grid-Connected Inverters Electronics and Communications Engineering Department Digital Control Techniques for Grid-Connected Submitted by.
- [2] Aliyu U. O. and Guda, H. A. (2015). Design of a Stand-Alone Photovoltaic System for a Residence in Bauchi, 5(1), 34–44.
- [3] Ani, V. A. (2016). Design of a Reliable Hybrid (PV-Diesel) Power System with Energy Storage in Batteries for Remote Residential Home.
- [4] Bellia, H. (2015). A detailed modeling of photovoltaic module using matlab a detailed modeling of photovoltaic module using matlab. nriag journal of astronomy and geophysics, (june 2014). <http://doi.org/10.1016/j.nrjag.2014.04.001>
- [5] Chen, H., Chen, P., Chang, L., & Bai, W. (2013). Stand-Alone Hybrid Generation System Based on Renewable Energy. <http://doi.org/10.7763/IJESD.2013.V4.405>
- [6] DEBASHIS DAS, S. K. P. (2011). Modeling and simulation of pv array with boost converter : an open loop study modeling and simulation of pv array with boost converter : an open loop study.
- [7] Duka, I. & Noble, C. (2011). High frequency DC-DC boost converter. retrieved from https://www.wpi.edu/pubs/e-project/available_e-project/042711-220800_unrestricted_high_frequency_DC-DC_boost_converter_mqp_final_duka_noble.pdf
- [8] Dunlop, J. P. (n.d.). Batteries and Charge Control in Stand-Alone Photovoltaic Systems Batteries and Charge Control in Stand-Alone Photovoltaic Systems Fundamentals and Application.
- [9] Engineering, A., Ahmad, Z., & Singh, S. N. (2013). Modeling and Control of Grid Connected Photovoltaic System- A Review, 3(3), 40–49.
- [10] GEBREEL, A. A. G. M. (2011). Simulation and implementation of two- level and three-level inverters by matlab and rt-lab.
- [11] Gupta, A., & Garg, P. (2013). Grid integrated solar photovoltaic system using multi level inverter, 3952–3960.
- [12] Guyo, K. G., & A. (2013). Design of a Grid Connected Photovoltaic System for Enhancement of Electrical Power Supply in Kenya : A Case Study of Nairobi Embakasi Kidegho Gideon Guyo A thesis submitted in partial fulfillment for the degree of Master of Science in (Electrical Enginee. Photovoltaic System for Enhancement of Electrical Power Supply.
- [13] Henry Massawe S, P. U. (2015). Modeling and Simulation of a PV System using DC-DC Converter School of Electrical Engineering Aparna K P , Priya R , Sindhu Suryanarayanan, 1(2), 9–16.
- [14] Hosseini, E. (2015). Modeling and simulation of choppers switching via matlab / simulink, 12(1), 10–17.

- [14] Khamis, A., Shareef, H., & Ayob, A. (2011). Modeling and simulation of a microgrid testbed using photovoltaic and battery based power generation microgrid system modeling photovoltaic (pv) model, 2(11), 658–666.
- [15] Kircicek, Y., Aktas, A., & Ucar, M. (2014). Modeling and Analysis of a Battery Energy Storage System Supplied from Photovoltaic Power Source, 1–13.
- [16] Limkumnerd, S., & Eungdamrong, D. (2007). Mathematical models and simulations of phase noise in phase-locked loops, (February 2007).
- [17] Naidu, V. V, & Mohan, T. M. (2013). Modeling and simulation of photovoltaic system, (6), 2–7.
- [18] Natsheh, E. M., Albarbar, A., & Yazdani, J. (2009). Modeling and Control for Smart Grid Integration of Solar / Wind Energy Conversion System. Modeling and Control for Smart Grid Integration of Solar/Wind Energy Conversion System, 1–8.
- [19] Rafal, K., Jasinski, M., & Kazmierkowski, M. P. (2011). Grid synchronization and symmetrical components extraction with PLL algorithm for grid connected power electronic converters – a review, 59(4). <http://doi.org/10.2478/v10175-011-0060-8>
- [20] Rout, S. (2015). Mathematical modelling of grid connected photovoltaic system using matlab / simulink and hardware implementation, (etcc), 6–11.